The zinc electrode : its behaviour in the nickel oxide-zinc accumulator

THE ZINC ELECTRODE

ITS BEHAVIOUR IN THE NICKEL OXIDE-ZINC ACCUMULATOR

JOS HENDRIKX

THE ZINC ELECTRODE

COVER:

SHAPE CHANGE OF THE ZINC ELECTRODE AS RESULT OF CYCLING

THE ZINC ELECTRODE

ITS BEHAVIOUR IN THE NICKEL OXIDE-ZINC ACCUMULATOR

PROEFSCHRIFT

TER VERKRIJGING VAN DE GRAAD VAN DOCTOR IN DE
TECHNISCHE WETENSCHAPPEN AAN DE TECHNISCHE
HOGESCHOOL EINDHOVEN, OP GEZAG VAN DE RECTOR
MAGNIFICUS, PROF. DR. S.T.M. ACKERMANS, VOOR
EEN COMMISSIE AANGEWEZEN DOOR HET COLLEGE
VAN DEKANEN IN HET OPENBAAR TE VERDEDIGEN OP
DINSDAG 29 MEI 1984 TE 16.00 UUR

DOOR

JOZEF LAURENTIUS HUBERTUS MICHIEL HENDRIKX

GEBOREN TE WEERT

Dit proefschrift is goedgekeurd door
de promotoren   Prof. E. Barendrecht
           en   Prof.Dr. J.R. Selman
     co-promotor Dr. W. Visscher

aan mijn ouders

Author's publications, dealing with subjects described in this thesis:

1. M.Y. Abyaneh, J.L.H.M. Hendrikx, W. Visscher and E. Barendrecht
   The Electrocrystallization of Zinc from Alkaline Media
   J. Electrochem. Soc. 129 (1982) 2654.

2. J.L.H.M. Hendrikx, W. Visscher and E. Barendrecht
   Interaction of Zinc deposited from an Alkaline Solution
   with a Polycrystalline Silver Substrate
   Electrochem. Acta 28 (1983) 743.

3. J.L.H.M. Hendrikx, A. van der Putten, W. Visscher and E. Barendrecht
   The Electrodeposition and dissolution of Zinc and Amalgamated Zinc
   in Alkaline Solutions
   Electrochem. Acta 29 (1984) 81.

CONTENTS

1. INTRODUCTION

It was in 1800 that Volta [1] discovered the galvanic cell, which supplies electric current as a result of chemical processes occurring in the cell. Volta's piles were constructed of zinc disks as negative electrodes and silver or copper disks as positive electrodes. Since that time considerable research has gone into the development and amelioration of these cells (batteries) and from the very beginning zinc has proved to be attractive as negative electrode material.

In 1836 the Daniell cell [2] was invented and in 1865, the highly important Leclanché cell [3,4] came on the scene. Various improvements were made to the Leclanché cell, eventually leading to a 'dry' battery and in its improved form this cell is still widely used today. All these primary cells use zinc as electrode material.

The secondary battery system, zinc-nickel oxide, was discussed for the first time by de Michalowski [5] in 1899 and patented in 1901 by Junger [6] and Edison [7]. This cell, however, because of its short cycle life and various other problems (see later), turned out to be unattractive commercially and interest in it was lost.

The lead-acid secondary battery invented by Planté in 1860 is still the most commonly used battery. Although for load leveling in electricity plants and for traction purposes in electric vehicles, it is not the optimum battery because of its low energy density, it remains until now the most reliable one.

For more than one reason much of the developmental effort on new aqueous electrolyte batteries has been focussed on battery systems with zinc as the negative electrode e.g. the zinc-nickel oxide system. In this system the following electrode reactions take place:

$$Zn + 2OH^- \underset{\text{Charge}}{\overset{\text{Discharge}}{\rightleftharpoons}} ZnO + H_2O + 2e^- \text{ , } E^o = 1.25 \text{ V} \qquad (1.1)$$

$$2\ NiOOH + 2H_2O + 2e^- \underset{\text{Charge}}{\overset{\text{Discharge}}{\rightleftharpoons}} 2Ni(OH)_2 + 2OH^- \text{ , } E^o = 0.48 \text{ V} \qquad (1.2)$$
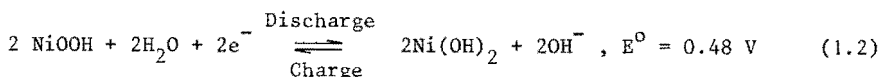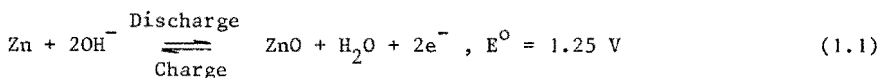
giving the overall cell reaction as

$$Zn + 2\ NiOOH + H_2O \underset{\text{Charge}}{\overset{\text{Discharge}}{\rightleftharpoons}} ZnO + 2Ni(OH)_2 \text{ , } E^o = 1.73 \text{ V} \qquad (1.3)$$
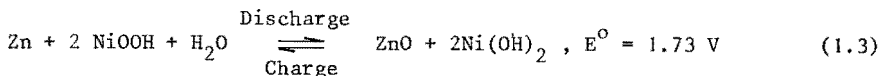
The cell voltage is 1.73 V. The electrolyte is KOH, with concentrations

in the range of 4 – 10 M. Based solely on the electrical capacity and
weights of reactants, the theoretical energy density is 373 Wh/kg. The
practical energy density, however, is much lower due to the fact that
utilization of reactants is not complete and because of the weight of
extra essentials such as current collectors, separators, terminals and
cell case. Nevertheless, the practical energy content per unit weight
and volume is still high 60 – 80 Wh/kg [8-10] compared to 40 – 45 Wh/kg
for the lead-acid battery. In addition, the cell can be discharged at
high rates, 100 – 130 W/kg [9-11], and in a relatively wide temperature
range. The mechanical stability of the battery is also very satisfactory
[9].
Despite these advantages, there are a number of problems which hinder a
breakthrough occurring for this battery. The main problem is the limited
cycle life, i.e. strong reduction of the capacity of the cell on cycling
caused by various processes at the zinc electrode of which the most
important are:

– Shape Change i.e. the reduction of the zinc electrode geometric area
  on cycling. The zinc electrode's active material is removed from the
  plate edges and agglomerates towards the plate center (Fig. 1.1). Once
  initiated, this displacement of active zinc progresses as cycling con-
  tinues and results in a reduction of the capacity and the useful life
  of the cell.

before cycling **after cycling**
⟦⟧ **zinc active material**
▨ **current collector**
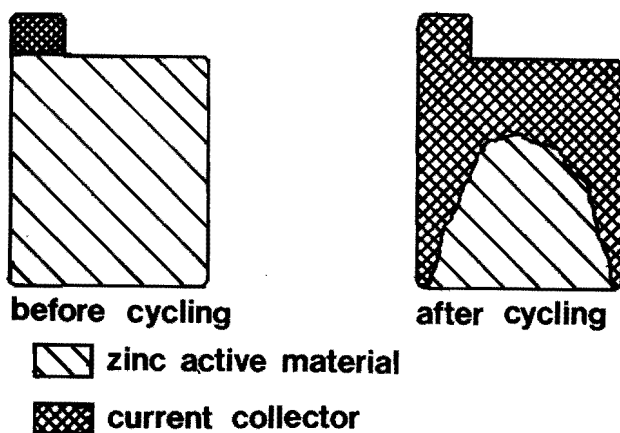
Fig. 1.1 Shape Change of the zinc electrode as result of cycling.

2

- Densification of the active material, which is often observed together
  with shape change. This is a reduction of the surface area of the porous
  electrode, in the direction perpendicular to the surface, and is caused
  by the different current distributions on charge and discharge in the
  porous system.

- Passivation which inhibits the zinc discharge process, due to the formation
  of zinc oxide and hydroxide layers at the surface.

- Dendrite formation which can cause cell failure by internal short-circuiting.
  Much research has been done on separators to prevent short-circuiting,
  and on additives to the electrode and electrolyte to stop or mitigate
  zinc dendritic growth.

A second problem of the cell is its sensitivity to overcharging [9,12]
caused by the disparity in charging efficiencies between the positive
and the negative electrodes. A further disadvantage is the relatively poor
charge retention [9]. After a rest period of one month at room temperature,
only approximately 70% of the capacity is available.
This thesis attempts to investigate certain aspects of zinc electrode
reaction and behaviour in view of its application in batteries.
Chapter 2 begins with a literature review on the properties of zinc
including its solution chemistry and the anodic and cathodic processes.
This is followed by a discussion of the properties of the zinc electrode
in a battery system with particular attention to porous structure. Shape
change is emphasized as the most important factor leading to limited
battery cycle life. Two existing models of the phenomenon of shape change,
based on electro-osmosis and current distribution are treated in detail.
It is shown that neither of these models is adequate to describe
consistently the phenomena observed.
In chapter 3, the first stages of electrocrystallization (nucleation and
growth) are investigated. This is done because in the battery, deposition
and dissolution processes take place, during charging and discharging of
the zinc electrode. In these processes, next to charge transfer and trans-
port of reactants and products, also the formation and breakdown of crystal
lattices are involved. Because the charge transfer kinetics of zinc are
very fast, this electrocrystallization process is decisive. Polycrystalline
silver is used as substrate, because in batteries a silver current collector
is often used and reproducible results can be obtained with this substrate.

In chapter 4 the surface reactions between the silver substrate and the
deposited zinc layer will be more thoroughly investigated.

The reaction mechanism of zinc and amalgamated zinc in an alkaline electro-
lyte is dealt with in chapter 5. In an actual battery, the zinc electrode
is usually amalgamated to hinder the formation of hydrogen. However, there
is little information available to date in the literature on the reaction
mechanism of the amalgamated zinc. Therefore, the investigation incorpo-
rates zinc electrodes amalgamated in different ways. The pure zinc electrode
is also included because the literature contains proposals on several
different mechanisms ; these, however, are based on contradictory experi-
mental results.

In chapter 6 the actual battery system is studied in order to obtain more
information on cycling behaviour and especially on shape change phenomenon.
The effect on cycle behaviour of different amalgamation techniques of the
zinc electrode and several additives to the electrode is described.

Chapter 7 deals with impedance measurements of the zinc electrodes, as used
in the study of the reaction mechanism, which gives additional information
about the reaction mechanism of the zinc electrodes. Also the impedance
technique was applied to study the complete battery behaviour in order to
find a correlation with the changes of the zinc electrode during cycling,
in particular, the shape change phenomenon.

Literature

1. A. Volta, Phil. Trans., Rog. Soc. (Lond.) $\underline{90}$ (1800) 403.
2. J.F. Daniell, Phil. Mag. III $\underline{8}$ (1836) 421.
   Phil. Trans. $\underline{126}$ (1836) 106, 125.
   Phil. Trans. $\underline{127}$ (1837) 141.
3. G. Leclanché, French Patent No. 71.865 (1866).
4. G. Leclanché, Les Mondes $\underline{16}$ (1868) 532.
5. T. de Michalowski , British Patent No. 15.370 (1899).
6. W. Jugner, Swedish Patent No. 15.567 (1901).
7. T.A. Edison, British Patent No. 20.072 (1901).
8. J. McBreen and E.J. Cairns, Advances in Electrochemistry and Electro-chemical Engineering vol. 11, p. 273. H. Gerischer and C.W. Tobias, ed., John Wiley & Sons, New York, 1978.
9. U. Falk, I.E.E. Energy Ser. $\underline{1}$ (Electrochemical Power Sources) (1980), p. 324-402.
10. N.P. Yao, C.C. Christianson, F. Hornstra, 16th Intersoc. Energy Conversion (1981) 641.
11. F.P. Kober and A. Charky in Power Sources Vol. 3, p. 309, D.H. Collins ed.,Oriel Press, Newcastle upon Tyne, 1971.
12. J. McBreen, Comprehensive Treatise of Electrochemistry vol. 3, p. 314, J.O'M. Bockris et al. ed., Plenum Press, New York 1981.

5

2. LITERATURE REVIEW

2.1. Properties of zinc in alkaline solution.

2.1.1. Solution Chemistry.

The electrolyte in the Zn/NiOOH system consists of potassiumhydroxide with concentrations in the range of 4 to 12 M and zinc oxide. The zincate ion, $Zn(OH)_4^{2-}$, with tetrahedral structure [1-3] is the only important zinc ion in KOH electrolytes [4]. The solubility of ZnO in KOH is shown in Fig. 2.1 [5]; it appears to be independent of temperature [6,7]. The figure shows that "supersaturated" solutions can be formed by electrodissolution of zinc into alkaline solutions [5]. The decomposition process of the supersaturated solution is very slow and can take about one year to reach equilibrium.
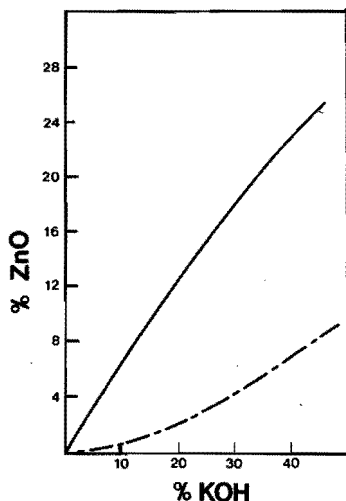
Fig. 2.1   Zincate solubility in KOH-solu-
tions at room temperature. [5]
solid line: solubility limit of electro-
litically generated zincate.
broken line: solubility of ZnO.

It is not yet clear what the solute species are in these supersaturated solutions [8]. McBreen, Dirkse and Nanis [9-11] have determined the diffusivity in KOH at various concentrations and temperatures [9-11]. The diffusivity remains constant with KOH concentrations up to $\sim$ 7 M while above this concentration it decreases rapidly with increasing KOH concentration.

2.1.2. Anodic processes at the zinc electrode in alkaline solutions.

The utilization of a zinc electrode in alkaline solutions depends on the ability of the electrode to remain active in the anodic dissolution process

$$Zn + 4\ OH^- \rightarrow Zn(OH)_4^{2-} + 2e^- \tag{2.1}$$

However, this zinc discharge is often inhibited by the formation of a passivating zinc oxide or hydroxide layer. Anodic dissolution and passivation behaviour has been the subject of many investigations using galvanostatic techniques [12-22], potential sweep techniques [23-33], rotating ring-disc techniques [24,27,28] and the X-ray diffraction technique [34]. Using the galvanostatic technique, the relation between the current density and the passivation time, at which a large increase in the overpotential occurs, has been studied. On zinc sheets the results in general conform to the relationship [12-21]

$$(i - A) \, t_p^{\frac{1}{2}} = B \qquad\qquad\qquad (2.2)$$

in which

   i = the applied current density

   t_p = the passivation time

   A,B = correlation constants, of which the values are dependent on experimental conditions, such as KOH concentration and the convection pattern of the electrolyte.

A summary of experimental data for A and B has been given [19]. The correlation constant A can be taken as a limiting current density, below which no passivation takes place. Values of B give an indication of the degree of utilization to be expected at various KOH concentrations: at $\sim$ 7 M this value reaches a maximum [15]. Different mechanisms have been proposed to explain the zinc passivation behaviour, namely dissolution-precipitation [18,23,35], adsorption [24,28,36,37] and two-dimensional growth of crystals [25,38]. In all three mechanisms, the zinc oxide film is responsible for passivation.

Two kinds of oxides are formed [23,26]:

- Type-I film. This film consists of a porous white layer (loose and flocculent) which is formed under stagnant conditions. It is thought that this layer is formed by the dissolution-precipitation mechanism [27,35,39, 40,41]. At low current densities (< 150 mA/cm^2) passivation of the electrode occurs when the film becomes so thick that the rate of supply of OH$^-$-ions through the film is less than the rate of demand of OH$^-$-ions for the electrode reaction [19,41].

- Type-II film. This film is more compact, and is thought to be formed by surface growth processes [23,26]. It is considered to be responsible for the passivation of zinc in alkaline solutions [23] at higher current densities (> 150 mA/cm^2) [20].

In the passivation process both types of films play an important role [27]:
the porous type-I film is not responsible for passivation, but retards
the mass transfer. This ultimately results in a decrease of the pH in the
porous film resulting in the formation of a thin compact type-II layer,
which is responsible for the passivation.
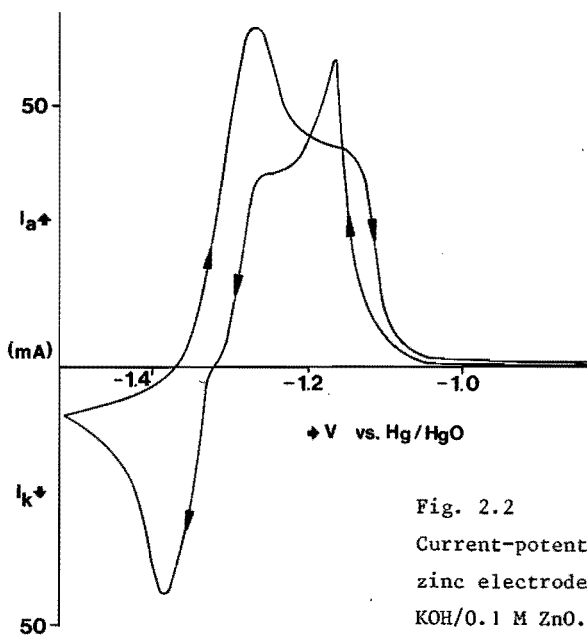
Fig. 2.2
Current-potential curve of a stationary
zinc electrode (0.28 cm^2) in 3 M
KOH/0.1 M ZnO. Scan rate: 50 mV s^{-1} [42]

Current-potential curves for zinc are complex due to the occurrence of
several processes [23-33]. An example is given in Fig. 2.2 [42]. Experi-
mental conditions such as the scan rate, electrolyte concentration and
convection regime influence the shape of these curves. The major feature
of these curves is that they show two anodic current peaks that become more
distinct at lower scan rate [26]. These double peaks are attributed to the
formation of hydrogen, which is catalyzed by the anodic films on zinc
[26,32]. Prior to passivation current oscillations have been observed
[27,28,29,43]. These oscillations are ascribed to buckling and tearing
of the compact type-II film [23,43] or to a process in which passivating
films appear and disappear as a result of changes in pH at the surface
[27].

2.1.3. Cathodic processes at the zinc electrode in alkaline solution.
The deposition of zinc from alkaline solutions has also been intensively
studied using potentiostatic and/or galvanostatic techniques (occasionally

in combination with microscopic observation) [44-49], SEM [48,50,51,52],
X-ray diffraction technique [50] or impedance technique [53-55].
Three types of zinc deposits have been observed:

I. Smooth compact deposit.

On a smooth zinc electrode the initial deposit is epitaxial, regardless
of the overpotential [45,47], and consists of two-dimensional growth
layers. In vigorously stirred solutions this growth form is retained
for a long time at low overpotential [49]. In unstirred solutions there
is an optimum value of current density (210 A/m^2) which gives a maximum
thickness of the compact zinc layer [49]. However, after some time,
depending on the experimental conditions, this type of growth stops
and faced protuberances (also called protrusions) begin to form on the
substrate [45]. The mechanism for the formation of these protuberances
is not understood. It is suggested that these protuberances, or pyramids,
arise as a result of the rotation of a screw dislocation [48]. Moreover,
the formation of these protuberances causes the onset of other growth
forms.

II. Spongy, mossy deposit.

This deposit is finely grained, poorly adherent [45] and consists of
fine, helically coiled zinc whiskers, 0.6 to 1.0 μm in diameter [46].
It is formed at low overpotentials (< 75 mV) [49] and the formation
is apparently not controlled by mass transfer but by some specific
steps in the charge transfer reaction [53]. It has been postulated
that a coupling between the interfacial reactions and the surface
diffusion of Zn^+_{ads} can explain the formation of the mossy deposit
[54,55].

III. Dendritic deposit.

The transition to dendrite formation corresponds to the onset of
mass transport control and is characterized by a critical current
density, which is dependent on hydrodynamic conditions [56] and tempe-
rature [49]. The deposit has a fern-like structure. Initiation and
propagation of the deposit have not been completely understood so far.
Bockris et al. [47,48] have proposed that dendrites originate from
the tips of pyramids formed as the result of the rotation of a screw
dislocation. They begin to grow when the mode of mass transfer changes
from linear to spherical diffusion. Only a small fraction of these
pyramids develop into dendrites [48,52]. Mansfeld and Gilman [51] also
observed pyramids but found that dendrites were more frequently
initiated at the bases of the pyramids. Powers [45] suggests that

entities formed by dissolution of dark-coloured anodic layers expedite the nucleation of dendrites. According to the lit. [54] a strong acceleration of the nucleation rate, caused by the autocatalytic formation of the adions, plays an important role in the formation of dendrites.

May and Kautz [57] presented a mechanism to explain the different morphologies.

- Dendrites are likely to be due to a more rapid growth on the non-basal crystallographic planes than on the basal planes.
- Mossy deposit is a result of dissolution from the non-basal planes at low cathodic potentials.

Model systems were sought which would produce such a phenomenon. Two such systems were found to be in accord with the proposed mechanism. One involves rapid disproportionation of Zn^+-species on the non-basal planes; the other involves a redox reaction between zinc-zincate and hydrogen water systems.

In batteries, dendrite deposition is undesirable because it leads to short-circuiting. Along with the search for better separators which hinder short-circuiting, attempts have also been made to control the deposit morphology (and to get mossy deposits, which are desirable in battery electrodes).

Factors which influence the morphology are:

. Additives to the electrolyte

Certain additives modify the deposit morphology inhibiting the formation of dendrites and widening the range of current densities leading to compact deposits [58-60]. Diggle et al. [59] ascribed the inhibition of zinc dendrite morphology to a blocking action in the case of some organic additives, and, in the case of lead and quaternary ammonium salts, to specific adsorption, which is supposed to lower the electro-static field.

Bressan and Wiart [60,61] concluded that the additive lead acetate modifies the rates of some elementary reactions taking place at the interface and seems to decrease that of the autocatalytic step in the reaction mechanism. They also concluded that the additives give rise to an accelerated nucleation rate ensuring a faster renewal of active growth sites.

. Various charging methods [49,62-66]

Periodically varying cathodic currents modify the deposit morphology
by suppressing the formation of zinc sponge and extending the formation
of compact epitaxial deposit [49,65]. However, control of the deposit
morphology is limited and hence this does not appear to be a very
promising method for solving the problems of the zinc electrode. (Appelt
[66] has given a qualitative explanation based on the formation of a
diffusion layer and the change of the zincate concentration at the
surface when a "three-component-impuls current" is used. This current
also influences the initiation of zinc dendrites).

. Electrolyte flow

Naybour [56] has demonstrated the effect of electrolyte flow on the
morphology, and correlated the deposit morphology with the Reynolds
number: on increasing Reynolds numbers the morphology of the deposit
undergoes transition from dendrite to bulbous (a kind of sponge) and
ultimately to a flat deposit (plate-like structures).

Two mechanisms for zinc deposition in and onto ZnO-electrodes have been
proposed [67-70]. One mechanism assumes the direct solid state reduction
from ZnO to Zn [67] and the other assumes that the dissolution of zinc
oxide is followed by reduction of the zincate ion [68]. Drazic and Nagy [68]
concluded that the contribution of the solid-state reaction to the battery
electrode process is not likely to be more than a few percent, if any.
Zavgorodnyaya [69,70] concluded that in less concentrated KOH-solutions
(0.1 to 0.5 N), the reaction occurs predominantly directly in the solid
state and only in part via a prior dissolution step, while in concen-
trated solutions it occurs chiefly via the dissolution step.

2.2. Properties of zinc in batteries.

Porous electrodes are used in battery systems because they attain the high
current densities required. The behaviour of these electrodes in battery
systems involves a greater number of interrelated phenomena than is the
case in planar electrodes. Besides anodic and cathodic phenomena, the
geometry, the structure parameters of the electrode and the cycle con-
ditions also determine the behaviour.

Many investigations have been carried out on porous electrodes, both
experimentally and theoretically. The structure of porous electrodes has
a major influence on the utilization. Several empirical correlations have
been derived for this interdependence [71-73]. From a mathematical model

based on a concentrated ternary electrolyte theory, Sunu and Bennion [74] predicted that, if a membrane separator is applied, the utilization is severely limited by depletion of hydroxyl ions within the zinc electrode compartment. They also predicted that the reaction profiles in the pores are highly non-uniform, and that the reaction zone near the electrode surface is very thin, resulting in a low discharge capacity. This has been experimentally confirmed [75]. On repeated cycling the difference in anodic and cathodic reaction current product distribution causes the redistribution of solid zinc and zinc oxide species in the pore. Information about the reaction product profiles in the porous electrode is obtained by measuring the penetration depth of the reaction in the pore. This can be done with different techniques:

- microslicing of the electrode followed by chemical analysis of zinc and zinc oxide [75,76]
- microscopic measurement of the zinc oxide in the pore [77]
- continuous measurement of current through each segment of a sectioned porous electrode fabricated by photolithographic technique [78,79]

   This gives direct information of the current distribution in the pore. From these measurements it has been concluded that the penetration depth is very small (only a fraction of the thickness of the porous electrode), and that the current distribution is highly non-uniform and varies depending on anodic or cathodic current [78,79].

Investigations of the anodic reaction in a pore have indicated the disso-lution-precipitation mode of ZnO formation [76,77,80]. This zinc oxide is referred to as a type-I film [23]. SEM-observations of these precipitates [78,80] have given insight into morphological aspects of electrocrystallized ZnO (the porosity of the ZnO-film is 80-85%).

Nagy and Bockris [76] have explained current distribution in the porous electrode by a model for an oxide film, consisting of a thin high-resistance compact film beneath the porous oxide upper layer. To account for the passivation mechanism caused by the formation of a compact ZnO within the electrode pores, Liu et al. [79,81] made use of the model of Sunu [74]. They concluded that the high non-uniformity of current distribution was due to the high electrolyte resistance compared to both the charge transfer resistance and the diffusion resistance of OH^--ions.

It has been suggested that the passivation of the electrode may have been caused by pore plugging due to the catalytic hydrogen evolution. The last model considered here, is the migration model, developed by Yamazaki [82]. He formulated the current or reaction product distribution

in a porous electrode but did not take into consideration the precipitation of zinc oxide and passivation. The calculated results showed different reaction product distributions during charge and discharge, attributed to a resistivity change in the pore electrolyte and to a change in the interfacial reaction resistance.

2.2.1. Shape Change.

Shape Change involves the redistribution of the active material on the zinc electrode geometric area with cycling. The active material is removed from the electrode edges and agglomerates towards the plate center. Many investigations have been carried out to gain a better under- standing of this phenomenon.

Parameters influencing Shape Change (SC) are:

- The depth of discharge (DOD)

  Seiger studied the effect of DOD on the cycle life. His study also included failure mechanisms other than SC [83]. The relation between DOD and cycle life was very clear and was expressed in the following exponential function

$$ L = L_o \exp\left[\alpha(1 - D)\right] \qquad (2.3) $$

  in which L is the number of cycles obtained at depth of discharge (D), L_o is the cycle life at 100% DOD (D = 1) and α is a proportionality factor.

- The type of separator.
- The stoichiometric ratio of the negative and positive active material.
- The construction of the cell with the electrodes. The effect of the orientation of the zinc electrode, horizontally or vertically with respect to the earth's gravitational field, on the extent of Shape Change is insignificant [84,85].
- The additives to the zinc electrode.

  Amalgamation of the zinc electrode to increase the hydrogen overpotential also increases the rate of SC [84]. Other additives, however, (such as cadmium, lead and thallium, which also increase the hydrogen overpotential) reduce the rate of SC [86,87]. Some surface active agents, such as Emulphogene, have a positive effect upon the cycle life [88].

  The effect of additives in pasted zinc battery electrodes has been studied in great detail by McBreen at al. [89-91]. They concluded [89] that the benificial effect of some metal oxide additives (PbO, $In(OH)_3$,

13

Tl_2O_3 and mixtures of these) is due to the overpotential increase which improves the current distribution and so decreases the rate of Shape Change. They suggested that this additive effect is in reality a substrate effect and assumed that the adverse effect of HgO is due to a slight overpotential decrease. The effect on the current distribution during formation of the electrodes has been further investigated by means of a sectioned nickel oxide electrode, by the same authors [90]. In the case of zinc electrodes with no additive, the average current density at the edge sections was about twice that at the center sections. Additives such as Tl_2O_3 and $In(OH)_3$ result in a more even current distribution during formation. However, in this latter investigation they found that HgO had little effect on the current distribution which, of course, does not support their earlier findings. In addition, anomalous effects were found with PbO additives because of leaking of the additive into the electrolyte, especially at the electrode edge.

Two different mechanisms have been proposed to explain Shape Change:
- McBreen [92] gives a qualitative explanation of the phenomenon of SC, based on extensive experimental data of the patterns of current and potential distribution during cycling of a zinc electrode. Differences in current distribution during charging and discharging result in accumulation of zinc and exhaustion of reducible zinc species at the plate periphery. He postulated that this leads to the formation of concentration cells, composed of the edges and the center of the electrode, so that zinc dissolves away from the plate edge and is deposited at the plate center. These concentration cells in turn cause Shape Change. The second factor contributing to SC, according to McBreen, is the occurrence of a concentration gradient of zincate, in the beginning of discharge (in the first stages of cycling) due to the current distribution, and leading to a displacement of the zincate in the direction of the center. McBreen's explanation, however, is not satisfactory. A diffusion process is incorporated in the model only at the moment that the concentration gradient in the direction of the center is negative (to explain the movement of zincate to the center) but not when the reducible zinc species at the plate periphery is exhausted and the concentration gradient is positive. Furthermore, the reasoning of McBreen is not consistent regarding the idea of a concentration cell concept. He argues that relaxation of the different potentials over the electrode surface to a common value must occur via

14

a concentration cell, rather than via the much slower diffusion process.
However, different potentials over the zinc electrode arise also in the
beginning of discharge due to variations in zincate concentration.
In this situation he limits himself to a diffusion process concept
only and discounts the concentration cell concept in his explanation.
As a result, the concentration cell concept and the diffusion process
concept are incorporated in the model only when they can explain Shape
Change.

- In their consideration of Shape Change Choi et al. [93] presented a
  mathematical model, based on convective flows induced by electro-
  osmotic and osmotic forces across the membrane separator, which is
  present in the actual battery system. During discharge these forces
  induce a flow of electrolyte from the zinc electrode compartment
  towards the counter electrode compartment, i.e. across the membrane;
  during charge this flow occurs in the reverse direction (see Fig. 2.3).

Fig. 2.3 Schematic view of the convective flows in the accumulator
          ➤ : during charging   1 : zinc compartment
          ➤ : during discharging   2 : membrane separator
                                      3 : nickel compartment

During discharging the solution in the zinc electrode compartment is
supersaturated with zincate and during charging the electrolyte solution
becomes unsaturated due to deposition. The combination of these two
facts results in a net movement of zinc in the y-direction during a
complete cycle. On repeated cycling this leads to Shape Change.
The material redistribution over the zinc electrode and the average
fluid flow rates, which are measured in a zinc/silveroxide cell, with

vented electrodes and a radiation-grafted polyethylene separator [94,95], are in agreement with the predicted values of the model. However, a great discrepancy exists between the predicted and observed cumulative concentration changes at the end of the cycles. But this is attributed to physical differences between the "model"- and the "actual" cell. Experiments were also carried out in cells where provisions were made to prevent convection [94,96]. Although the measured Shape Change was considerably less than in normal cells, this test cannot be regarded as decisive because the depth of discharge (DOD) was only half that of normal cells. The mathematical model predicts that in a cell with minimal convection, the overpotential and current have to be uniform over the whole electrode, but this is not verified by the measurements [96]. Moreover, the model is neither complete nor satisfactory because it only predicts the material redistribution in the y-direction (see Fig. 2.3) and not in the z-direction (in which direction SC also takes place) [92,95], or in the x-direction (see chapter 2.2).

2.3. Literature

1. J.S. Fordyce and R.L. Baum, J. Chem. Phys. $\underline{43}$ (1965) 843.

2. G.H. Newman and G.E. Blomgren, J. Chem. Phys. $\underline{43}$ (1965) 2744.

3. W. van Doorne and T.P. Dirkse, J. Electrochem. Soc. $\underline{122}$ (1975) 1.

4. R.J. Brodd and V.E. Leger, in Encyclopedia of Electrochemistry of the Elements, Vol. 5. A.J. Bard, ed., Dekker, New York, 1976.

5. T.P. Dirkse, Technical Report no. AFAPL-TR-69.90, Contract no. AF 33[615]-3292, Calvin College, Grand Rapids, Mich., Dec. 1969.

6. W.H. Dyson, L.A. Schreier, W.P. Scholette and A.J. Salkind, J. Electrochem. Soc. $\underline{115}$ (1968) 566.

7. C.T. Baker, I. Trachtenberg, J. Electrochem. Soc. $\underline{114}$ (1967) 1045.

8. T.P. Dirkse, J. Electrochem. Soc. $\underline{128}$ (1981) 1412.

9. J. McBreen, Report No. N68-15716, Contract No. NAS 5-10231, Yardney Electric Corp., New York, June 1967.

10. T.P. Dirkse, Technical Report No. AFAPL-TR-72.87, Contract No. S33615-70-C-1022, Project 3145, Calvin College, Grand Rapids, Mich., Dec. 1972.

11. L. Nanis, JPL Contract No. 952.543, Report No. N70-23265, University of Pennsylvania, February 1970.

12. R. Landsberg, Z. Phys. Chem. $\underline{206}$, (1957) 291.

13. R. Landsberg and H. Bartel, Z. Electrochem. $\underline{61}$, (1957) 162.

14. M. Eisenberg, H.F. Bauman and D.M. Brettner, J. Electrochem. Soc. 108, (1961) 909.

15. N.A. Hampson and M.J. Tarbox, J. Electrochem. Soc. 110, (1963) 95.

16. N.A. Hampson, M.J. Tarbox, J.T. Lilley and J.P.G. Farr, Electrochem. Technol. 2, (1964) 309.

17. J.P. Elder, J. Electrochem. Soc. 116, (1969) 757.

18. T.P. Dirkse and N.A. Hampson, Electrochem. Acta 16, (1971) 2049.

19. M-B. Liu, G.M. Cook and N.P. Yao, Report ANL/OEPM-80-1, Argonne National Laboratory, Illinois, 1980.

20. M-B. Liu, G.M. Cook and N.P. Yao, J. Electrochem. Soc. 128 (1981) 1663.

21. R.N. Elsdale, N.A. Hampson, P.C. Jones and A.N. Strachan, J. Appl. Electrochem. 1 (1971) 213.

22. G. Coates, N.A. Hampson, A. Marshall and D.F. Porter, J. Appl. Electrochem. 4, (1974) 75.

23. R.W. Powers and M.W. Breiter, J. Electrochem. Soc. 116 (1969) 719.

24. M.N. Hull and J.E. Toni, Trans. Faraday Soc. 67 (1971) 1128.

25. R.D. Armstrong and G.M. Bulman, J. Electroanal. Chem. 25 (1970) 121.

26. R.W. Powers, J. Electrochem. Soc. 118 (1971) 685.

27. M.C.H. McKubre and D.D. MacDonald, J. Electrochem. Soc. 128 (1981) 524.

28. M.N. Hull, J.E. Ellison and J.E. Toni, J. Electrochem. Soc. 117 (1970) 192.

29. T.P. Dirkse, N.A. Hampson, Electrochim. Acta 17 (1972) 387.

30. R.D. Armstrong and M.F. Bell, Electroanal. Chem. and Interfacial Electrochem. 55 (1974) 201.

31. G.S. Vozdvizhanskii and E.D. Kochman, Zh. Fiz. Khim. 39 (1965) 657.

32. I. Sanghi and M. Fleischmann, Electrochim. Acta 1 (1959) 161.

33. T.I. Popova, N.A. Simonova and B.N. Kabanov, Elektrokhimiya 3 (1967) 1419.

34. R.W. Powers, J. Electrochem. Soc. 116 (1969) 1652.

35. S. Szpak and C.J. Gabriel, J. Electrochem. Soc. 126 (1979) 1914.

36. B.N. Kabanov, Electrochim. Acta 6 (1962) 253.

37. E.A. Ivanov, T.I. Popova and B.N. Kabanov, Sov. Electrochem. 5 (1969) 643.

38. H. Kaesche, Electrochim. Acta 9 (1964) 383.

39. Z. Nagy and J.O'M. Bockris, J. Electrochem. Soc. 119 (1972) 1129.

40. T. Katan, J.R. Savory and J. Perkins, J. Electrochem. Soc. 126 (1979) 1835.

41. A. Marshall, N.A. Hampson, J. Appl. Electrochem. 7 (1977) 271.

42. Unpublished Results, A.M.T.P. van der Putten.

43. M. Breiter, Electrochim. Acta 15 (1970) 1297.

44. R.W. Powers, Electrochem. Technol. 5 (1967) 429.

45. R.W. Powers, ILZRO Project No. ZE-T20, Progress Report No. 5, 1967.

46. Z.O.J. Stachurski, NASA contract No. NAS 5-S873, N67-26278, 1965.

47. J.W. Diggle, A.R. Despić and J.O'M. Bockris, J. Electrochem. Soc. 116 (1969) 1503.

48. J.O'M. Bockris, Z. Nagy and D. Drazic, J. Electrochem. Soc. 120 (1973) 30.

49. S. Arouete, K.F. Blurton and H.G. Oswin, J. Electrochem. Soc. 116 (1969) 166.

50. I.N. Justinijanovic and A.R. Despic, Electrochim. Acta 18 (1973) 709.

51. F. Mansfeld and S. Gilman, J. Electrochem. Soc. 117 (1970) 1521.

52. R.D. Naybour, Electrochim. Acta 13 (1968) 763.

53. I. Epelboin, M. Ksouri and R.J. Wiart, J. Electrochem. Soc. 122 (1975) 1206.

54. I. Epelboin, M. Ksouri and R.J. Wiart, Farad. Symp. Chem. Soc. 12 (1977) 115.

55. I. Epelboin, M. Ksouri and R. J. Wiart, J. Electroanal. Chem. 65 (1975) 373.

56. R.D. Naybour, J. Electrochem. Soc. 116 (1969) 520.

57. C.E. May and H.E. Kautz, NASA-TM-82768, Cleveland, Ohio, 1981.

58. F. Mansfeld, S. Gilman, J. Electrochem. Soc. 117 (1970) 588.

59. J.W. Diggle and A. Damjanovic, J. Electrochem. Soc. 119 (1972) 1649.

60. J. Bressan, R. Wiart, J. Appl. Electrochem. 7 (1977) 505.

61. J. Bressan, R. Wiart, J. Appl. Electrochem. 9 (1979) 43.

62. J.E. Oxley, NASA Report No. ER-377, Leesona Moos Laboratories, Great Neck, N.Y., 1966.

63. V.V. Romanov, Zh. Priklad. Khim. 34 (1961) 2692.

64. J.N. Jovicavic, D.M. Drazic and A.R. Despic, Electrochim. Acta 22 (1977) 589.

65. D.T. Chin, R. Sethi and J. McBreen, J. Electrochem. Soc. 129 (1982) 2677.

66. K. Appelt and K. Jurewicz, Electrochim. Acta 27 (1982) 1701.

67. O. Hladic and K. Schaabe, Electrochim. Acta 15 (1970) 635.

68. D. Drazic and Z. Nagy, J. Electrochem. Soc. 118 (1971) 255.

69. V.I. Lubyanova and E.F. Zavgorodnyaya, Soviet Electrochem. 15 (1979) 918.

70. E.F. Zavgorodnyaya, V.I. Lubyanova and Yu. R. Rodak, Sov. Electrochem. 16 (1980) 870.

71. C.M. Shepherd and H.C. Langelan, J. Electrochem. Soc. 109 (1962) 657.

72. C.M. Shepherd and H.C. Langelan, J. Electrochem. Soc. 114 (1967) 8.

73. G. Coates, N.A. Hampson, A. Marshall and D.F. Porter, J. Appl. Electro-chem. 4 (1974) 75.

74. W.G. Sunu and D.N. Bennion, J. Electrochem. Soc. 127 (1980) 2007.

75. W.G. Sunu and D.N. Bennion, J. Electrochem. Soc. 127 (1980) 2017.

76. Z. Nagy and J.O'M. Bockris, J. Electrochem. Soc. 119 (1972) 1129.

77. T. Katan, J.R. Savory and J. Perkins, J. Electrochem. Soc. 126 (1979) 1835.

78. Y. Yamazaki and N.P. Yao, J. Electrochem. Soc. 128 (1981) 1658.

79. M-B. Liu, G.M. Cook and N.P. Yao, J. Electrochem. Soc. 129 (1982) 239.

80. S. Spzak, C.J. Gabriel, J. Electrochem. Soc. 126 (1979) 1914.

81. M-B. Liu, G.M. Cook and N.P. Yao, J. Electrochem. Soc. 129 (1982) 1390.

82. Y. Yamazaki and N.P. Yao, J. Electrochem. Soc. 128 (1981) 1655.

83. H.N. Seiger, Proc. Intersoc. Energy Convers. Eng. Conf. 16th (vol.1) 1981, 102-110.

84. G.A. Dalin, in Zinc-Silver oxide batteries. A. Fleischer and J.J. Lander ed., Wiley, New York 1971, p.87.

85. S.P. Poa and Ch. Wu, J. Appl. Electrochem. 8 (1978) 427.

86. O. Wagner and A. Himy, in Proc. 27th Power Sources symp., PSC Publications Committee, Red Bank, N.J. 1976, p.135.

87. A. Himy and O. Wagner, in Proc. 28th Power Sources symp., PSC Publications Committee, Red Bank, N.J. 1979, p.167.

88. J.A. Keralla and J.J. Lander, Electrochem. Tech. 6 (1968) 202.

89. J. McBreen and E. Gannon, Electrochim. Acta 26 (1981) 1439.

90. J. McBreen and E. Gannon, J. Electrochem. Soc. 130 (1983) 1980.

91. J. McBreen, E. Gannon, D.T. Chin and R. Sethi, J. Electrochem. Soc. 130 (1983) 1641.

92. J. McBreen, J. Electrochem. Soc. 119 (1972) 1620.

93. K.W. Choi, D.N. Bennion and J. Newman, J. Electrochem. Soc. 123 (1976) 1616.

94. K.W. Choi, D.N. Bennion and J. Newman, J. Electrochem. Soc. 123 (1976) 1628.

95. D.C. Hamby, N.J. Hoover, J. Wirkkala, D. Zannle, J. Electrochem. Soc. 126 (1979) 2110.

96. D.C. Hamby, J. Wirkkala, J. Electrochem. Soc. 125 (1978) 1020.

3. THE ELECTROCRYSTALLISATION OF ZINC FROM ALKALINE MEDIA.

3.1. Introduction.

The electrocrystallisation of zinc has been extensively studied from the technological point of view. The number of publications on this subject is continuously increasing due to the promising features of zinc as electrode material in rechargeable batteries.The complexity of the behaviour of this metal as an electrode is evident from different types of studies and contradictory data found in the literature.
Only few investigations (see for example references [1,2]) have been carried out on the first stages of the deposition of zinc. However, these studies still lack the detailed analysis of the very initial stages such as the initial formation of monolayers and the initial nucleation and three-dimensional growth of centres.

It is now well established [3] that detailed information about the kinetics of electrocrystallisation can be obtained readily from the initial stages of the potentiostatic deposition on foreign substrates. The electrocrystal-lisation of nickel, an irreversible process, was recently examined [4] by this technique and it was shown that the computer-based analysis of the initial stages of the deposition [5], according to the relevant general electrocrystallisation models [6], gives direct information as to the kinetics of nucleation, the kinetics of crystal growth in two and three dimensions, the morphology of the deposit and the role of 'overlap' of growth centres, etc.

The main aim of the work reported in this chapter is to explore the extent to which such studies can be used to derive similar information about a reversible process, the electrocrystallisation of zinc.

3.2. Theory.

Derivation of current-time equations for electrocrystallisation processes requires as a pre-requisite the correct calculation of the actual area of growth centres at any time, t, prior to and after the coalescence of centres. It was pointed out recently [7,8] that the statistical treatments of overlap [9] used for such calculations account for all ingestion of sites due to their coverage by the growth processes, but ingestion of sites due to the conversion of sites into nuclei are not accounted for; this type

of ingestion must then be taken into consideration by introducing a
nucleation law [7,8]

$$N = \frac{A}{A'} \quad (1 - \exp - A't) \tag{3.1}$$

where A (nuclei cm^{-2} s^{-1}) is the initial rate of nucleation, A' (s^{-1}) is the
rate of conversion of a site into a nucleus and N (nuclei cm^{-2}) is the total
number of nuclei which can be formed in time t in the absence of growth
processes. If nucleation is progressive in time and occurs at only N_0 (cm^{-2})
preferred sites, then the total number of nuclei which can be formed in
the absence of growth is given by

$$\frac{\dot{A}}{A'} = N_0 \tag{3.2}$$

whereas for the case of progressive nucleation in the absence of such
preferred sites

$$\frac{A}{A'} = \frac{1}{\alpha r_c^2} \tag{3.3}$$

where r_c (cm) is the critical size of a nucleus and α is a packing factor.
General current-time equations for nucleation and two-dimensional growth
of centres together with the concurrent hydrogen evolution [6] give rise
to a transient shown in Fig. 3.1. The initial current in this case rises
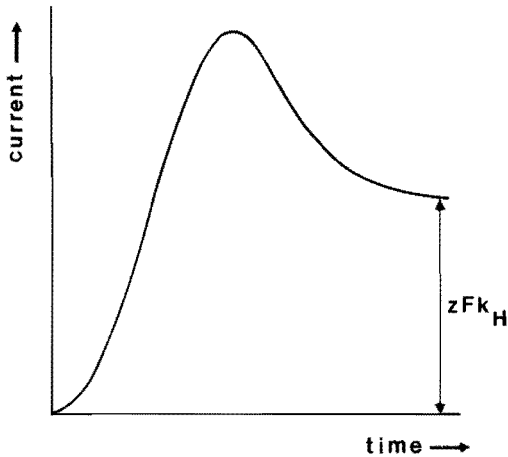

Fig. 3.1 Theoretical current-time transient due to the two-dimensional
          nucleation and growth together with evolution of hydrogen (on
          the tops and at the edges of the growth centres).

with time according to

$$i \sim t^n \tag{3.4}$$

where $2 \geq n \geq 1$ depending on whether A' is very large (n = 1 for A' = ∞) or very small (n = 2 for A' very small compared to the overall rate of the process). The steady-state current is due to hydrogen evolution on top of the monolayer deposit.

The general current-time equation for nucleation and three-dimensional growth of centres whose shapes are approximated by right-circular cones, Fig. 3.2A, is given by [6]

$$i = z \, F \, k' \left\{ 1 - \exp \left[\frac{- \pi M^2 k^2 A}{A' \rho^2} \left(t^2 - \frac{2t}{A'} + \frac{2}{A'^2} - \frac{2}{A'^2} \exp \, (- A't) \right) \right] \right\} \tag{3.5}$$

where k' (moles $cm^{-2} \, s^{-1}$) and k (moles $cm^{-2} \, s^{-1}$) are the rates of crystal growth in the direction perpendicular and parallel to the substrate, and M (g mol^{-1}) and ρ (g cm^{-3}) are the molecular weight and the density of the deposit, respectively.
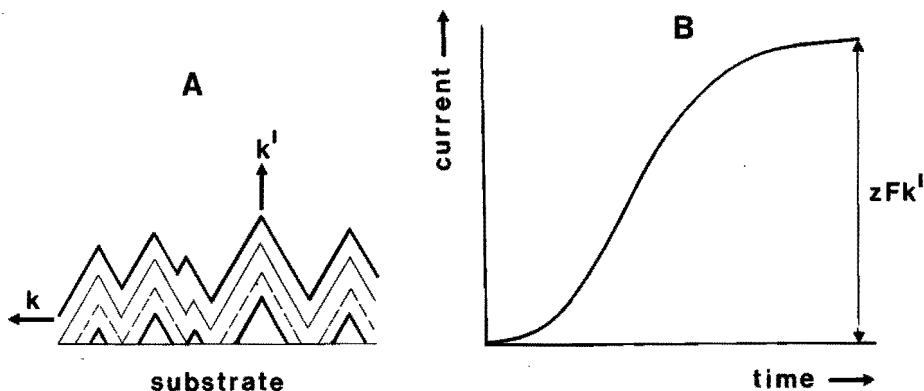

Fig. 3.2 A. Growth of right-circular cones, viewed at four different times.
          B. Current-time transient according to equation (3.5).

Equation (3.5) has two limiting forms. If the nucleation is instantaneous (i.e. A' = ∞; N = A/A' = N_0), the current-time equation is given by

$$i = z \, F \, k' \left\{ 1 - \exp \frac{- \pi M^2 k^2 N_0}{\rho^2} t^2 \right\} \tag{3.6}$$

22

If the nucleation is progressive and $\frac{1}{A'}$ is large compared to the overall time, the current-time equation is given by

$$i = z F k' \left\{ 1 - \exp \frac{- \pi M^2 k^2 A}{3\rho^2} t^3 \right\} \qquad (3.7)$$

The above Eqs. (3.5), (3.6) and (3.7) predict an asymptotic approach of current to a constant value, $z F k'$ (A cm^{-2}), Fig. 3.2B. However, the transients for the deposition of nickel [4,5] and cobalt [10] on a vitreous carbon electrode show that the current goes through a maximum. The appearance of this maximum current in the initial stages of the potentiostatic deposition

of nickel has been explained by the mechanism of 'death' and synchronised 'rebirth' [5] of new centres: a mechanism also observed [11] by electron microscopic studies of the initial stages of the deposition of nickel onto {111} single crystal copper.

It has recently been shown [12] that nucleation, growth and overlap of hemispherical centres, also considered later in this paper, can adequately explain the transients of the electrocrystallisation of nickel without further assumptions of 'death' and 'rebirth' processes.

3.3. <u>Experimental</u>.

The electrocrystallisation of zinc was studied on silver electrodes in alkaline zincate solutions. Measurements were made in a conventional three-compartment cell at 295 ± 1 K, using a Wenking potentiostat (68 FR.5) and a Universal Programmer (PAR 175); the current-time transients were recorded on a Kipp (BD8 multirange) chart recorder. The reference electrode is an Hg/HgO electrode and all potentials are given with respect to this electrode. The counter electrode is a high purity zinc rod.

A polycrystalline silver rod electrode of purity 99.95% and 6 mm in diameter, embedded in KelF was polished with successively finer grades of alumina (down to 0.05 μm); the electrode was then cleaned by pouring firstly fast running tap water and then double distilled water over it. The experimental work was carried out in 10 M KOH + 0.5 M ZnO solutions prepared from AnalaR Chemicals and double distilled water. The solutions were freshly prepared prior to each set of experiments.

The Ag electrode, in each experiment, was inserted into the cell at 0.0 V; the potential was then stepped to the value E_r (which was previously

determined as being the rest potential of a pure zinc rod in the solution
in use) for a period long enough for the background current to fall to a
steady low value. Next, a further step to the appropriate working potential
was applied so as to initiate the electrocrystallisation of zinc. The
overpotentials, here defined as the difference $E - E_r$, were varied between
24 and 35 mV.

3.4. Results.

3.4.1. General Features of the Initial Stages of the Electrodeposition of Zinc.

Fig. 3.3 illustrates the initial part of the current-time transient observed
for the potentiostatic deposition of zinc onto a polycrystalline silver
electrode at a potential of $- .1.381$ V ($E_r = -1.355$ V). In the time range
$0 < t < t_1$ the deposition of a layer can be observed (peak A).
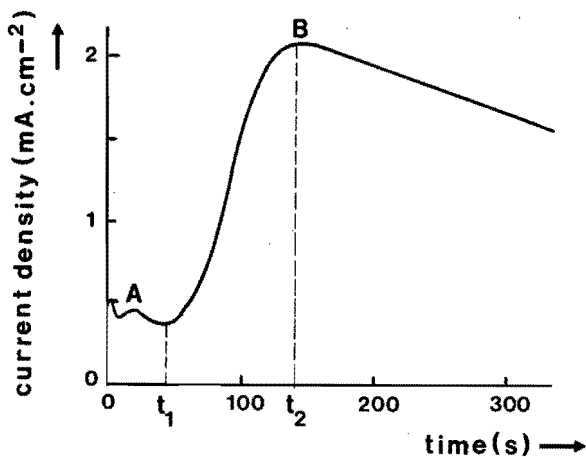

Fig. 3.3 Initial part of the current-time transient of the deposition of
          zinc onto a polycrystalline silver electrode at −1.381 V (vs.
          Hg/HgO).

At $t > t_1$ nucleation and three-dimensional growth of centres take place.
The growth of these centres in the direction parallel to the substrate
is impeded by their coalescence during the later stages. The current goes
through a maximum at $t = t_2$ (peak B) and decreases rather slowly compared
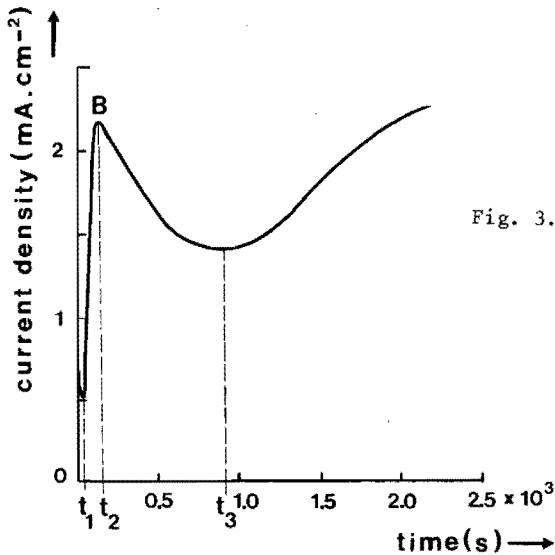to the rising portion of the transient.

Fig. 3.4 The extended longer-time part of the transient shown in Fig. 3.3.

Fig. 3.4 shows the longer-time features of the transient shown in Fig. 3.3. It can be seen that the current after falling to a relatively low value at $t = t_3$ slowly rises again, indicating the 'rebirth' of new centres on the top of the underlying deposit and their subsequent growth into the solution.

Successive increase in overpotential drastically decreases the time scale and increases the current scale at which peaks A and B occur (see Fig. 3.5 at $E = -1.385$ V and Fig. 3.6 at $E = -1.390$ V). Overlap of the two transients (one observed at $t < t_1$ and the other at $t > t_1$, Fig. 3.3) and a larger increase of the current peak A, with respect to that of B, is also observed.
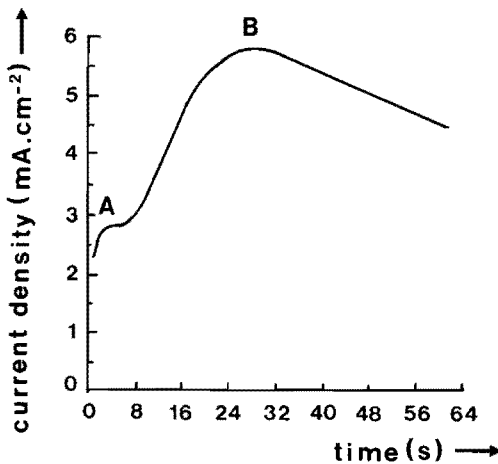

Fig. 3.5
Initial part of the current-time transient of the deposition of zinc onto a polycrystalline silver electrode at -1.385 V (vs. Hg/HgO).
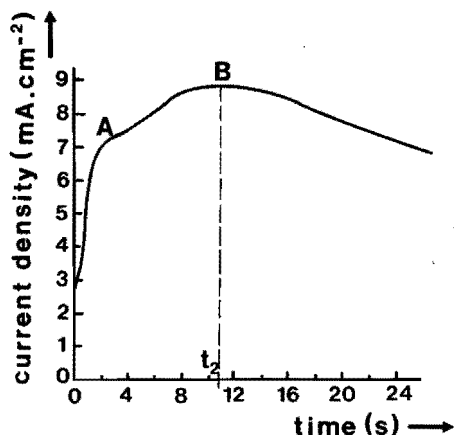
25

Fig. 3.6

Initial part of the current-time transient of the deposition of zinc onto a polycrystalline silver electrode at -1.390 V (vs. Hg/HgO).

3.4.2. Detailed Analysis of the Initial Stages.

The formation of the layer of deposit observed in the time range $0 < t < t_1$ (Fig. 3.3), is by no means the first layer formed on a silver substrate. Potential sweep measurements (Fig. 3.7) show at cathodic potentials smaller than that of Fig. 3.3, monolayer/adsorption peaks prior to the formation of this layer, as also found in [13]. The relatively large, diminishing background current observed in Fig. 3.3 at the very beginning of the transient is thus mostly due to fast formation of these initial layers which, however, are not investigated in this paper.

If the layer, observed in the above time range is assumed to be formed via a two-dimensional nucleation and growth process with concurrent evolution of hydrogen at the edges and on the tops of the growth centres, then
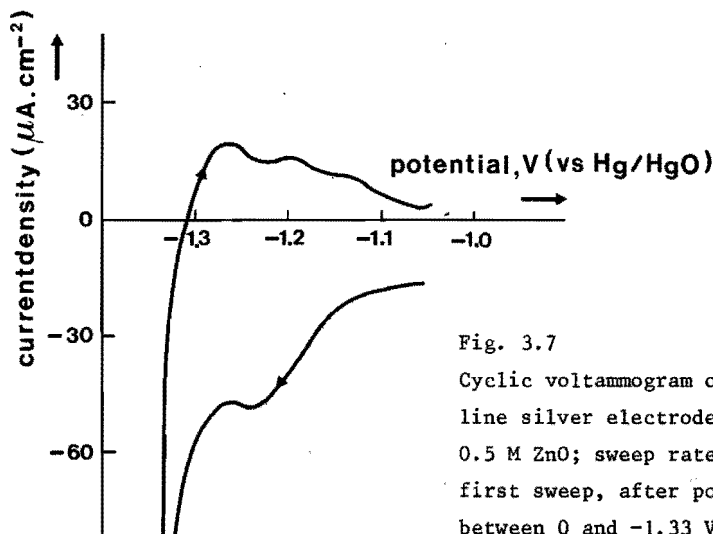

Fig. 3.7
Cyclic voltammogram of a polycrystalline silver electrode in 10 M KOH + 0.5 M ZnO; sweep rate: 10 mV/s; first sweep, after polishing, between 0 and -1.33 V.

at time t_1 (when the monolayer formation is completed) the current is given by

$$i_H = z \, F \, k_H \qquad (3.8)$$

where k_H (moles $cm^{-2} \, s^{-1}$) is the rate constant for the evolution of hydrogen on the top surface of the full layer. The nucleation and three-dimensional growth of centres must then take place on the top of this already deposited layer. Assuming right-circular cone growth forms, the total current-time equation describing the transient, in the time range $t_1 < t < t_2$ is given by Eqs. (3.5) and (3.8):

$$i = i_H + z \, F \, k' \left\{ 1 - \exp \left[- \frac{\pi \, M^2 k^2 A}{A'\rho^2} \left((t-t_1)^2 - \frac{2(t-t_1)}{A'} + \frac{2}{A'^2} \right. \right. \right.$$
$$\left. \left. \left. - \frac{2}{A'^2} \exp - A' \, (t-t_1) \right) \right] \right\} \qquad (3.9)$$

provided that there are no other processes, such as the 'death' and 'rebirth' of crystal growth. Fig. 3.8 is the computer fit of the experimental transient, Fig. 3.3, in the above time range to this equation. It is worthwhile to note that the nucleation rate constant $A'(s^{-1})$ is directly obtained by this computer fit.
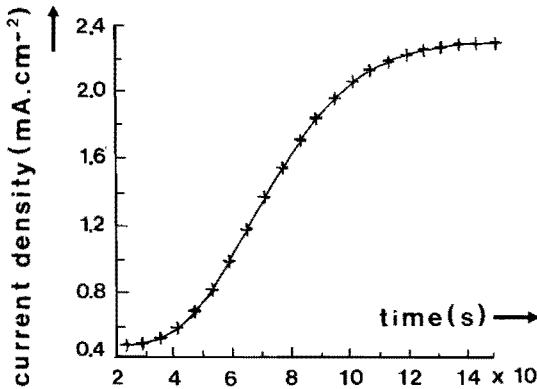

Fig. 3.8   The part of the current-time transient shown in Fig. 3.3 in the time range $t_1 < t < t_2$
+ + : experimental data ; —— : theoretical fit of equation (3.9)
Derived parameters: A' $= 0.11 \pm 0.02 \ (s^{-1})$;
i_H $= 0.479 \pm 0.003 \ (mA \ cm^{-2})$; t_1 $= 24.3 \pm 0.8 \ (s)$;
k' $= (0.931 \pm 0.002) \ 10^{-8} \ (moles.cm^{-2}.s^{-1})$;
$k^2 A/A'$ $= (0.161 \pm 0.003) \ 10^{-6} \ (moles^2.cm^{-6}.s^{-2})$;
standard error of fit : $0.36 \ 10^{-2} \ (mA.cm^{-2})$.

27

A computer fit of the same experimental data of Fig. 3.3 in this time range, $t_1 < t < t_2$, to the simplified form of Eq. (3.9) for progressive nucleation (Eq. 3.7 + 3.8), shows that the fit is slightly less than in Fig. 3.8 (standard error of fit: $0.17 \ 10^{-1}$ mA cm^{-2}), indicating that Eq. (3.7) is indeed only an approximation of the general relation (Eq. 3.5).

The current-time transients obtained at higher potentials (E = -1.385 V (Fig. 3.5); E = -1.390 V (Fig. 3.6)) show that here, evidently, the mechanism of two-dimensional nucleation and growth can no longer be an adequate description of the first transient peak. Indeed, when these transient data are fitted to the current-time equations (describing monolayer formations simultaneously with nucleation and three-dimensional growth of centres on the top of the two-dimensional growth centres), large negative values for the evolution of hydrogen and negative rate constants are obtained; i.e.: this model is no longer operative.
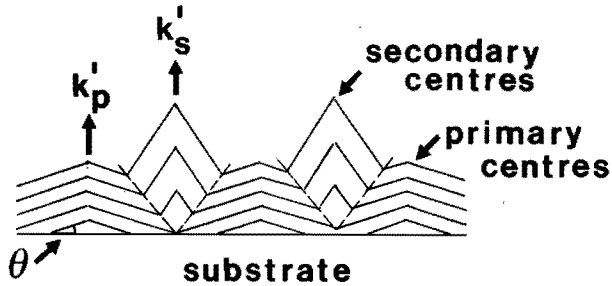

Fig. 3.9   Growth of secondary right-circular cone centres at sites where primary centres coalesce
θ = contact angle of the primary centres.

In order to explain the current-time behaviour at higher potentials we propose a model, in which nucleation and three-dimensional growth of primary centres, having low contact angle, θ, (Fig. 3.9) at low over-potential, are followed by nucleation of secondary three-dimensional growth centres at the junctions where coalescence of the primary centres occur. We assume in this model that the nucleation is instantaneous. The derivation of the current-time equation for this model is straight-forward. The current, i_p, due to the instantaneous nucleation and three-dimensional growth of primary centres is given by equation (3.6) in the following notation:

$$ i_p = z \ F \ k_p' \left(1 - \exp \frac{-\pi \ M^2 k_p^2 N_0 \ t^2}{\rho^2} \right) \tag{3.10} $$

28

where subscript p denotes that the rates belong to the nucleation and
growth of primary centres. After an induction time, t_1, growth of secondary
centres at junctions where primary centres have coalesced, starts. The
growth of secondary centres affects the total current in two ways, firstly
by decreasing the current (due to the decrease in the actual area of the
primary centres) by an amount of

$$i_{-p} = z \, F \, k_p' \left(1 - \exp \frac{-\pi \, M^2 k_s^2 \, N_0}{\rho^2} (t-t_1)^2 \right) \qquad (3.11)$$

and secondly by increasing the current by

$$i_s = z \, F \, k_s' \left(1 - \exp \frac{-\pi \, M^2 k_s^2 \, N_0}{\rho^2} (t-t_1)^2 \right) \qquad (3.12)$$

where subscript s refers to the secondary centres. A complete description
of the transient, Figs. 3.5 and 3.6, up to the second maximum must, moreover,
also include the initial diminishing background current. If we assume
that the fall in the background current, i_b, is related to the coverage
of the primary growth centres, then

$$i_b = i_b' \exp \left(\frac{-\pi \, M^2 k_p^2 \, N_0 t^2}{\rho^2} \right) \qquad (3.13)$$

where i_b' is the value of current observed at $t = 0$.

Derived parameters:

i_b' = 1.69 ± 0.04 (mA cm^{-2})

k_p' = $(0.1429 \pm 0.0002) \, 10^{-7}$ (moles cm^{-2} s^{-1})

$k_p^2 \, N_0$ = $(0.22 \pm 0.01) \, 10^{-2}$ (moles^2 cm^{-6} s^{-2})

k_s' = $(0.2973 \pm 0.0002) \, 10^{-7}$ (moles cm^{-2} s^{-1})

$k_s^2 \, N_0$ = $(0.309 \pm 0.003) \, 10^{-4}$ (moles^2 cm^{-6} s^{-2})

t_1 = 5.26 ± 0.03 (s)

standard error of fit : $0.68 \, 10^{-2}$ mA.cm^{-2}

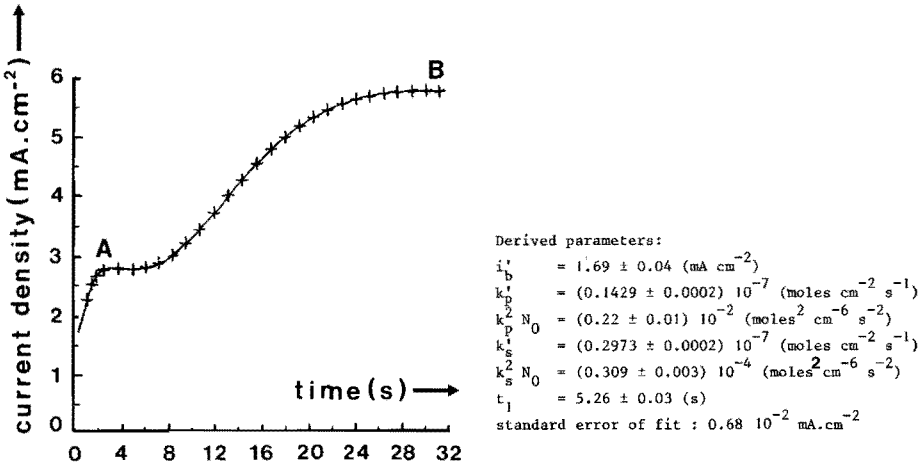Fig.3.10 (Initial) current-time transient of the deposition of zinc onto
          a polycrystalline silver electrode at -1.385 V (vs. Hg/HgO)
          + + : experimental data ; —— : theoretical fit of equation (3.14)
          and (3.15)

The total current is then given by

$$i = i_b + i_p \quad \text{for } t \leq t_1 \tag{3.14}$$

and by

$$i = i_b + i_p - i_{-p} + i_s \quad \text{for } t \geq t_1 \tag{3.15}$$

Figs. 3.10 and 3.11 show the computer fit of the experimental transients at potentials of -1.385 V and -1.390 V to the above equations (3.14) and (3.15).
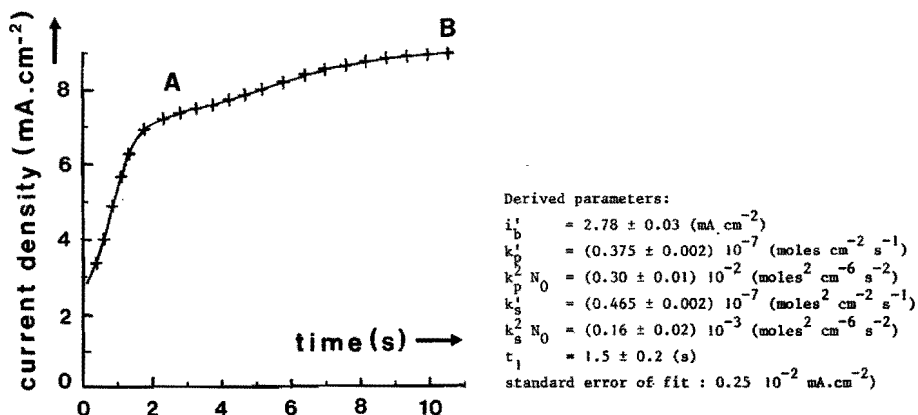

Derived parameters:

i_b' $= 2.78 \pm 0.03$ (mA cm^{-2})
k_p' $= (0.375 \pm 0.002)$ 10^{-7} (moles cm^{-2} s^{-1})
$k_p^2 N_0$ $= (0.30 \pm 0.01)$ 10^{-2} (moles^2 cm^{-6} s^{-2})
k_s' $= (0.465 \pm 0.002)$ 10^{-7} (moles^2 cm^{-2} s^{-1})
$k_s^2 N_0$ $= (0.16 \pm 0.02)$ 10^{-3} (moles^2 cm^{-6} s^{-2})
t_1 $= 1.5 \pm 0.2$ (s)
standard error of fit : 0.25 10^{-2} mA.cm^{-2})

Fig. 3.11   Initial current-time transient of the deposition of zinc onto a polycrystalline silver electrode at -1.390 V (vs. Hg/HgO) + + : experimental data ; —— : theoretical fit of equation (3.14) and (3.15)

In Fig. 3.12, k_s', the growth rate constant of the secondary centres in the direction perpendicular to the substrate, is plotted against the over-potential. In this small potential region a nearly linear relation is obtained, indicating that the linearized form of the Butler-Volmer relation is valid

$$i = z \, F \, k_s' = i_o \, \frac{z \, F \, \eta}{RT} \tag{3.16}$$

in which i_o is the exchange current density. The calculated i_o-value is about 100 A/m^2 (related to the geometric area of the electrode). In the literature [14-16] i_o-values of 200-3100 A/m^2 are given. It is a moot question whether this i_o-value can be compared with the i_o-values for the $Zn \to Zn^{2+}$-reaction, as determined in the literature.
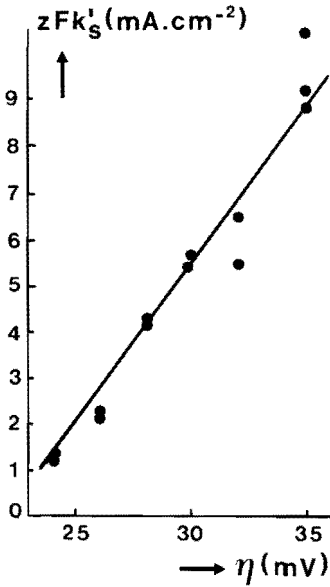
Fig. 3.12
Plot of $z F k_s'$ against η.
k_s' = rate of growth of the secondary centres in the direction perpendicular to the substrate, as obtained by curve fitting.

The growth of the secondary centres starts after an induction period (t_1) which decreases at higher overpotentials.

The reproducibility of the derived parameters is good, if we take into account the variation in the surface of the silver substrate for each experiment and the sensitivity of the different parameters on the overvoltage.

The transient according to equations (3.15) and (3.9), however, deviates from the experimental data at longer times as equations (3.15) and (3.9) predict an asymptotic approach of current to a constant value. This will be discussed later on.

Experimentally the current increases again after a decrease beyond the point B, resulting in a minimum at $t = t_3$ (Fig. 3.4). On fitting the equations for nucleation and three-dimensional growth of centres to the transient, Fig. 3.4 at $t > t_3$, a good fit is obtained, indicating that the deposit in this range is again formed via the nucelation and 3 D-growth. This deposit appeared to be mossy.

3.5. Discussion.

The transient behaviour of nucleation and growth of conical forms were
considered in the theoretical section. The initial transient current is
mainly governed by factors which affect the coverage of the substrate,
such as the shape of the basal plane of the growth centres and the
operative nucleation and growth laws. The actual topography of the
centres exerts influence after their coalescence and becomes the dominating
factor for the transient shape after the full coverage. The very good fit
of the transients for zinc to the equations indicates that the nucleation
and three-dimensional growth of centres are indeed responsible for the
initial stages. We note that models based on right-circular cone growth
forms predict an asymptotic approach of current to a steady-state value
and further assumptions about the cessation of growth above and over that
due to the coalescence are necessary. Furthermore, the current-time
transients over a range of overpotentials were explained by two models,
one at low(Fig. 3.3)and the other at higher overpotentials (Figs. 3.5 and 3.6).
We like to point out that the above models can be replaced by only one
model in which no further assumptions are needed. In this model (Fig. 3.13)
spherical-cap growth centres instead of right-circular cones are considered.
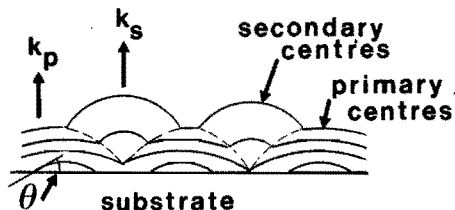

Fig. 3.13 Growth of secondary hemispherical centres at sites where the
           primary centres coalesce.

Whereas continued growth of the conical centres following overlap preserves
the topography of the surface,Fig. 3.2A(so that the current approaches a
limit,Fig. 3.2B), the continued growth of spherical cap centres leads to
a smoothing of the surface, Fig. 3.14A(with hemispherical caps). The current-
time equation based on nucleation law [1] for the growth of such centres
is complicated; here we only consider the current-time equations developed
[12] for the nucleation and growth of hemispherical centres ($\theta = \frac{\pi}{2}$ in
Fig.3.14A)based on the two limiting cases of
a) *Instantaneous* conversion of N_0 (cm^{-2}) sites into nuclei, for which the
current is given by

$$i \simeq \frac{2\,z\,F\,\pi\,M^2\,k^3\,N_0\,t}{\rho^2}\,\exp\left(-\frac{\pi\,M^2\,k^2\,N_0\,t^2}{\rho^2}\right)\int_o^t \exp\frac{\pi\,M^2\,k^2\,N_0\,u^2}{\rho^2}\,du \qquad (3.17)$$

b) *Progressive* nucleation when $\frac{1}{A^T}$ is large compared to the overall time of growth for which

$$i \simeq \frac{z\,F\,\pi\,M^2\,k^3\,A}{\rho^2}\,\exp\left(-\frac{\pi\,M^2\,k^2\,At^3}{3\rho^2}\right)\int_o^t (t^2-u^2) \qquad (3.18)$$

$$\exp\frac{-\pi\,M^2\,k^2\,A}{3\rho^2}\,(2\,u^3 - 3\,tu^2)\,du$$

Both these equations predict a maximum in the current-time behaviour, Fig. 3.14B, except that equation (3.17) predicts an initial current rise proportional to the square of time whereas equation (3.18) indicates an initial rise proportional to the cube of time; both transients reach a steady state value of $z\,F\,k$ at extended times.
However, the correlation between experimental data and theoretical equations is not yet made.
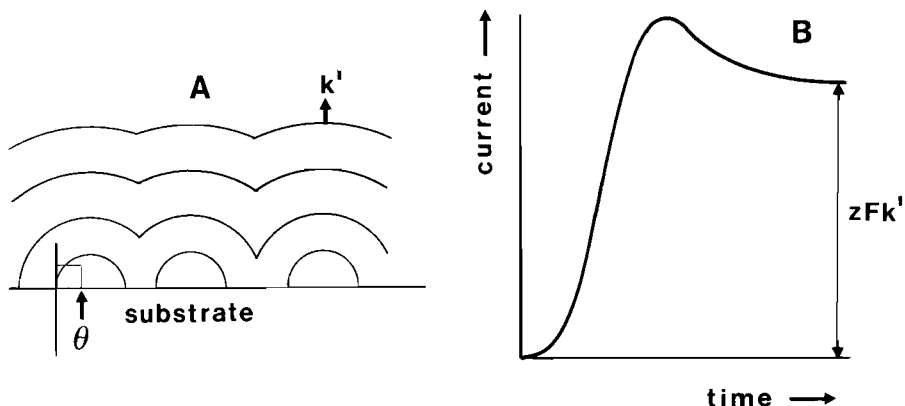

Fig. 3.14 A. Growth of hemispherical cap centres viewed at four different times.

B. Theoretical current-time transient for the mechanism of crystal growth, illustrated in Fig. 3.14A.

In order to find out whether the peak currents observed in Figs. 3.3, 3.5 and 3.6 are due to any transport processes, the deposition of zinc onto a rotating Ag disc electrode is studied.

The current-time transient, (Fig. 3.15), of the potentiostatic deposition
of zinc onto a rotating disc electrode, also shows the presence of peak
currents, indicating that these currents are indeed caused by the decrease
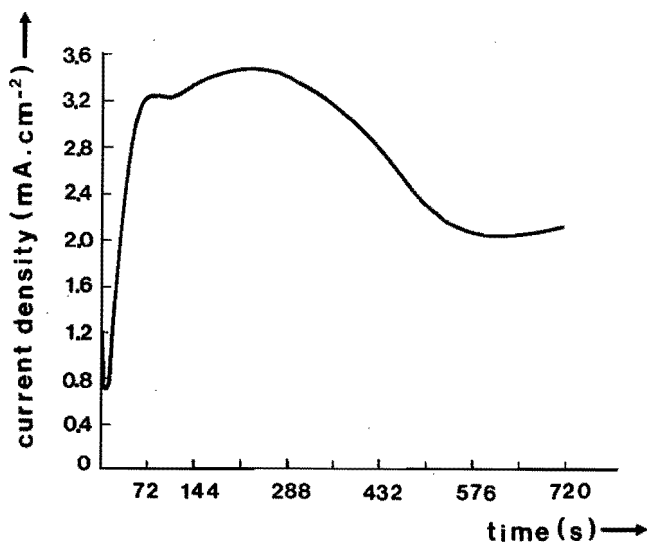of the area of the deposit after coalescence.

Fig. 3.15 Current-time transient of the deposition of zinc onto a rotating
(2000 rpm) polycrystalline silver electrode at −1.382 V (vs.
Hg/HgO).

In practice zinc is deposited at high rates where the reaction is pre-
dominantly controlled by the diffusion of species through the solution.
Here we have only studied the deposition at low rates, i.e. at low over-
potentials, as the detailed information about the nucleation and growth
mechanism can be easily followed and understood under these conditions.
Further insight into the complexity of the behaviour of zinc is clearly
required for a variety of experimental conditions.

3.6. Conclusions.

Measured i-t transients for electrodeposition of zinc from an alkaline
medium onto a silver substrate were compared with calculated transients
for models of crystal nucleation and growth.

The electrocrystallisation of zinc is found to go through the following
stages:

1. adsorption/underpotential monolayer formation of zinc followed by:
2. the formation of a thin layer by nucleation and three-dimensional growth
   of primary centres, with a low contact angle at low overpotential (24 mV)
   and an increase in this contact angle at higher overpotential;
3. the formation of a second layer by nucleation and 3 D-growth of secondary
   centres, at low overpotential on the top of the first layer and at higher
   overpotential at the junctions where the primary centres coalesce.
   The primary and secondary nucleation and crystal growth lead to the
   formation of a compact deposit, prior to:
4. nucleation and three-dimensional growth of centres leading to the
   formation of a loose mossy deposit.

3.7. Literature.

1. F. Mansfeld and S. Gilman, J. Electrochem. Soc. 117 (1970), 588.
2. A.R. Despic, Proceedings of the Third Symposium on Electrode Processes,
   The electrochemical Soc. Inc., Princeton, N.J. (1979) pp. 235.
3. M. Fleischmann and H.R. Thirsk, in "Advances in Electrochem. and
   Electrochemical Engineering" Vol. III, ed. Delahay and Tobias,
   Interscience, New York (1963).
4. M.Y. Abyaneh and M. Fleischmann, Trans. Inst. Met. Fin., 58 (1980), 91.
5. idem, J. Electroanal. Chem., 119 (1981), 197.
6. ibid, 119 (1981), 187.
7. M.Y. Abyaneh, Ph.D. Thesis, Southampton University 1980.
8. M.Y. Abyaneh and M. Fleischmann, The Analysis of Nucleation and Overlap
   in Crystal Growth Processes, in press.
9. M. Avrami, J. Chem. Phys. 7 (1939), 1103; ibid 8 (1940), 212;
   ibid 9 (1941), 177.
10. M.Y. Abyaneh, E. Barendrecht and H. Zeilmaker, under preparation.
11. N. Itoh, N. Yamazoe and T. Seiyama, Surface Tech. 5 (1977), 27.
12. M.Y. Abyaneh, Calculation of Overlap for Nucleation and Three-dimensional
    Growth of Centres, submitted for publication.
13. G. Adzic, J. McBreen and M.G. Chu, J. Electrochem. Soc. 128 (1981), 1691.
14. J.O'M Bockris, Z. Nagy and A. Damjanovic, J. Electrochem. Soc. 119
    (1972), 285.
15. N.A. Hampson, G.A. Herdman, R. Taylor, J. Electroanal. Chem. 25 (1970), 9.
16. T.P. Dirkse and N.A. Hampson, Electrochimica Acta 17 (1972), 135;
    ibid 17 (1972), 383; ibid 17 (1972), 1113.

4. INTERACTION OF ZINC DEPOSITED FROM AN ALKALINE SOLUTION WITH A POLYCRYSTALLINE SILVER SUBSTRATE.

4.1. Introduction.

Zinc electrodeposition on silver is of technological importance because of the use of a silver current collector in zinc secondary batteries [1]. Adžić et al. [2] studied the adsorption onto and the alloy formation of zinc with silver. They found that underpotential deposition and alloy formation takes place.

In relation with the study of the nucleation and three dimensional growth of zinc centres onto silver [3, 4], a detailed examination of the deposition of zinc onto silver and their interaction was started using cyclic voltammetry, microprobe technique and ellipsometry. Because cyclic voltammetry and ellipsometry can be applied simultaneously, it is expected to get more information about the surface reactions.

4.2. Experimental.

The electrochemical measurements were made in a conventional three-compartment glass cell at 295 ± 1 K, using a Wenking potentiostat (68 FR.5) and a Universal Programmer (PAR 175); the cyclovoltammograms were recorded on an X-Y recorder (HP-7046 A). The reference electrode is an Hg/HgO electrode and all potentials are given with respect to this electrode. The counter electrode is a high purity zinc rod. The working electrode is a polycrystalline silver rod of purity 99.95% and 6 mm in diameter, embedded in KelF, such that only the flat base was exposed to the electrolyte.

The pretreatment of the surface substrate is as follows: polishing with successively finer grades of alumina (down to 0.05 μm) and cleaning by pouring firstly fast running tap water and then double destilled water over it. Before each experiment this pretreatment was carried out.

The electrolyte is a 10 M KOH + 0.5 M ZnO solution and was prepared from Analar Chemicals and double destilled water. The solutions were freshly prepared prior to each set of experiments.

Cyclic Voltammetry

All the cyclic voltammetric studies were made with a rotating electrode (2000 RPM, to avoid mass transport limitation), in voltage regions more negative than 0.0 V to avoid the oxidation of the substrate. The voltage scan rate is 10 mV s^{-1}.

Microprobe

A Jeol microprobe apparatus was used. The penetration depth of the electron-beam is about 0.2 μm (at the voltage of 5 kV).

The samples were prepared as follows. The zinc was deposited on the silver electrodes by a sweep (10 mV s^{-1}) to -1.5 V (negative to the restpotential of zinc in the solution (-1.36 V)). By varying the arrest times at certain potentials (-1.25 V; -0.45 V) in the anodic sweep, different samples are obtained. After removal from the electrolyte, the electrode was washed in fast running tap water, double destilled water, rinsed in ethanol and dried in air.

Ellipsometry

Simultaneous electrochemical and ellipsometric measurements were made in a KelF cylindrical cell with quartz windows fixed for an angle of incidence of 70° at the mounted working electrode (0.7 cm^2). The counter electrode is a platinum sheet (± 3 cm^2). The reference electrode is an Hg/HgO electrode. The ellipsometer was a Rudolph automatic ellipsometer model RR 2000 equipped with tungsten iodine light source and monochromatic filter for 546.1 nm.

4.3. Results.

4.3.1. Cyclic Voltammetry.

Fig. 4.1 shows a cyclic voltammogram on a polycrystalline silver electrode in the E-range 0.0 to -1.43 V in 10 M KOH + 0.5 M ZnO. The deposition of zinc (A) and, during the subsequent anodic sweep, the dissolution of the bulk-zinc (B) and other anodic peaks (C and D) can be clearly discerned. When the electrode, after the deposition of zinc, is held at -1.36 V (the restpotential of zinc in this solution), peaks C and D become more pronounced (Fig.4.2). These peaks were found to depend upon the contact time of the zinc layer with the silver substrate. Moreover, the condition of the surface, whether zinc is present eg. at its restpotential -1.36 V, or at -1.25 V, when the bulk-zinc has been dissolved during the anodic sweep, influences the anodic peaks C and D.

Fig. 4.3 shows the dependence of the anodic charges (Q) under the peaks C and D on the arrest times at -1.36 V (= t_1) and at -1.25 V (= t_2). Q_C and Q_D are found to be proportional to the square root of time t_1. In Table 4.1 the slope of the Q vs. $\sqrt{t_1}$ lines are tabulated as function of the arrest time at -1.25 V (= t_2).
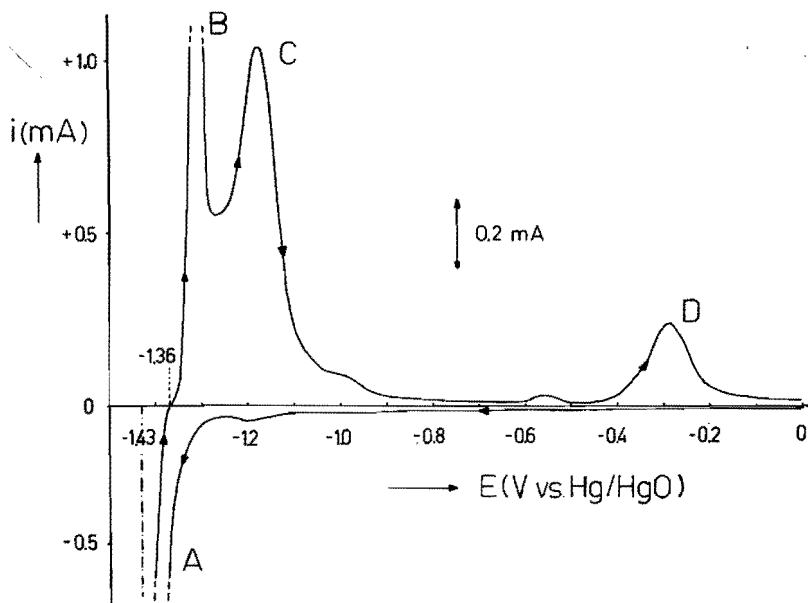
Fig. 4.1 Cyclic voltammogram on a polycrystalline silver electrode (0.28 cm^2) in the E-range 0.0 to -1.43 V in 10 M KOH + 0.5 M ZnO (2000 RPM).
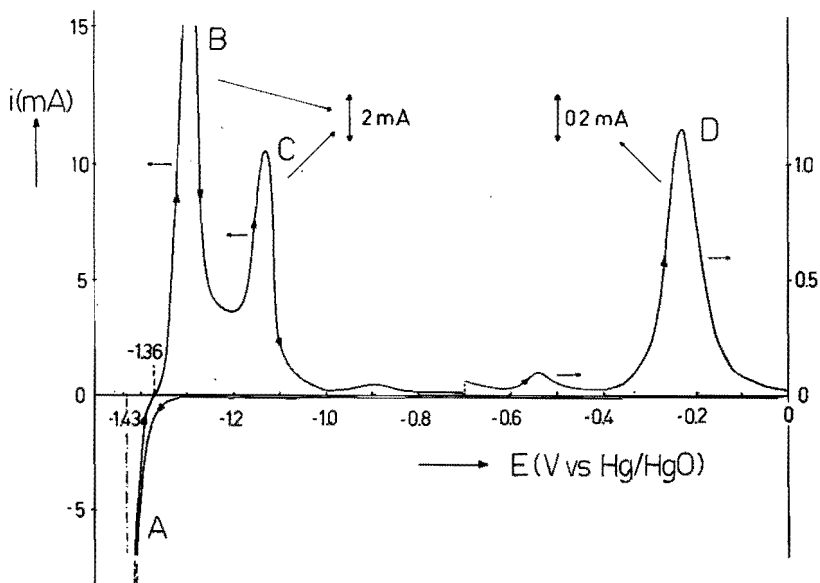

Fig. 4.2 Cyclic voltammogram on a polycrystalline silver electrode (0.28 cm^2) in the E-range 0.0 to -1.43 V in 10 M KOH + 0.5 M ZnO (2000 RPM), with an arrest time of 15 min at -1.36 V, the restpotential of zinc.
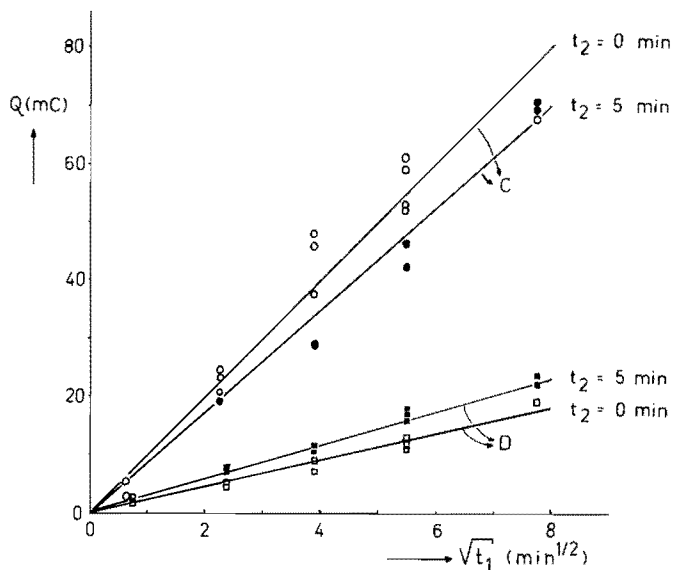
Fig. 4.3 Dependence of the anodic charges under peaks C and D on the arrest
times at −1.36 V (= t_1) and −1.25 V (= t_2).

Table 4.1   slope Q_C vs. $\sqrt{t_1}$, Q_D vs. $\sqrt{t_1}$ and $Q_C + Q_D$ vs. $\sqrt{t_1}$ as function
of the arrest time at −1.25 V (= t_2).

t_2 (min)	slope Q_C vs. $\sqrt{t_1}$ ($mC.min^{-\frac{1}{2}}$)	slope Q_D vs. $\sqrt{t_1}$ ($mC.min^{-\frac{1}{2}}$)	slope $Q_C + Q_D$ vs. $\sqrt{t_1}$ ($mC.min^{-\frac{1}{2}}$)
0	9.8 ± 0.6	2.3 ± 0.1	12.1 ± 0.7
1	7.9 ± 0.4	2.5 ± 0.1	10.4 ± 0.5
5	6.8 ± 0.6	2.9 ± 0.1	9.7 ± 0.7

4.3.2. Ellipsometry.

Fig. 4.4a shows the change in Δ and ψ during a potential sweep in the
E-range 0.0 to −1.39 V.

Fig. 4.4b shows the corresponding voltammogram. Significant changes in
Δ and ψ occur at the same potentials where deposition and dissolution
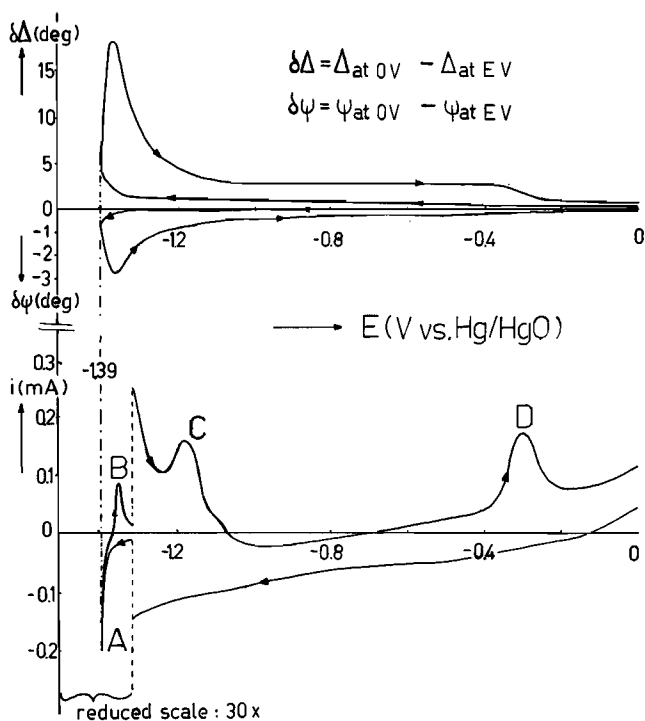peaks are observed in the cyclic voltammogram.

Fig.4.4a. Change in Δ and ψ during a potential sweep on a polycrystalline silver electrode (0.7 cm^2) in the E-range 0.0 to -1.39 V in 10 M KOH + 0.5 M ZnO.

   b. Corresponding cyclic voltammogram.

Under the before mentioned sweep conditions, Δ and ψ reach a maximum, resp. minimum at the moment when the maximum amount of zinc is deposited ($\sim$ 20 mC/cm^2). This means that in the potential range -1.39 to -1.365 V Δ still increases and ψ decreases. Δ and ψ become nearly constant after both peaks B and C are dissolved and reach final values at 0.0 V, that are within 0.5° the same as the initial values at 0.0 V. If, after the cathodic sweep, the anodic sweep is arrested at the restpotential of zinc, -1.36 V, for ten minutes, Δ and ψ become nearly constant during this arrest period. On resuming the anodic sweep, larger changes in Δ and ψ than in Fig. 4.4a are observed. Also peaks C and D are increased.
Fig. 4.5 shows the result when more zinc is allowed to deposit ($\sim$ 100 mC/cm^2), by making the reversal potential more cathodic (-1.42 V). Δ reaches a maximum at -1.42 V, while ψ reaches a minimum at -1.36 V on the anodic
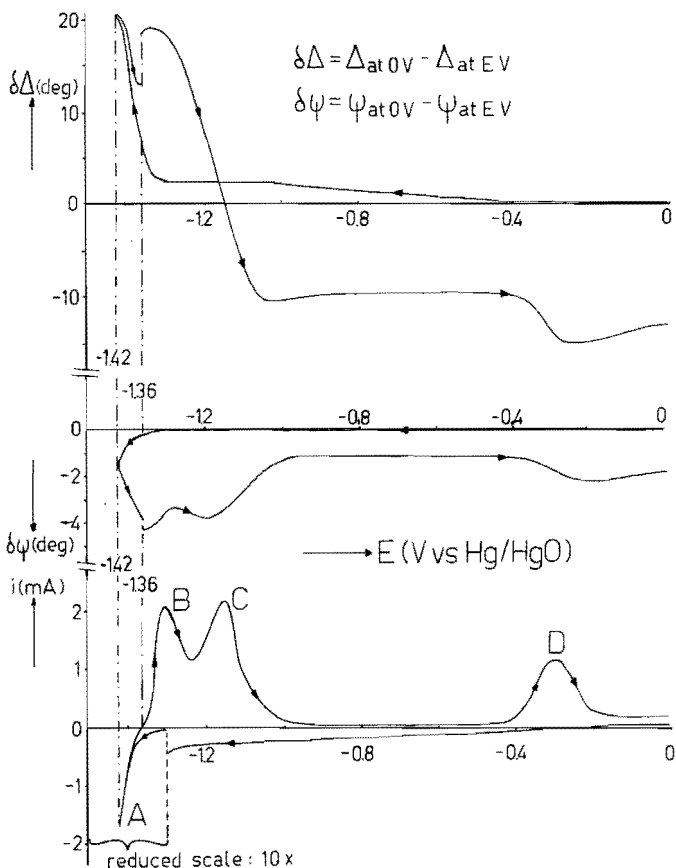
40

Fig. 4.5   Change in Δ and ψ during a potential sweep on a polycrystalline
silver electrode (0.7 cm^2) in the E-range 0.0 to -1.42 V in
10 M KOH + 0.5 M ZnO, plus corresponding cyclic voltammogram.

sweep. When now the sweep is arrested at the restpotential on the anodic
sweep, Δ and ψ do not become constant. Moreover, the final values of
Δ and ψ at 0.0 V are now different from the initial values. It was found
that this difference between the final and initial values of Δ and ψ
depends on the reversal potential and on the time of arrest at -1.36 V.
When such an electrode, with final values of Δ and ψ different from the
initial values, is thereafter repeatedly subjected to a potential sweep
between 0.0 V and a potential, just cathodic of the zinc restpotential,
the values of the ellipsometric parameters Δ and ψ at 0.0 V slowly return
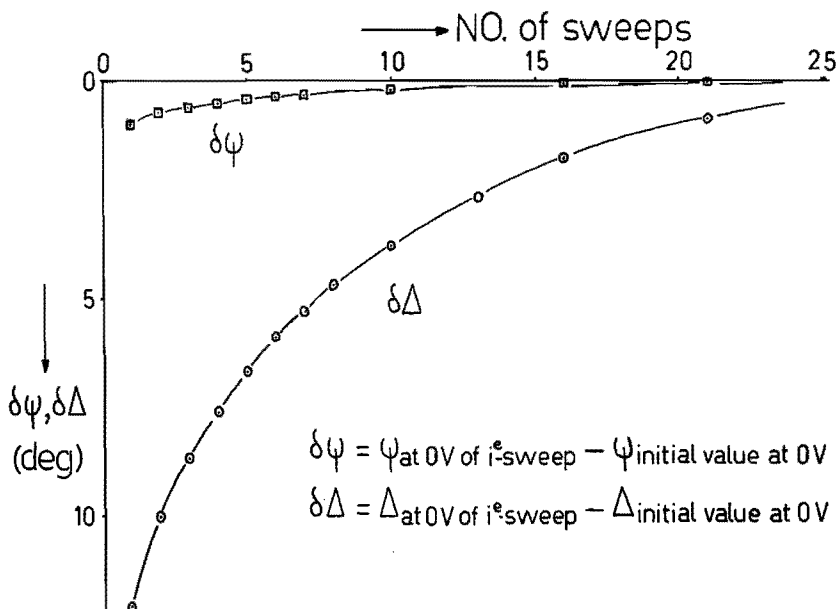to the initial values (Fig. 4.6).

Fig. 4.6   Dependence of $\delta\Delta$ and $\delta\psi$ on the number of sweeps, between 0.0 V and a potential, just cathodic of the zinc restpotential.

4.3.3. Microprobe.

To further analyse the peaks C and D, microprobe measurements are carried out.
Table 4.2 summarizes the microprobe results for the silver-zinc system.
The two different samples are prepared by a potential program as pictured in Fig. 4.7.

Table 4.2   Microprobe results of Ag substrate samples, prepared as shown in Fig. 4.7.

	Percentage (at. %)		Total wt %
	Ag	Zn	Ag and Zn
Sample I	22 ± 3	78 ± 3	91 ± 1
Sample II	55 ± 3	45 ± 3	95 ± 2

Combination of the results in Table 4.2 and the phase diagram of silver and zinc (Fig.4.8) point out that the ε-phase (alloy $AgZn_3$) is present on the surface of sample I and the ξ-phase (alloy AgZn) on the surface of sample II. Also, traces of other elements are present i.e. oxygen and silicium.
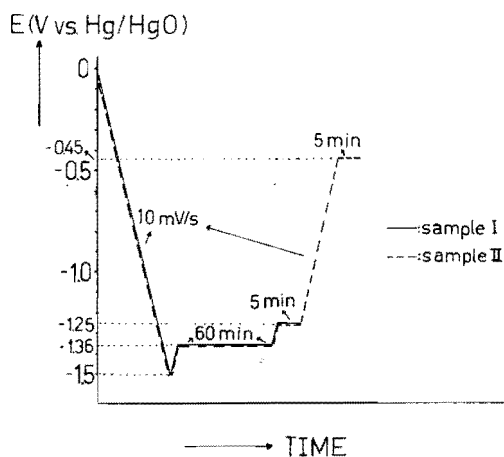

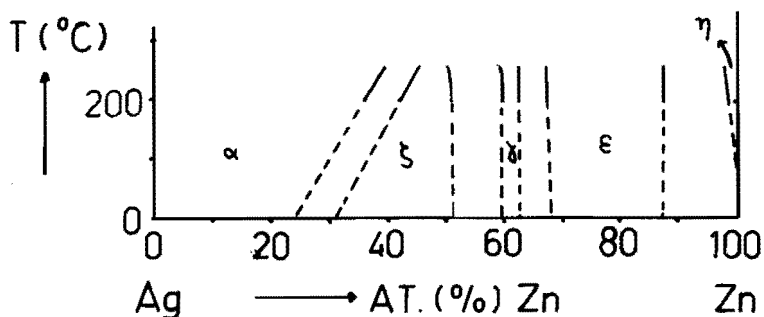Fig. 4.7   Potential program of silver substrate samples in 10 M KOH + 0.5 M ZnO (2000 RPM).

Fig. 4.8   Phase diagram of silver and zinc [5], extrapolated to room temperature.

4.4. Discussion.

With the cyclovoltammetric technique the formation of two phases is indicated: C at −1.15 V and D at −0.25 V (and a very small one at −0.55 V).
With the microprobe technique two of these could be identificated: C is the ε-phase (alloy $AgZn_3$) and D is the ξ-phase (alloy AgZn). These phases are

formed by interdiffusion of zinc and silver as indicated by the dependence
of the anodic charges on the square root of the arrest time (t_1) at the
restpotential of zinc (Fig. 4.3). It is seen from Table 4.1, that with increasing
t_2 the slope Q_C vs. $\sqrt{t_1}$ decreases, whereas the slope Q_D vs. $\sqrt{t_1}$ increases.
With removal of excess Zn, by arresting the potential at −1.25 V, so that
bulk-zinc dissolves, some $AgZn_3$ is transformed into AgZn. In this trans-
formation process $AgZn_2$ is probably an intermediate (small peak at −0.55 V).
It is very likely that this transformation takes place already during the
zinc deposition.

Moreover, it is also seen from Table 4.1 that the total charge $(Q_{AgZn_3} + Q_{AgZn})$
decreases with time t_2. This could indicate that these phases are transformed
into another phase of Ag and Zn, probably the α-phase, in which zinc is
soluble up to about 25 atomic percent at room temperature [5]. The dissolution
of the zinc in the α-phase probably will not occur at a potential more
negative than 0.0 V and so this zinc will remain in the substrate. This explains
why a great discrepancy exists in the initial part of the current-time
transient of the potentiostatic deposition of zinc onto a freshly, mechanically
polished silver surface and the deposition on a 'cycled' silver surface i.e.
a silver surface on which already zinc was deposited and dissolved (Fig. 4.9).
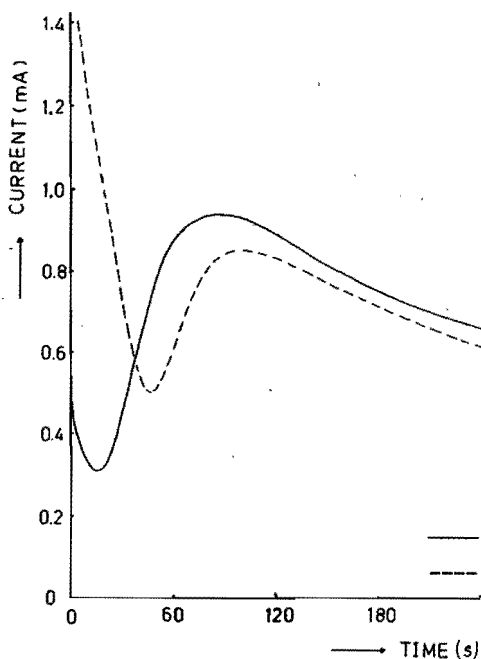

Fig. 4.9

Initial part of the current-time
transient of the deposition of
zinc onto a polycrystalline
silver electrode (0.28 cm^2) at
−1.39 V.

——— : after mechanically polishing

---- : after an anodic sweep up to 0 V.

The difference between the final and initial values at 0.0 V of the ellipso-
metric parameters Δ and ψ, caused by an arrest time at -1.36 V, could be
explained by the formation of the α-phase during zinc deposition.
This is also supported by an experiment in which the deposited zinc layer
had a contact time of a few weeks with the substrate. Then, in the cyclic
voltammogram, a peak appeared at a potential positive to 0.0 V.
The microprobe results also indicate that oxygen and silicium are present,
oxygen probably by oxidation of zinc at the surface after removal of the
electrode from the cell, and silicium because of the use of a glass cell.
Because diffusion of zinc and silver through different phases takes place,
it is not possible to calculate one single diffusion coefficient: the
diffusion coefficient involves the diffusion of a component in a uniform
phase. Therefore, calculation of a more general penetration constant is
carried out, which gives a rough indication of the penetration rate of zinc
into silver. Calculation of a penetration constant (K) of zinc and silver
is possible with :

$$K = \frac{(\Delta x)^2}{2t} \qquad (4.1)$$

where Δx is the penetration depth (cm) and t the penetration time (sec). [6]
Δx is proportional to the total charge $(Q_{tot} = Q_\varepsilon + Q_\zeta)$ of the zinc species
of the two phases, via correlation coefficient α

$$\Delta x = \frac{Q_{tot}}{\alpha} \qquad (4.2)$$

Combination of (4.1) and (4.2) gives

$$K = \frac{1}{2\alpha^2} \frac{(Q_{tot})^2}{t} \qquad (4.3)$$

The correlation coefficient α can be determined by calculating the amount
of zinc atoms per volume unit in the phases and correlating this amount
with the charge of the dissolved zinc of the phases. This can be done as
follows.
The number of atoms (x) per volume unit in the two phases can be determined
with use of the lattice parameters in the phases [7]

$$x_\varepsilon = \frac{2}{\frac{\sqrt{3}}{2} a_\varepsilon^2 \cdot c_\varepsilon} \qquad ; \qquad x_\zeta = \frac{1}{a_\zeta^3} \qquad (4.4)$$

where a and c are the lattice parameters.

The number of the zinc atoms (y) per volume unit in the two phases is equal to

$$y_\varepsilon = \frac{3}{4} \cdot x_\varepsilon \quad ; \quad y_\xi = \frac{1}{2} x_\xi \qquad (4.5)$$

Multiplying y with a factor (nF/N) results in the amount of charge (q) per volume unit, needed for dissolving the zinc species in the two phases

$$q_\varepsilon = \frac{nF}{N} \cdot y_\varepsilon \quad ; \quad q_\xi = \frac{nF}{N} \cdot y_\xi \qquad (4.6)$$

where N is Avogadro's number, n is the charge number of zinc and F is the Faraday constant. Combination of (4.4), (4.5) and (4.6) gives

$$q_\varepsilon = \frac{nF}{N} \cdot \frac{3}{4} \cdot \frac{2}{\frac{\sqrt{3}}{2} a_\varepsilon^2 c_\varepsilon} \qquad (4.7a)$$

$$q_\xi = \frac{nF}{N} \cdot \frac{1}{2} \cdot \frac{1}{a_\xi^3} \qquad (4.7b)$$

These q's are the separate contributions of the two phases to the correlation coefficient α.

With use of the ratio (β) of the charge of the zinc species in the two phases, given in Fig. 4.3,

$$\beta = \frac{Q_C}{Q_D} \qquad (4.8)$$

α can be obtained

$$\alpha = \frac{\beta}{1 + \beta} q_\varepsilon + \frac{1}{1 + \beta} q_\xi \qquad (4.9)$$

Combination of (4.7a), (4.7b) and (4.9) gives

$$\alpha = \left(\frac{\beta}{1 + \beta}\right) \cdot \left(\frac{nF}{N}\right) \cdot \frac{\sqrt{3}}{a_\varepsilon^2 c_\varepsilon} + \left(\frac{1}{1 + \beta}\right)\left(\frac{nF}{N}\right) \frac{1}{2} \frac{1}{a_\xi^3} \qquad (4.10)$$

Using equation (4.3), K can be calculated.
If the value of the slope Q_{tot} (= Q_C + Q_D) vs. $\sqrt{t_1}$ in Table 4.1, is taken at t_2 = 0, then K has a value of 7 x 10^{-14} cm^2/s. Adžić and McBreen [2] calculated a diffusion coefficient with a value of 3.10^{-12} cm^2/s and Schmidt et al. [8] estimated a value of $D < 10^{-14}$ cm^2/s.

These diffusion coefficients can not be compared with the calculated penetration constant.

Calculation of the optical constants of the deposited zinc and of the two zinc alloys is possible with use of a computer program in which the thickness of the deposited layer, the optical constants of the substrate and the solution, and the measured ellipsometric parameters Δ and ψ has to be inserted. For the calculation of the optical constants of the deposited zinc layer the following assumptions were made:

- The zinc deposit is a uniform layer upon the smooth silver surface, with the geometric surface taken as the true surface.
- No interaction takes place between the zinc and the silver layer.
- The total amount of the cathodic charge applied is only used for the zinc reduction.
- One layer zinc deposit needs 400 $\mu C/cm^2$ and has a thickness of 2.3 $\overset{\circ}{A}$ (calculated with use of the atomic radius of the zinc atom and the h.c.p.- structure of the zinc lattice [7].

Using the values for Δ and ψ of the interface Ag|Zn|solution at the rest-potential of zinc on the anodic sweep, the optical constants N and K are calculated for different thicknesses of the deposited zinc layer. The calculated values differ considerably from the literature values of zinc [9], even for thin deposits, when the deposit time was only a few seconds. This is an indication that the simplified model, as assumed here i.e. a zinc layer upon the silver substrate without any interaction between silver and zinc cannot be applied. There must be a rather fast formation of alloys by inter-diffusion of silver and zinc and this can explain the discrepancy.

Also, the change of Δ and ψ with time at the restpotential of zinc indicates that diffusion takes place at the interface, independent of current flow. The dependence of the difference between the final and initial values of Δ and ψ on the arrest time t_1 (at the restpotential), and the amount of deposited zinc implies that not all the zinc is removed from the silver substrate during the anodic sweep. Probably, some remaining zinc is present in the α-phase and can only be removed at more positive potentials. By repeatedly sweeping without arrest time, the remaining part of the zinc in the α-phase can dissolve.

Besides the alloy formation by interdiffusion there is another factor which influences the ellipsometric parameters Δ and ψ. This factor is the surface roughening, caused by the interdiffusion process. Between these two factors, alloy formation and surface roughening can not be discriminated by ellipso-metry. Because of this, we did not try to calculate the optical constants of the different alloys.

4.5. Conclusions

Zinc forms alloys with the substrate via diffusion. Two phases are identified: one as the ε-phase ($AgZn_3$) and the other as the ξ-phase ($AgZn$). A penetration coefficient (k) of 7.10^{-14} cm^2/s is calculated. Transformations into phases with lower zinc content take place continuously, probably resulting in the formation of the α-phase.

4.6 Literature

1. S.U. Falk and A.J. Salkind, "Alkaline Storage Batteries", pp. 163-167, John Wiley & Sons. Inc., New York (1969).
2. G. Adžić, J. McBreen, M.G. Chu, J. Electrochem. Soc. 128 (1981) 1691.
3. M.Y. Abyaneh, J. Hendrikx, E. Barendrecht, W. Visscher, 32th I.S.E. Meeting, Dubrovnik/Cavtat, 1981. (Ext. Abstr. B.12).
4. M.Y. Abyaneh, J. Hendrikx, E. Barendrecht, W. Visscher, J. Electrochem. Soc. 129 (1982) 2654.
5. M. Hansen, "Constitution of Binary Alloys", pp. 62-65, McGraw-Hill Book Comp., New York (1958).
6. K. Hauffe, "Reaktionen in und an Festen Stoffen", Springer Verlag, Berlin (1966).
7. A. Taylor et al., Crystallographic Data on Metal and Alloy Structures, Dover Publications Inc., New York (1962).
8. E. Schmidt, M. Christen, P. Beyelar, J. Electroanal. Chem. 42 (1973) 275.
9. American Institute of Physics Handbook, 6-118, McGraw-Hill Book Comp. Inc., New York (1963).
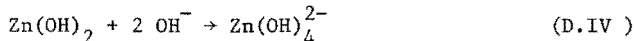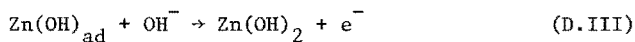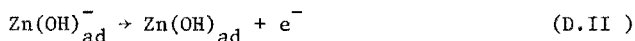
5. THE ELECTRODEPOSITION AND -DISSOLUTION OF ZINC AND AMALGAMATED ZINC IN ALKALINE SOLUTIONS.

5.1. Introduction.

Several mechanisms have been proposed for the zinc reaction in alkaline media, based on contradictory experimental results. For the amalgamated electrode less information is available. In an actual battery system, however, the zinc electrode is usually amalgamated to hinder self-discharge of the battery during which hydrogen is formed. On the other side, it has been found that amalgamation accelerates the Shape Change [1-4]. Therefore and in order to gain more insight in the effect of amalgamation on its kinetic behaviour, the zinc electrode and amalgamated zinc electrodes prepared differently were studied with the galavanostatic transient technique in 1.5 - 10 M KOH.
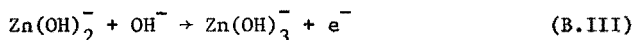
5.2. Review.

Several mechanisms for the zinc electrode were proposed. One of them, that of Dirkse and Hampson, is as follows [5-12]:

$$Zn_{kink} + OH^- \rightarrow Zn(OH)^-_{ad} \qquad (D.I \ )$$

$$Zn(OH)^-_{ad} \rightarrow Zn(OH)_{ad} + e^- \qquad (D.II \ )$$

$$Zn(OH)_{ad} + OH^- \rightarrow Zn(OH)_2 + e^- \qquad (D.III)$$

$$Zn(OH)_2 + 2\ OH^- \rightarrow Zn(OH)_4^{2-} \qquad (D.IV \ )$$

In this mechanism, written for the anodic process, reaction (D.II) is rate determining at very short times. On a longer time scale (> 10 μs) or at high overpotential, the formation of kink sites, associated with reaction (D.I), becomes rate determining. The mechanism is based on galvanostatic transient measurements at very low overpotentials (< 10 mV) in 1 - 10 M KOH. It was found that the exchange current density, i_o, decreased as the measuring time increased. The authors did not correct for the ohmic potential drop, because in their view this drop may be neglected in such concentrated electrolytes. They also performed potentiostatic measurements at high overpotentials, but observed a maximum in the transient [12]. In double pulse measurements the maximum disappeared, but no straight Tafel lines were obtained. According to Dirkse, this behaviour is caused by adsorption of an intermediate [12].

Dirkse has also pointed out that the ionic strength of the electrolyte must play an important role [10,13]. At high KOH concentration (> 4 M)

there is almost no "free" water because it is almost totally attached
to the ions present. This will have a strong effect on the activity
coefficient of the OH^--ion. Dirkse therefore has carried out some measure-
ments at constant ionic strength (with the aid of KF, for F^- is iso-
electronic with OH^-) in order to maintain the water activity constant.
A second mechanism is that of Bockris et al. [14]:

$$Zn + OH^- \rightarrow Zn\ OH + e^- \qquad\qquad (B.I\ )$$

$$ZnOH + OH^- \rightarrow Zn(OH)_2^- \qquad\qquad (B.II\ )$$

$$Zn(OH)_2^- + OH^- \rightarrow Zn(OH)_3^- + e^- \qquad\qquad (B.III)$$

$$Zn(OH)_3^- + OH^- \rightarrow Zn(OH)_4^{2-} \qquad\qquad (B.IV\ )$$

In this mechanism, reaction (B.III) is the rate determining step (RDS),
both in anodic and cathodic direction. The first two steps of the
mechanism (B.I + B.II) are derived from theoretical arguments. Bockris
et al. come to their conclusions on the basis of galvanostatic and potentio-
static transient measurements in $0.1 - 3$ M KOH, both at very low and high
overpotentials. Compensation for the IR-drop was found to be necessary
even using a special reference electrode construction in which this
electrode could be placed as close as 0.0025 cm to the working electrode.
The results of the potentiostatic and the galvanostatic experiments were
identical. Bockris et al. also determined reaction orders with respect to
OH^- and $Zn(OH)_4^{2-}$, in both anodic and cathodic direction. In their opinion
the formation of kink sites is not rate determining because the i_o
obtained from extrapolation of the Tafel line was identical with the value
from experiments at very low overpotential. The same mechanism was also
found by other workers from steady state measurements [15]. Their results
from transient measurements, however, were not consistent with this
mechanism. This is a good example of the contradictory information regarding
the kinetics of the zinc electrode.
About the amalgamated electrode as used in actual battery systems, almost
no kinetic information is available. Dirkse has performed some experiments [16]
in order to prove that in this case charge transfer is rate determining,
and not the formation of kink sites. The amalgamated electrode must then be
regarded as a "liquid", which implies that kink site formation cannot play
a role in the electrode processes. He found that indeed the amalgamated
electrode gave rise to higher current densities than the zinc electrode for
a given overpotential. The resulting mechanism has the same reaction sequence
as for the zinc electrode, only the RDS is now shifted to reaction D.II.
More information is available about the mechanism of the zinc amalgam

50

electrode. The question arises, however, if these results can be applied
to the amalgamated zinc electrode: amalgam experiments make use of a
mercury drop in which a small amount of zinc is dissolved, being the
reverse of an amalgamated electrode, in which a small amount of mercury
is introduced onto solid zinc. Even the proposed mechanisms for zinc
amalgam are contradictory: Payne and Bard [17] suggest a similar mechanism
as that of Dirkse and Hampson (Zn_{kink} written as Zn), with conclusions
drawn from potential step chronocoulometry, d.c.polarography and potential
sweep voltammetry experiments, followed by thorough mathematical analysis,
however, Despić et al. [18] suggest a mechanism with a chemical step between
two electron transfer reactions as the RDS. Moreover, they consider water
as a reaction partner.

5.3. Experimental.

The zinc electrode and the amalgamated electrode were studied by means of
the galvanostatic transient technique in alkaline solutions with concen-
trations ranging from 1.5 to 10 M KOH, and in KOH-KF electrolytes at
constant ionic strength. The zincate concentration was varied from
0.011 to 0.4 M.

THE CELL. All experiments were performed in the cell given in Fig. 5.1.
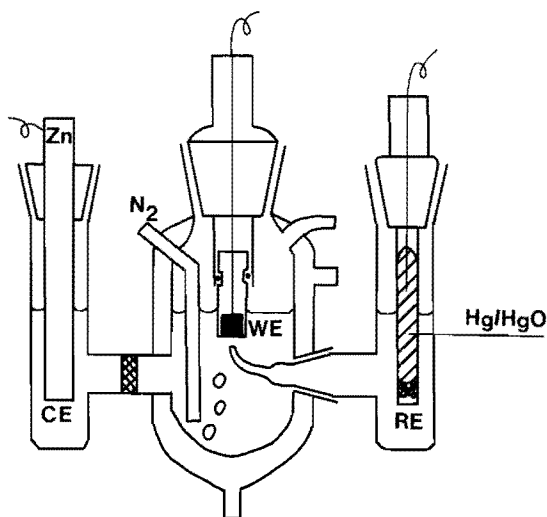
Fig. 5.1 The cell: CE = counter electrode, WE = working electrode,
          RE = reference electrode.

The total cell volume was about 60 ml. The counter electrode (CE) was
made of zinc (99.9% Merck) in order to maintain the zincate concentration
as constant as possible. As a reference electrode (RE) a Hg/HgO-electrode
was used having the same electrolyte as used in the cell. All potentials
are given with respect to this electrode. In general, the distance between
the WE and the trip of the Luggin capillary – RE system was 2 mm in order
to avoid shielding of the electrode. Before each measurement nitrogen was
bubbled through the cell to remove dissolved oxygen. All experiments were
performed at room temperature (20°C).

THE ELECTRODE. The electrode consisted of a polycrystalline zinc rod
(99.9% Merck), machined to 6 mm diameter and embedded in KelF. This
type of electrode construction was also used for the amalgamated zinc
electrodes, which consisted of a proprietary zinc rod containing 1 and 6
wt.% mercury. These pre-amalgamated zinc alloys are manufactured with a
special production technique [19,20] by Metallurgy Hoboken-Overpelt,
Belgium[*]. The electrodes with 1 and 6 wt.% mercury are nominated
Zn(Hg.I) and Zn(Hg.II) resp.

ELECTRODE PRETREATMENT. The zinc and the amalgamated zinc electrodes were
first mechanically polished using SiC paper 600. After this treatment, the
electrode was electrochemically etched in the electrolyte under investi-
gation by varying the potential three to five times from −800 to −1600 mV
vs. Hg/HgO, and back. (Scanrate 50 mV.s^{-1}). During this scan much more
zinc dissolved into the solution than was deposited on the surface. The
result was a shiny electrode in which the separate grains could be clearly
discerned. A third amalgamated electrode (Zn(Hg.III)) was prepared as
follows: the zinc electrode was polished using SiC paper 600 and then
diamond paste 3 μm. The electrode was amalgamated by immersing it for
60 seconds into a solution of 0.3 g $HgCl_2$ in 10 g acetone. The resulting
black film on the electrode surface was wiped off, the electrode was rinsed
with double distilled water and electrochemically etched in the same way
as the zinc electrode. Before each experiment the electrode was amalgamated
and pretreated anew.

CHARACTERIZATION OF THE Zn(Hg,III) ELECTRODE. To characterize the
Zn(Hg,III) electrode two facts are of importance, viz. the total
amount of mercury on the surface and the distribution of the mercury
over and in the zinc. The total amount of mercury on the electrode

---

* Obtained by courtesy of Dr. Meeus.

surface was measured as follows: ten thin circular zinc discs (dia-
meter 8 mm) were amalgamated under the conditions given above.
Thereafter, the discs were dissolved in 25 ml concentrated nitric acid
and the mercury concentration of this solution was measured by atomic
absorption. The mercury content of the zinc electrode was 0.9 mg.cm^{-2}.
Second, it was investigated whether the mercury forms alloys with the
zinc on a time scale of a few hours. The X-ray diffractograms (Cu, Kα)
of the zinc electrode and the amalgamated electrode did not show any
difference. Moreover, the calculated values for the lattice constants
almost coincided with the values on the ASTM card of zinc, thus the
lattice was not stretched due to possible diffusion of mercury into
the zinc lattice.
The distribution of the mercury over the zinc surface was investigated
by electron probe micro-analysis. This technique did not reveal segre-
gation of the mercury. Therefore, it must be assumed that mercury is
distributed regularly over the surface. These findings agree with the
results of Swift et al. [21]. Moreover, they showed that on a time
scale of a few hours no mercury will diffuse into the grains. Such
diffusion had only to be taken into account after a period of four
months.

SOLUTION PREPARATION. The zincate solutions were prepared from analytical
grade chemicals (p.a. Merck) and double distilled water. For the experi-
ments at constant ionic strength KF (p.a. Merck) was used.
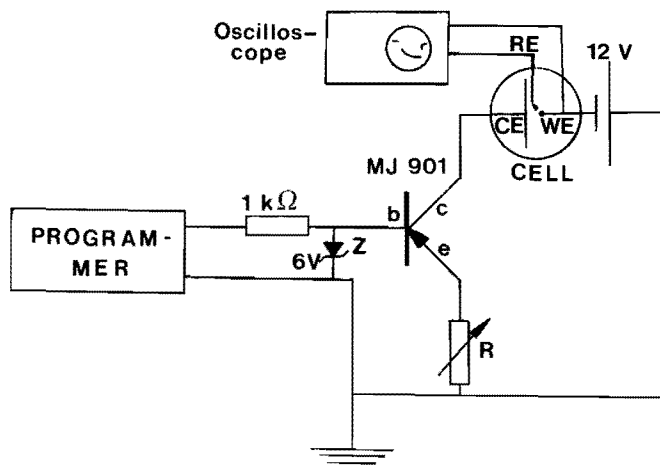
Fig. 5.2   The experimental set-up for experiments in cathodic direction.

MEASURING TECHNIQUE. The galvanostatic pulse technique was used, with
a pulse time of 5 ms or shorter, The set-up is based on a concept of
Bockris et al. [22]. The cathodic set-up is depicted in Fig. 5.2.
In order to be able to apply currents up to 8 A, the high power
Darlington transistor MJ901 was used; the type number of Zener diode Z
was BZX 55C 6V2.
The anodic set-up is similar, however, the Zener diode, the accumulator
and the collector-emitter were placed in reverse order; in this case the
transistor type number was MJ1001.
With these circuits excellent rectangular current pulses were obtained.
The programmer was a PAR potentiostat programmer model 175; the
oscilloscope a Tektronix model 535A.

5.4. Results.

5.4.1. Zinc electrode.

E-t TRANSIENTS. In both the anodic and cathodic Tafel region a distinct
plateau (after charging of the double layer) was observed for the
transients. The ohmic potential drop, which could be read directly from
the oscilloscope screen, could not be neglected since it occasionally
exceeded several times the values for the activation overpotential: the
transients obtained at very low current densities did not reach a constant
value after charging of the double layer. This makes extrapolation to
zero time hazardous; thus, no values for i_o were calculated from these
experiments. At very high current densities the overpotential increased
linearly with time after charging of the double layer, due to concentration
polarization [23]. In this case the linear region was extrapolated to
zero time and the zero-time value was used for calculating the activation
overpotential. Sometimes, a small maximum was observed in the transient.
The possibility of the appearance of such a maximum in the transient for
multistep reactions was evaluated by Plonski [24] for several theoretical
models. According to Selånger [25] the maximum can be explained by poly-
merization of zinc species at the electrode surface. The appearance of
the maximum had almost no effect on the extrapolated value of the activation
overpotential.
It was noted that the activity of the zinc electrode appeared to be a
function of the waiting time at the restpotential. This activity, reflected
in the i_o value, decreased with increasing waiting time. It was tried to

find a pretreatment which would yield a reproducible electrode surface:
applying a high anodic prepulse of 0.5 A cm^{-2} did not have the desired
result, nor did cathodic reduction with hydrogen evolution in 1 M KOH as
recommended by Bockris et al. [14]. It seems, therefore, that the activity
of the electrode is determined by its actual surface state. Consequently,
in order to get as reproducible results as possible, it was decided to
perform the measurements after 10-30 minutes waiting time at the rest-
potential. Within a single measurement the Tafel slope did not depend
on i_o. Values for the capacity of the double layer, calculated from the
slope of the tangent at the very beginning of the transient, were very
high (several hundreds µF cm^{-2}) and showed little variation with solution
composition.

TAFEL LINES. In general, the applied current densities did not exceed
0.5 A cm^{-2}. Measurements at higher i were not possible due to fast
occurring concentration polarization, making the extrapolation to zero
time imposssible. Examples of results for the zinc electrode in 3 M KOH/
0.1 M ZnO in the anodic and cathodic directions are given in Figs. 5.3
and 5.4.
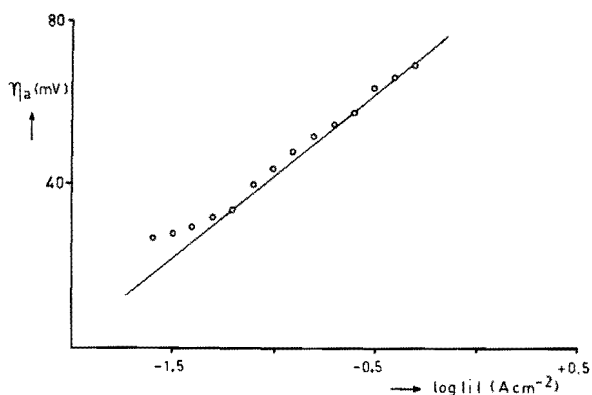
Fig. 5.3
The Tafel line in
anodic direction
for the zinc elec-
trode in 3 M KOH/
0.1 M ZnO.
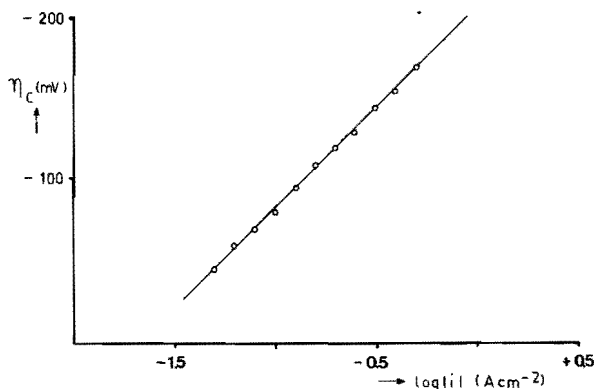
Fig. 5.4
The Tafel line in
cathodic direction
for the zinc elec-
trode in 3 M KOH/
0.1 M ZnO.

55

For all concentrations the anodic Tafel lines are usually linear over
one decade of current density. Most of the cathodic Tafel lines are
linear over a region less than one decade. Results of series of experi-
ments as a function of KOH concentration are summarized in Table 5.1.
(Each experiment is repeated at least five times).

Table 5.1 Measured values of Tafel slope b and of i_o for the zinc electrode as function of KOH concentration.

Electrolyte	anodic				cathodic			
	b_a(mV)	σ_n^*	i_o(A cm^{-2}) x 10^4	σ_n^*	b_c(mV)	σ_n^*	i_o(A cm^{-2}) x 10^4	σ_n^*
1.5 M KOH/0.1 M ZnO	47	6	84	61	105	19	155	61
3 M KOH/0.1 M ZnO	41	12	140	95	130	27	450	330
7 M KOH/0.1 M ZnO	53	16	77	61	137	32	400	320
10 M KOH/0.1 M ZnO	38	11	84	45	137	32	380	240

$^*\sigma_n$ is the standard deviation.

The anodic Tafel slope is about 38 - 53 mV and the cathodic Tafel slope
is about 105 - 137 mV for all concentrations. The reproducibility of the
cathodic Tafel slope was less than of the anodic one, as is indicated
by its standard deviation (σ_n).

RESTPOTENTIALS. In Table 5.2 the restpotentials of zinc vs. Hg/HgO are
given as a function of KOH concentration. The zincate concentration was
0.1 M. The restpotentials showed some fluctuations, probably due to the
interference of hydrogen evolution. Because the corrosion current is low
and i_o of the zinc/zincate couple is high, the restpotentials will differ
only slightly from the equilibrium potentials. These equilibrium potentials

Table 5.2
Measured restpotentials vs. Hg/HgO of the zinc electrode as a function
of the KOH concentration.

Electrolyte	E_r (mV)
1.5 M KOH/0.1 M ZnO	−1332 ± 3
3 M KOH/0.1 M ZnO	−1354 ± 6
7 M KOH/0.1 M ZnO	−1368 ± 4
10 M KOH/0.1 M ZnO	−1376 ± 4

56

were calculated according to the Nernst equation, using the Davies
equation [26] for the activity coefficients, since the activity coeffi-
cients of KOH and $K_2 Zn(OH)_4$, in the presence of each other, are not
known :

$$-\log \gamma_{\pm} = 0.509\ z_+ z_- \left\{ \frac{\sqrt{I}}{\sqrt{I} + 1} - BI \right\} \qquad (5.1)$$

I is the ionic strength of the solution, $\gamma_{\pm}$ the activity coefficient, and
B a constant. Although this empirical equation is valid only for concen-
trations up to 1 M, Boden, Wylie and Spera [26] calculated values of the
activity coefficients for KOH solutions up to 10 M, which almost coin-
cided with the measured values of Akerlof and Bender [27]. The best
agreement was found for B = 0.275. The values for the activity coeffi-
cients of zincate were also calculated with this equation. For the
activity of water, values obtained for NaOH solutions were adopted [28].
The activity of the solids (Zn, Hg/HgO) was considered to be unity.
The calculated equilibrium potentials are presented in Table 5.3.

Table 5.3

Calculated activity coefficients, and equilibrium potentials of zinc
vs. Hg/HgO as a function of KOH concentration.

Electrolyte	a_{H_2O}	γ_{KOH}	$\gamma_{K_2Zn(OH)_4}$	E_r (mV)
1.5 M KOH/0.1 M ZnO	0.95	0.9	0.8	-1332
3 M KOH/0.1 M ZnO	0.88	1.3	1.7	-1352
7 M KOH/0.1 M ZnO	0.62	4.2	17.7	-1368
10 M KOH/0.1 M ZnO	0.38	10.6	113	-1372

From Tables 5.2 and 5.3 one can see that the agreement is excellent.
The restpotentials as a function of zincate concentration in 7 M KOH
are given in Tabel 5.4. In this table are also shown the calculated
values using, again, the Davies equation. From Table 5.4, one can see
that here also the agreement between the measured and the calculated
restpotentials is good.

REACTION ORDER IN HYDROXYL IONS. Because the fluctuations of i_o are a
function of the surface state of the electrode, reaction orders have to

Table 5.4

Measured and calculated restpotentials of zinc in 7 M KOH, as a function of zincate concentration.

Electrolyte	E_r (measured)	E_r (calculated)
0.4 M ZnO	-1353 mV	-1350 mV
0.1 M ZnO	-1367 mV	-1368 mV
0.04 M ZnO	-1375 mV	-1379 mV
0.011 M ZnO	-1386 mV	-1394 mV

be determined from measurements at the same electrode. At each concentration, a galvanostatic run was made to obtain the Tafel lines. After completion of the experiment, the first solution was tested again; indeed the Tafel line was not shifted more than 10 mV. The reaction order with respect to species j, is defined as follows:

$$p_j = \left(\frac{\partial \log i}{\partial \log a_j} \right)_{E, a_i} \tag{5.2}$$

It is necessary to use activities (so to know the activity coefficients) instead of concentrations as done by most authors, because here very high concentrations were used. The fact that the reaction order is defined at constant potential E causes difficulties in the measurement of p with respect to OH^-: in order to plot the Tafel lines with respect to the same reference electrode, the change in equilibrium potential must be known as a function of KOH activity. This change cannot be measured directly since the potential of the RE also changes with the KOH activity. To use a pH independent RE is not desirable, since unknown liquid-junction potentials are so introduced by the different electrolytes in the RE and the WE compartment. Therefore, direct measurement of p is not possible.

An alternative is the calculation of p from the dependence of i_o on KOH activity. For the anodic process

$$i_o = k \, \Pi_i \, a_i^{p_i} \left[\exp \frac{\alpha_a \, z \, F \, E_r}{RT} \right] \tag{5.3}$$

$$\left(\frac{\partial \log i_o}{\partial \log a_j} \right) = p_j + \frac{\alpha_a \, z \, F}{2.3 \, RT} \left(\frac{\partial E_r}{\partial \log a_j} \right) \tag{5.4}$$

58

Consequently, for the cathodic process:

$$\left(\frac{\partial \log i_o}{\partial \log a_j}\right) = p_j - \frac{\alpha_c \, z \, F}{2.3 \, RT}\left(\frac{\partial E_r}{\partial \log a_j}\right) \tag{5.5}$$

Now, $\left(\dfrac{\partial E_r}{\partial \log a_j}\right)$ can be obtained from the Nernst-equation (E_r in Volt vs. NHE):

$$E_r = -1.184 + \frac{RT}{2F} \ln \frac{\gamma_{K_2 Zn(OH)_4} \, c_{K_2 Zn(OH)_4}}{(\gamma_{KOH} \, c_{KOH})^4} \tag{5.6}$$

The activity coefficients can be obtained from equation (5.1). In Table 5.5, the calculated activities of KOH and the restpotentials vs. NHE are given for the different solutions. From these data it follows that $\left(\dfrac{\partial E_r}{\partial \log a_{KOH}}\right) = -87.3$ mV.

Table 5.5
Calculated activities of KOH and restpotentials of the zinc electrode vs. NHE as a function of KOH concentration. The zincate concentration was 0.1 M.

Electrolyte	γ_{KOH}	$\log a_{KOH}$	E_r (mV)
1.5 M KOH	0.9	0.1	−1222
3 M KOH	1.3	0.6	−1270
7 M KOH	4.2	1.4	−1345
10 M KOH	10.6	2.0	−1386

The values of the reaction order p_{OH^-} for the anodic respectively the cathodic process can now be calculated with equation (5.4), c.q. (5.5), using the experimental value of d log i/d log a_{KOH} (0 ± 0.1) and the measured Tafel slopes b_a and b_c which are equal to respectively $\dfrac{2.3 \, RT}{\alpha_a \, zF}$ and $\dfrac{2.3 \, RT}{\alpha_c \, zF}$.

For all concentrations this leads to the values given in Table 5.6.

REACTION ORDERS IN ZINCATE. In contrast to the experiments at different KOH concentrations, the reaction order in zincate can be measured

Table 5.6 calculated reaction order p_{OH^-} for anodic and cathodic process at the zinc electrode as function of KOH concentration.

	p_{OH^-},anodic	p_{OH^-},cathodic
1.5 M KOH/0.1 M ZnO	1.9 ± 0.3	-0.8 ± 0.3
3 M KOH/0.1 M ZnO	2.1 ± 1.0	-0.7 ± 0.3
7 M KOH/0.1 M ZnO	1.7 ± 0.8	-0.6 ± 0.3
10 M KOH/0.1 M ZnO	2.3 ± 1.0	-0.6 ± 0.3

directly. In these experiments the zincate concentration was varied from 0.011 M to 0.4 M, in 7 M KOH. Again activities have to be used instead of concentrations. However, since the ionic strength is about the same for the different solutions, the activity coefficient of zincate should not vary with the zincate concentration. Therefore, we suppose it makes no difference now, whether activities or concentrations are used for the determination of the reaction orders in zincate. The results in the cathodic direction are given in Fig. 5.5. The measured cathodic p-value in zincate is 1.3 ± 0.3. The same experiment in anodic direction gave a value of 0.
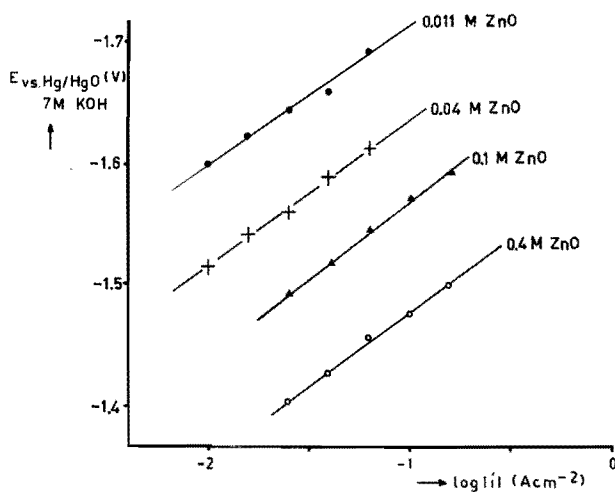
Fig. 5.5 Determination of the cathodic reaction order in zincate for the zinc electrode in 7 M KOH.

EXPERIMENTS AT A CONSTANT IONIC STRENGTH. In order to eliminate the effect of changes in the activity of water as a function of the KOH concentration, experiments were performed at a constant ionic strength of 10 M. As a supporting electrolyte, KF was used. Although the changes in the activity of water can be significant, the results showed that these changes did not make any difference for the zinc electrode reaction. The Tafel slopes remained constant; i_o kept the same order of magnitude.

5.4.2. Amalgamated electrodes.

The transients of the three amalgamated electrodes were different from those obtained at the zinc electrode. First of all, the rise time of the transients was much smaller, caused by a smaller value of C_{DL} and not by an increase of i_o. In general, the values for C_{DL} were about 10 times smaller than in the case of the zinc electrode. Another difference was the behaviour at very low i. In contrast to the zinc electrode a distinct plateau in the E-t transient was observed, thus values for i_o could also be obtained from measurements at low overpotential. In Fig. 5.6, the results of three separate experiments at low overpotential are presented for the Zn(Hg,III) electrode. The other amalgamated electrodes give similar results. It can be seen that, again, the activity of the electrode (i_o) is a function of the actual surface state.
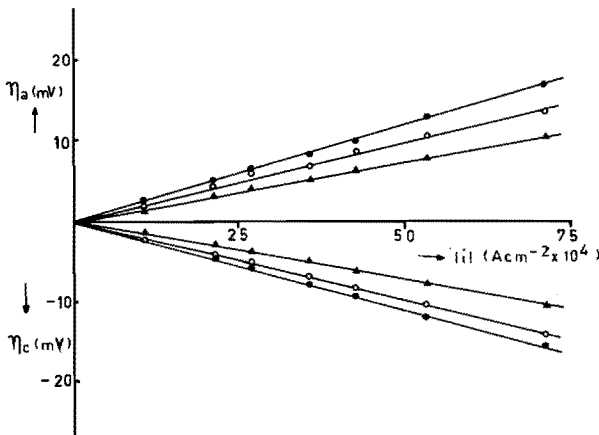
Fig. 5.6 Determination of the i_o for the amalgamated electrode in
          3 M KOH/0.1 M ZnO from measurements at very low η, results
          of three separate experiments ($\bullet$, o, $\blacktriangle$).

TAFEL LINES. The Tafel lines were measured for four different KOH con-
centrations. Typical examples of these experiments are given in Figs.
5.7 and 5.8 (for the anodic, respectively cathodic situation).
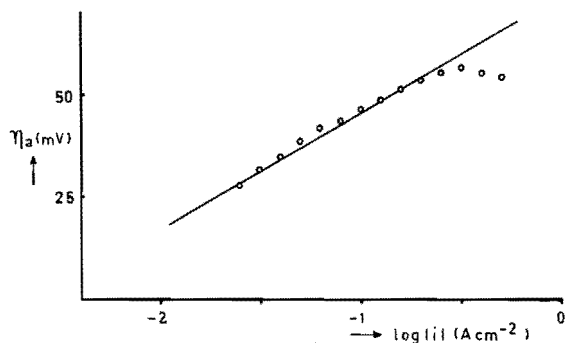

Fig. 5.7 The Tafel line in anodic direction for the amalgamated
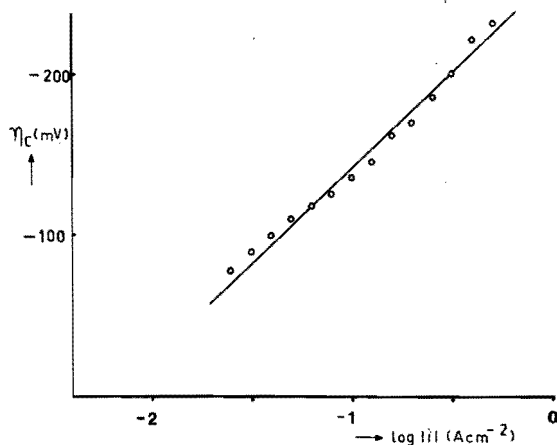   electrode Zn(Hg,III) in 3 M KOH/0.1 M ZnO.

Fig. 5.8 The Tafel line in cathodic direction for the amalgamated
         electrode Zn(Hg,III) in 3 M KOH/0.1 M ZnO.

A deviation of the linear region from the anodic Tafel line at high
current densities was observed for all three amalgamated electrodes
and was probably brought about by a change in the surface state of the
electrode caused by the passage of such a high current. The results of
the complete series of experiments are summarized in Table 5.7.
The kind of amalgamation appears to have almost no effect on the i_o^-,
b_a^- and b_c^--values. The anodic Tafel slope is about 30 - 35 mV for all

concentrations. The cathodic Tafel slope decreases with increasing KOH-concentration: from about 120 mV at 1.5 M to about 50 – 60 mV at 10 M.

Table 5.7

Measured values of Tafel slope b and i_o of the three amalgamated electrodes as a function of KOH concentration. The zincate concentration was 0.1 M.

Electrolyte	Electrode	anodic				cathodic			
		$i_o \times 10^4$ (A cm^{-2})	σ_n	b_a (mV)	σ_n	$i_o \times 10^4$ (A cm^{-2})	σ_n	b_c (mV)	σ_n
1.5 M KOH	Zn(Hg,I)	130	20	34	10	260	100	110	32
	Zn(Hg,II)	80	30	35	8	220	90	120	23
	Zn(Hg,III)	100	20	37	8	130	60	130	20
3 M KOH	Zn(Hg,I)	220	60	34	9	330	70	80	16
	Zn(Hg,II)	120	20	41	11	270	80	93	11
	Zn(Hg,III)	100	80	33	5	230	150	85	20
7 M KOH	Zn(Hg,I)	210	90	29	6	270	80	57	13
	Zn(Hg,II)	170	40	29	6	270	130	60	10
	Zn(Hg,III)	130	60	32	3	170	80	71	22
10 M KOH	Zn(Hg,I)	190	60	30	8	200	60	48	8
	Zn(Hg,II)	130	40	30	3	200	20	51	5
	Zn(Hg,III)	140	50	36	6	190	50	56	4

RESTPOTENTIALS. In Table 5.8 the restpotentials of the amalgamated electrode are given as a function of KOH concentration. It can be seen that these values are about 15 mV more negative than the values for zinc. This is probably caused by a change in E^o and/or the activity of Zn, due to amalgamation.

Table 5.8

Measured restpotentials vs. Hg/HgO of the amalgamated electrode as a function of KOH concentration.

Electrolyte	E_r (mV)
1.5 M KOH/0.1 M ZnO	-1342 ± 2
3 M KOH/0.1 M ZnO	-1362 ± 6
7 M KOH/0.1 M ZnO	-1383 ± 3
10 M KOH/0.1 M ZnO	-1390 ± 8

REACTION ORDERS IN HYDROXYL IONS. In this case too, the reaction orders cannot be measured. The i_o was virtually pH independent:

$$\left(\frac{\partial \log i_o}{\partial \log a_{KOH}}\right) = -0.1 \text{ to } +0.1.$$ The reaction orders in the hydroxyl ion can be calculated according to the equations (5.4) and (5.5). The resulting values for the anodic and cathodic p_{OH^-} are summarized in Table 5.9.

Table 5.9   calculated reaction order p_{OH^-} for the anodic and cathodic process at the amalgamated zinc electrodes as function of KOH concentration.

Electrolyte	$p_{OH^-, anodic}$	$p_{OH^-, cathodic}$
1.5 M KOH/0.1 M ZnO	2.5 ± 0.8	-0.7 ± 0.3
3 M KOH/0.1 M ZnO	2.5 ± 0.7	-1.0 ± 0.4
7 M KOH/0.1 M ZnO	2.9 ± 0.7	-1.4 ± 0.6
10 M KOH/0.1 M ZnO	2.7 ± 0.7	-1.6 ± 0.4

REACTION ORDERS IN ZINCATE. Since the cathodic Tafel slope is a function of the KOH concentration, the p in zincate was measured both in 3 M and 10 M KOH in the same way as done for the zinc electrode. Both experiments gave a value of +0.9 for the cathodic p. In the anodic direction this value was 0.

EXPERIMENTS AT CONSTANT IONIC STRENGTH. In contrast to the results for zinc, the ionic strength had a distinct influence on the kinetics of the amalgamated electrode. The anodic Tafel slope remained the same, but the cathodic slope was 50 - 59 mV for the whole KOH concentration region. The i_o was pH independent.

5.5. Discussion/conclusions.

The results can be summarized as follows: (Table 5.10).
The interpretation of the results for the zinc electrode is rather straightforward. The results are in reasonable agreement with the mechanism suggested by Bockris et al. for KOH concentrations up to 3 M,

Table 5.10 Results of the kinetic experiments for the zinc electrode and the amalgamated electrodes (values in brackets give the standard deviation σ_g)

M KOH	Anodic				Cathodic			
	1.5	3	7	10	1.5	3	7	10
Zinc electrode:								
Tafelslope b(mV)	47(6)	41(12)	53(16)	38(11)	105(19)	130(27)	137(32)	137(32)
$i_o \cdot 10^4$ (A cm^{-2})	84(61)	140(95)	77(60)	84(45)	155(61)	450(330)	400(320)	380(240)
p_{OH^-}	1.9±0.3	2.1±1.0	1.7±0.8	2.3±1.0	-0.8±0.3	-0.7±0.3	-0.6±0.3	-0.6±0.3
$p_{Zn(OH)_4^{2-}}$	-	-	0±0.1	-	-	-	1.3±0.3	-
Effect of Ionstrength	no	no	no	-	no	no	no	-
Amalgamated electrodes:								
Tafelslope b(mV)	35(8)	35(9)	30(5)	33(6)	122(26)	87(17)	63(18)	53(7)
i_o 10^4 (A cm^{-2})	100(30)	130(80)	160(70)	150(60)	180(90)	260(130)	220(110)	190(50)
p_{OH^-}	2.5±0.8	2.5±0.7	2.9±0.7	2.7±0.7	-0.7±0.3	-1.0±0.4	-1.4±0.6	-1.6±0.4
$p_{Zn(OH)_4^{2-}}$	-	0	-	0	-	0.9±0.2	-	0.9±0.2
Effect of Ionstrength	no	no	no	-	yes	yes	yes	-

and hence in conflict with the mechanism of Dirkse and Hampson. Tafel slopes of about 40 mV in anodic and about 120 mV in cathodic direction, indicate the following reaction as RDS, in both anodic and cathodic direction.

$$Zn(OH)_3^- + e^- \rightarrow Zn(OH)_2^- + OH^-$$
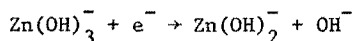
For this mechanism the following reaction orders would be expected:

	anodic	cathodic
p_{OH^-}	3	-1
$p_{Zn(OH)_4^{2-}}$	0	1

The experimental p-values in zincate are in agreement with these data. The values for p_{OH^-} are somewhat less ($p_{OH^-,anodic} \simeq 2.0$ and $p_{OH^-,cathodic} \simeq -0.7$). This is attributed to the intricate way of calculation of p_{OH^-}, which involves both experimental and literature data. Since the electroactive species is $Zn(OH)_4^{2-}$, the first two steps in the cathodic direction are

$$Zn(OH)_4^{2-} \rightarrow Zn(OH)_3^- + OH^-$$

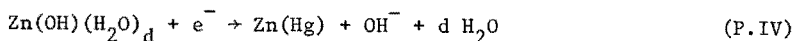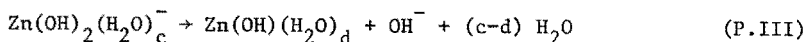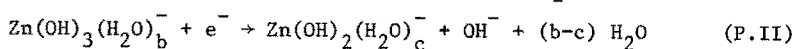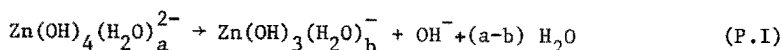$$Zn(OH)_3^- + e^- \rightarrow Zn(OH)_2^- + OH^-$$
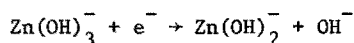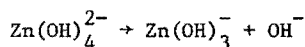
The remaining steps of the mechanism of Bockris et al. are based on theoretical arguments.

Although i_o cannot be determined exactly from our experiments at low overpotentials, one may conclude that the value for i_o from these experiments, and from experiments at high overpotential (Tafel region) did not differ by more than a factor 3. This is in agreement with the findings of Bockris et al., who concluded from this information that kink site formation is not rate limiting. Unfortunately, direct measurement of the reaction orders in OH^- is not possible. It has become clear in our experiments that i_o is virtually pH independent. This is again in agreement with the findings of Bockris et al. and contradicts measurements of Dirkse, who obtained a maximum at 7 M KOH [8].

The same applies to the measurement of the reaction orders in zincate, Fig. 5.5, which reveals that i_o depends on the zincate concentration. Dirkse and Hampson, however, observed that i_o was practically independent of the zincate concentration [8,11].

The differences in the i_o values from our work and that of others must be attributed to differences in electrode pretreatment and to the measuring period. The highest values for i_o were obtained when short measuring periods (μs range) were used. Bockris et al. reported values of $(80-3700) . 10^{-4}$ A cm^{-2} in electrolytes from 0.1 - 3 M KOH. The fact that Dirkse et al. did not obtain straight Tafel lines at high overpotentials [12] is probably caused by the fact that the ohmic potential drop was not taken into account. Our experiments showed that the IR-drop certainly cannot be neglected. The ionic strength has no influence on the mechanism and the kinetics of the zinc electrode.

The explanation of results for the amalgamated electrode is not equally straightforward. The formation of kink sites is of no importance since i_o values measured in experiments at low and very high overpotentials are the same. The results at a constant ionic strength suggest that water participates as a reaction partner. On the basis of this assumption, and the obtained Tafel slopes, we propose the following mechanism in which the reacting species, adsorbed at the electrode, is the water-containing species $Zn(OH)_4(H_2O)_a^{2-}$:

$$Zn(OH)_4(H_2O)_a^{2-} \rightarrow Zn(OH)_3(H_2O)_b^- + OH^- + (a-b)\ H_2O \qquad (P.I)$$

$$Zn(OH)_3(H_2O)_b^- + e^- \rightarrow Zn(OH)_2(H_2O)_c^- + OH^- + (b-c)\ H_2O \qquad (P.II)$$

$$Zn(OH)_2(H_2O)_c^- \rightarrow Zn(OH)(H_2O)_d + OH^- + (c-d)\ H_2O \qquad (P.III)$$

$$Zn(OH)(H_2O)_d + e^- \rightarrow Zn(Hg) + OH^- + d\ H_2O \qquad (P.IV)$$

The rate determining step in the anodic and cathodic direction is probably
not the same because of the values of the anodic and cathodic Tafel
slopes. The anodic Tafel slope of 30 - 35 mV indicates that in anodic
direction reaction (P.I) is rate determining (independent of the ionic
strength). The shift in the cathodic Tafel slope from 120 to about 60 mV,
when going to high KOH concentrations, can be explained if (c-d) is
smaller than (b-c). At high KOH concentrations, there is almost no free
water present, so reaction (P.III) will proceed faster than reaction
(P.II); consequently, the Tafel slope changes from 120 to 60 mV. At a
constant ionic strength of 10 M there is no free water available in
each solution, thus reaction (P.III) will be the RDS over the whole
concentration range. The question arises what causes the different
behaviour of the zinc and the amalgamated zinc electrode, since the
ionic strength does not have any influence on the behaviour of the zinc
electrode. In our view, this change is caused by a difference in adsorption
because the double layer capacities differ a factor ten. The high double
layer capacity of the zinc electrode suggests that the electrode is
covered with adsorbed OH^--ions and/or intermediates. The capacity of
the amalgamated electrode approaches the value for pure mercury. This
implies that the surface of this electrode is mainly covered with
adsorbed water molecules. Consequently, the water activity only influ-
ences the amalgamated electrode, and at the zinc electrode only OH^-
is involved. Thus, the difference in the mechanism of the zinc electrode
and the amalgamated electrode is caused by a change in adsorption beha-
viour, rather than by easier formation of kink sites due to the amal-
gamation.

5.6. Literature

1. J.J. Lander and J.A. Keralla, Technical Report on Contract
   AF 33(657)8943, Delco-Remy Divisions, General Motors Corp.,
   Anderson, Indiana (1963).

2. O. Wagner and A. Himy, Proc. 27th Power Sources Conf., PSC Publications Committee, Red Bank, N.J., 1976, p. 135.

3. G.A. Dalin, Zinc-Silveroxide Batteries. Edited by A. Fleischer and J.J. Lander, Wiley, New York (1971) pp. 87-95.

4. J. McBreen, J. Electrochem. Soc. 119 (1972) 1620.

5. J.P.G. Farr, N.A. Hampson, J. Electroanal. Chem. 13 (1967) 443.

6. N.A. Hampson, G.A. Herdman, R. Taylor, J. Electroanal. Chem. 25 (1970) 9.

7. T.P. Dirkse, N.A. Hampson, Electrochim. Acta 17 (1972) 135.

8. T.P. Dirkse, N.A. Hampson, Electrochim. Acta 17 (1972) 383.

9. T.P. Dirkse, N.A. Hampson, Electrochim. Acta 17 (1972) 1113.

10. T.P. Dirkse, J. Electrochem. Soc. 125 (1978) 1591.

11. T.P. Dirkse, J. Electrochem. Soc. 126 (1979) 541.

12. T.P. Dirkse, J. Electrochem. Soc. 127 (1980) 1452.

13. T.P. Dirkse, J. Electrochem. Soc. 126 (1979) 1456.

14. J.O'M. Bockris, Z. Nagy, A. Damjanovic, J. Electrochem. Soc. 119 (1972) 285.

15. V.S. Muralidharan, K.S. Rajagopalan, J. Electroanal. Chem. 94 (1978) 21.

16. T.P. Dirkse, D. de Wit, R. Shoemaker, J. Electrochem. Soc. 115 (1968) 442.

17. D.A. Payne, A.J. Bard, J. Electrochem. Soc. 119 (1972) 1665.

18. A.R. Despić, Dj. Jovanovic, T. Rakic, Electrochim. Acta 21 (1976) 63.

19. Belgian Patent No. 819.926 (1974).

20. U.S. Patent No. 4.104.188 (1974).

21. J. Swift, F.L. Tye, A.M. Warwick, J.T. Williams, Amalgamation of zinc anodes in Leclanché dry cells, Power Sources 4, Ed. D.H. Collins, Oriel Press, Newcastle upon Tyne (1973).

22. J.O'M. Bockris, H. Wroblowa, E. Gileadi, B.J. Piersma, Trans. Faraday. Soc. 61 (1965) 2531.

23. D.J. Kooyman, J.H. Sluyters, J. Electroanal. Chem. 13 (1967) 152.

24. I.H. Plonski, J. Electrochem. Soc. 116 (1969) 944.

25. P. Selånger, Electrochim. Acta 21 (1976) 637.

26. D.P. Boden, R.B. Wylie, V.J. Spera, J. Electrochem. Soc. 118 (1971) 1298.

27. G.C. Akerlof, P. Bender, J. Am. Chem. Soc. 70 (1948) 2366.

28. R.A. Robinson, R.H. Stokes, Electrolyte Solutions, second edition Butterworths, London (1959).

6. THE ZINC ELECTRODE IN THE NICKEL OXIDE-ZINC ACCUMULATOR

6.1. Introduction.

In this chapter the behaviour of the zinc electrode in a nickel oxide-zinc
battery will be investigated in order to get more insight in the processes
occuring at the zinc electrode, in particular in the Shape Change (SC)
phenomenon. This study was carried out with self-built cells, subjected to
repeated charge/discharge cycles. The occurrence of SC is strongly in-
fluenced by the cell-geometry. Cells of about 0.5 Ah capacity, with porous
zinc electrodes and built-in facilities to measure the potential distri-
bution along the zinc surface, were used.
Because of the reported influence of amalgamation on the Shape Change
[1-3], the effect of incorporation of metal oxide additives (HgO, PbO)
and of replacing zinc oxide partially by amalgamated zinc powder, was
studied.

6.2. Construction of electrodes and cell-design

Zinc electrode

The following zinc electrodes were used:

I.   teflon-bonded zinc oxide

II.   teflon-bonded zinc oxide with additive (2 wt% HgO or 2 wt% PbO)

III. teflon-bonded zinc oxide (with 1-6 wt% HgO as an additive), 1 part,
     and amalgamated zinc powder (with 1,3 or 6 wt% Hg), 2 parts, the
     latter as furnished by Metallurgy Hoboken-Overpelt, Belgium.

The teflon bonded zinc oxide was prepared following the procedure given by
McBreen [4]: a 2 ml portion of teflon dispersion (30-N, DuPont) was
diluted with 15 ml doubly distilled water and added to 25 g zinc oxide
(Merck p.a.). The paste was then heated to 280-300°C, cured at that temper-
ature for about 1 hr. and then crushed. The teflon-bonded zinc oxide was
mixed thoroughly with HgO or PbO as an additive for preparing the type II-
electrode, or with HgO and amalgamated zinc powder for preparing the type
III-electrode. The electrodes themselves were prepared by pressing the
mixture in a mould onto a nickel screen (which has been plated beforehand
with silver and acted as a current collector; geometric surface area of
3.5 x 3.9 cm). The current lead of silver was connected to the screen by
spotwelding. In table 6.1 the composition of the different zinc electrodes
is tabulated.

Table 6.1 Composition of the zinc electrodes and assembling type of cells

Cell no.	Teflon bonded zinc oxide (g)	Additive		Amalgamated Zinc powder		thickness (cm 10^3)	kind of zinc electr.	Assembling type
		kind	(g)	(g)	% Hg			
1	2.0	–	–	–	–	64±3	I	A
2	2.0	PbO	0.04	–	–	65±10	II	A
3	2.0	HgO	0.04	–	–	65±7	II	A
4	1.0	HgO	0.01	2	1	69±9	III	A
5	1.0	HgO	0.03	2	3	67±10	III	A
6	1.0	HgO	0.06	2	6	67±9	III	A
7	2.0	HgO	0.04	–	–	62±8	II	B
8	1.5	HgO	0.03	–	–	52±2	II	B
9	1.5	–	–	–	–	53±3	I	B
10	1.5	–	–	–	–	–	I	B
11	2.0	–	–	–	–	69±5	I	A
12	2.0	–	–	–	–	66±8	I	A
13	2.0	–	–	–	–	65±5	I	A
14	2.0	–	–	–	–	66±5	I	A

Nickel oxide electrode

Sintered nickel oxide electrodes were taken from bought Ni-Cd batteries, Varta type SD 2.4. Each electrode (3.5 x 3.9 x 0.085 cm) had a capacity of 0.4 Ah. In cells 1-9, the nickel oxide electrodes were uncharged and in cells 10-13 charged (about 0.3 Ah).

Separator system

The separator was a 0.009 cm thick RAI P-2193 specimen, consisting of one layer of cellophane, sandwiched between two layers of RAI P-2291, a copolymer of methacrylic acid and cross-linked low-density polyethylene.

Electrolyte

The electrolyte is 9.5 M KOH/0.5 M ZnO/0.5 M LiOH and prepared from Analar chemicals and doubly distilled water.

Reference electrode

The reference electrode is a Hg/HgO-electrode in a glass tubing, see Fig. 6.1.

Cell specifications and assembly

The electrochemical experiments are carried out in cells of acrylic plastic with interior dimensions of 6 x 3.7 x 0.4 cm (= h x 1 x w).

70

Provisions were made for introduction of one or more reference electrode(s)
by drilling holes (diameter: 0.6 cm) in the
wall. The connection between the reference
electrode compartment and the interior was a
drilled hole (diameter: 0.1 cm), filled with
adsorber material to prevent entering bubbles.
In Fig. 6.1 a schematic view of the cell with
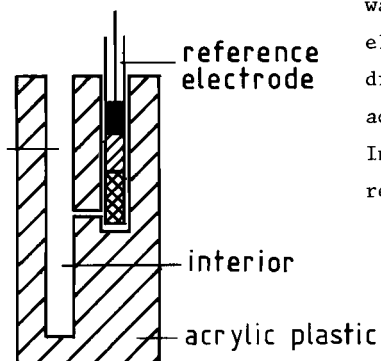reference electrode is given.

reference
electrode

interior

acrylic plastic   Fig. 6.1 Scheme of cell with
                            reference electrode.

The cells were assembled in two different ways:

type A The zinc electrode is placed in between the two nickel oxide elec-
        trodes (cells no. 1-6 and 11-13, Table 6.1). In this configuration
        only one reference electrode is used, which is placed at the side
        of the cell. The relative position of the capillary hole in the
        side wall, with respect to the zinc electrode, is shown in Fig.
        6.2.A.

type B The zinc electrode is placed in between the front cell wall and the
        nickel oxide electrode (consisting of two parallel plates) (cell
        no. 7-10 Table 6.1). One reference electrode is mounted at the side
        of the electrodes (a), three other reference electrodes are placed
        along the front of the zinc electrode as indicated in Fig. 6.2.B,
        nrs. b, c and d.

zinc-electrode   d

nickeloxide
electrode   zinc electrode

capillary hole a

                                                   c

(A)   (B)   capillary hole
                                                   b
      side   front
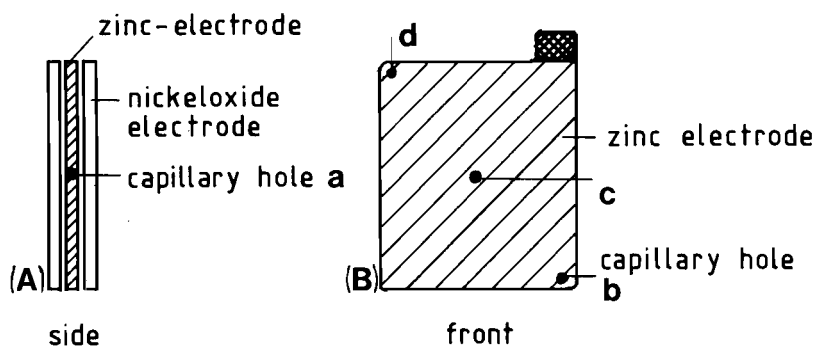
Fig. 6.2A/B Relative position of the capillary holes with respect to
             the zinc electrode for the types A and B, respectively.

71

The RAI P-2193 separator was wrapped three times around the zinc electrode
(in such a way that short circuiting was almost impossible).

Furthermore, a nonwoven propylene adsorber (RAI A-1480) was placed in
abuttal of the nickel oxide electrode

The cell was filled such that the level of the electrolye was about 0.3 cm
above the top of the electrodes (i.e. about 3 ml electrolyte was used).
The electrodes were allowed to soak for about one day prior to the start
of the experiment. Thereafter, the cell was vacuum treated to remove gas
bubbles. (The cells were operated in the vented mode.)

6.3. Experimental Procedure.

6.3.1 Cycling experiments.

The batteries no. 1-10 (Table 6.1) were subjected to charge-discharge cycles
at constant current, 200 mA for cells 1-6 (assembly type A) and 100 mA for
cells 7-10 (assembly type B).

Since zinc is utilized at two sides for cells 1-6 and only at one side for
cells 7-10, this implies the same current densities, i.e. 7.3 mA cm^{-2}.

An automatic cycling device was constructed for these experiments which was
capable of repeated charging and discharging three test cells to preselected
cut-off times and/or voltages. The rest time between the cycles is usually
circa 30 min. This device was used in conjunction with a power supply (Delta
power supply E 030-1).

The cell voltage (E_{cell}) and the potential of the zinc electrode with res-
pect to the Hg/HgO reference electrodes ($E_{Zn,a} \ldots E_{Zn,d}$) were monitored
using high impedance converters ($10^{13}\Omega$ between the recorder and the reference
electrodes).

The zinc electrodes were charged with 0.5 Ah (cells 1-6) and 0.3 Ah (cells
7-10), which is 20-40% of the theoretical capacity of the zinc active
material, as is usual in zinc battery charging [5,6]. Less charge passed
through the cell, if the cell voltage reached the charging cut-off volt-
age of about 2.2 V beyond which hydrogen is formed. Here, the state-of-
charge (SOC) is defined as being 100% with this predetermined amount of
charge or if the cut-off voltage is reached.

The cells were discharged until the cell voltage reached the discharging cut-
off voltage of about 1.35 V corresponding with a sudden decline in the volt-
age time curve. This state is defined here as the fully discharged state
(0% SOC).

72

After cycling experiments, the tested cells were dismantled and the zinc electrode was examined for Shape Change, visually, and by measuring the thickness at different places of the electrode.

6.3.2 Capacity measurements.

The capacity of the cell is measured as a function of the discharge current to get insight in the degree of utilization of the zinc electrode. The charge current was 70 mA (2.6 mA cm^{-2}) (charge time: 8 hr) and the discharge current was varied between 70 and 500 mA (2.6-18.3 mA cm^{-2}). A cut-off voltage of 1.35 V was used for all discharge measurements. After discharge at currents higher than 70 mA the rest capacity was determined by discharging the cell with 70 mA, in order to get comparable conditions for each charge/discharge cycle.

6.3.3 Porosity of the zinc electrode

The mercury penetration method was used to measure the pore volume per gram, V_p [cm^3 g^{-1}], and the pore size distribution of electrodes, fabricated of teflon bonded zinc oxide and of a mix of teflon bonded zinc oxide and amalgamated zinc powder.
(These experiments were carried out by the group of Prof. Scholten at the department of Chemical Technology, University of Technology, Delft). The porosity is then calculated with

$$\varepsilon = \frac{V_p}{\rho^{-1} + V_p} \qquad\qquad (6.1)$$

in which ρ = true density of active material [g cm^{-3}].
The porosity can also be calculated with

$$\varepsilon = \frac{V_p}{V_t} \qquad\qquad (6.2)$$

in which V_t = total volume per gram material [cm^3 g^{-1}].
The total volume (=V_t) is determined by the geometric surface area and the thickness, for which the average value is taken from thickness measurements at different places along the electrode surface.

6.4 Results.

6.4.1 Cycling experiments.

In Fig. 6.3 cell voltage (E_{cell})- and zinc potential ($E_{Zn,a}$)-time curves during charging and discharging for cell 1 at constant current of 200 mA are shown for different cycle numbers. During the first 35 cycles the cell can be charged with the predetermined amount of 0.5 Ah, but with increasing cycle number the cut-off voltage (2.2 V) is reached earlier, so less charge is accepted by the cell. The zinc potential curves show a similar pattern as the cell voltage curves.
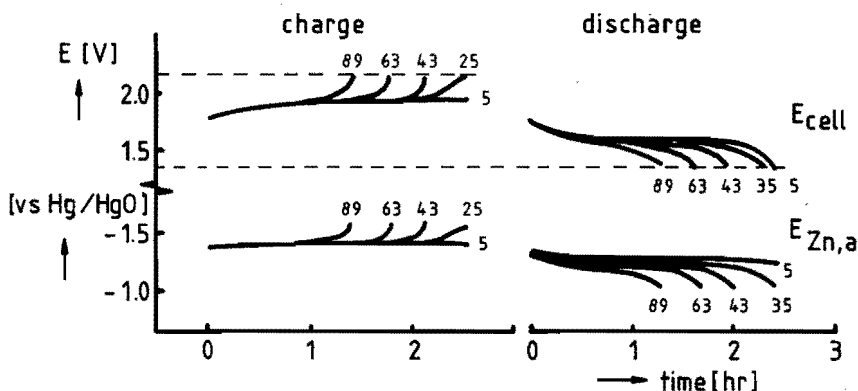
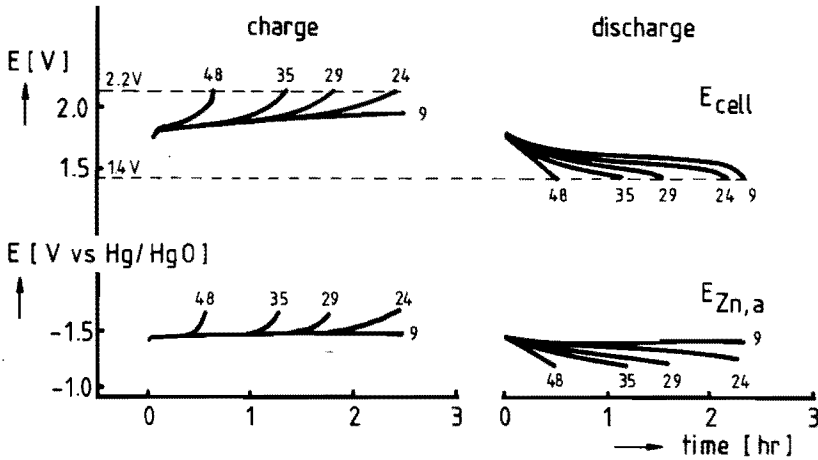Fig. 6.3 E_{cell} and $E_{Zn,a}$-time curves during charging and discharging of cell 1 at constant current of 200 mA for different cycle numbers.
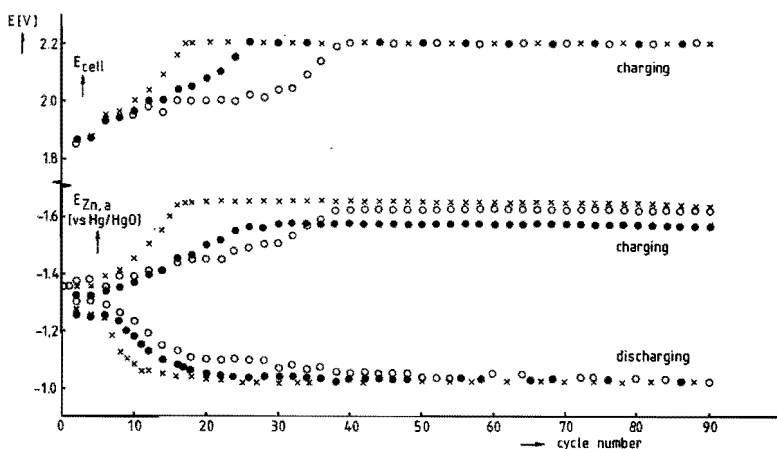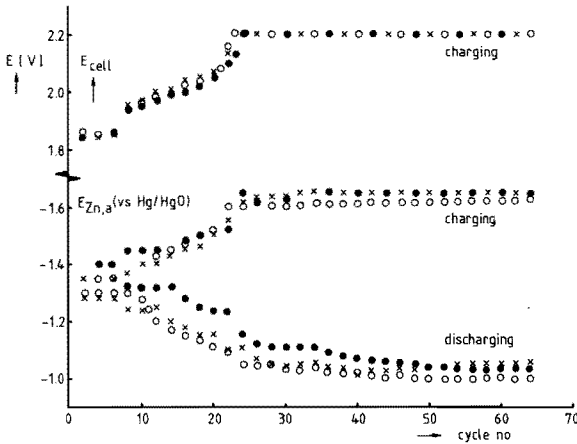

Fig. 6.4 E_{cell} and $E_{Zn,a}$ of cells 1-3 at the end of the charge and discharge period as function of cycle number.

o = cell 1 ; ● = cell 2 ; x = cell 3.

During discharge $E_{Zn,a}$ remains constant for the first 5 cycles. On further cycling, a decrease of $E_{Zn,a}$ is observed at the end of discharge: after about 40 cycles a limit of ca. 1.05 V (vs. Hg/HgO) is reached at the 1.35 V cell cut-off voltage. Fig. 6.4 compares E_{cell} and $E_{Zn,a}$ at the end of the charge and discharge periods during cycling for cell 1 (no additive), cell 2 (PbO additive) and cell 3 (HgO additive) (See Table 6.1.).

The cut-off voltage during charging is reached after 18 cycles in cell 3, after 26 in cell 2 and after 40 cycles in cell 1. This pattern is also observed for $E_{Zn,a}$, which reaches a limit value of about 1.6 V(vs. Hg/HgO) at the 2.2 V cell cut-off voltage. During discharging $E_{Zn,a}$ levels off to ca. 1.05 V (vs. Hg/HgO), reached by cell 3 after about 15, by cell 2 after about 20, and by cell 1 after about 40 cycles.
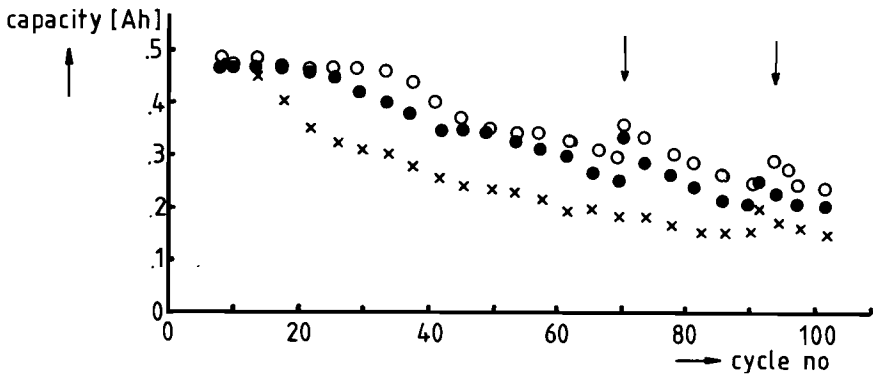
Fig. 6.5   Capacity of the cells 1-3 as ·function of cycle number.
           o = cell 1 ; ● = cell 2 ; x = cell 3.
           arrows = rest period (64 hours)

The charge efficiency, defines as the ratio of the charge output and the charge input, is about 95% for cell 3 and about 90% for cells 1 and 2. The capacity (= charge output) of the three cells is plotted in Fig. 6.5. Initially, the capacities of the cells are constant, but with cycling the capacity decreases. However, a rest period (64 hours) after 70 and 92 cycles, had a benificial effect on the capacity of cell 1 and 2. Photographs of the zinc electrode from cell 2 after 104 cycles are shown in Fig. 6.6; in Fig. 6.7 the thickness distributions of the zinc electrodes of cells 1-3, measured at different places along the surface is given. The amount of material is largest in the center and at the bottom, showing unambiguously the Shape Change phenomenon. No significant differences between the three cells are observed. At the edges some active material is still present in a
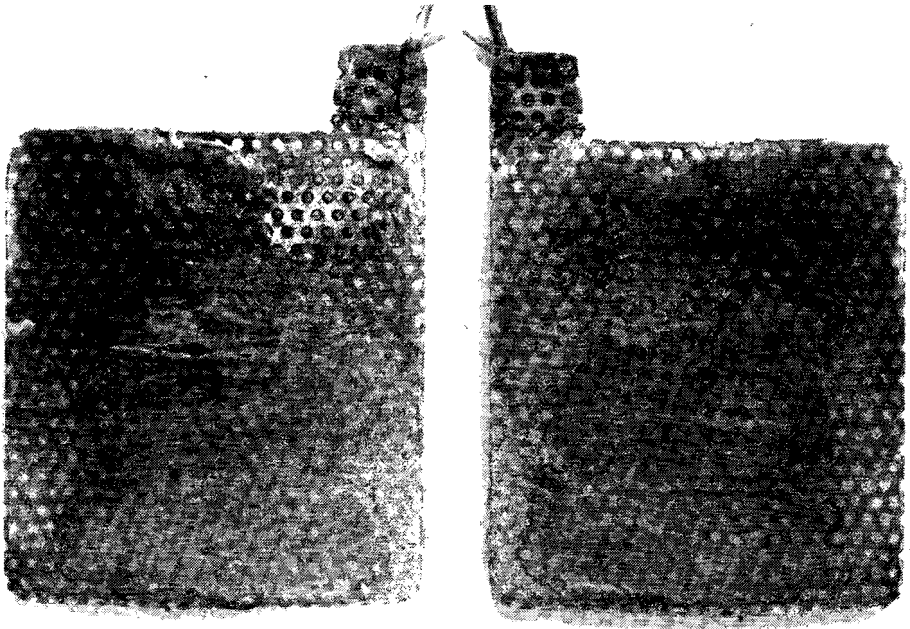
Fig. 6.6   Photographs of the zinc electrode (both sides) of cell 2 after
           104 cycles.

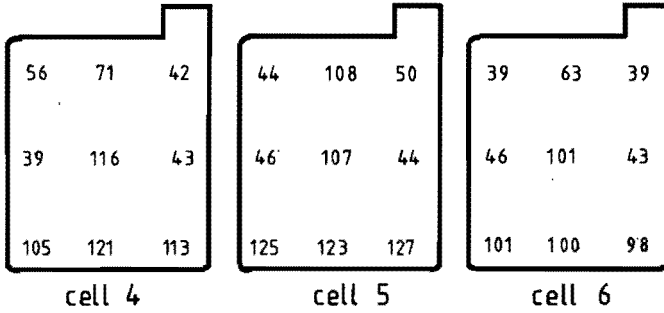cell 1   cell 2   cell 3
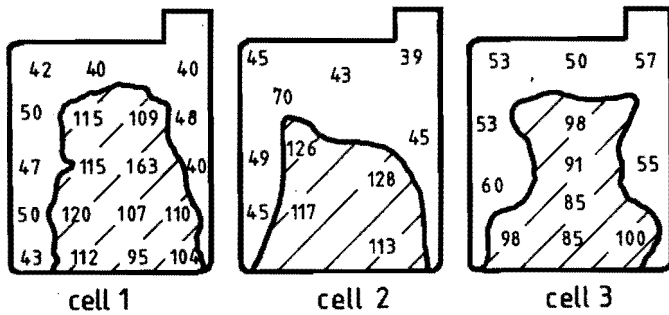
Fig. 6.7   Thickness distributions (in 10^3 cm) of the zinc electrodes of
           cells 1-3 after 104 cycles as measured at different places along
           the surface.

layer, which seems to be more teflonated than the material in the center
and at the bottom.

Cycling results for cell 5, in which the zinc oxide is partially replaced
by amalgamated zinc powder, are presented in Fig. 6.8. The bend in the

Fig. 6.8 E_{cell} and $E_{Zn,a}$-time curves during charging and discharging of
cell 5 at constant current of 200 mA for different cycle numbers.

curves develops more gradually than that in Fig. 6.3, both during charging
and discharging. Fig. 6.9 shows E_{cell} and $E_{Zn,a}$ at the end of the charge
and discharge period for cell 4 (prepared with 1% amalgamated zinc), cell 5
(3% amalgamated zinc) and cell 6 (6% amalgamated zinc). The cut-off volt-
age on charging is reached after about 24 cycles for all three cells. The
charge efficiency is high (95%) for the majority of the cycles.

Fig. 6.9 E_{cell} and $E_{Zn,a}$ of cells 4-6 at the end of charge and discharge
period as function of cycle number.
o = cell 4 (1% amalg. Zn) ; ● = cell 5 (3% amalg. Zn) ;
x = cell 6 (6% amalg. Zn).

In Fig. 6.10 the capacity (= charge output) of these cells is plotted as a function of cycle number. The decrease, after an initially constant value, is much steeper than in cells 1-3 (Fig. 6.5). Already after 25-35 cycles the capacities are reduced to 50% of the initial values. No significant differences between the three cells with the different percentage of mercury were found.
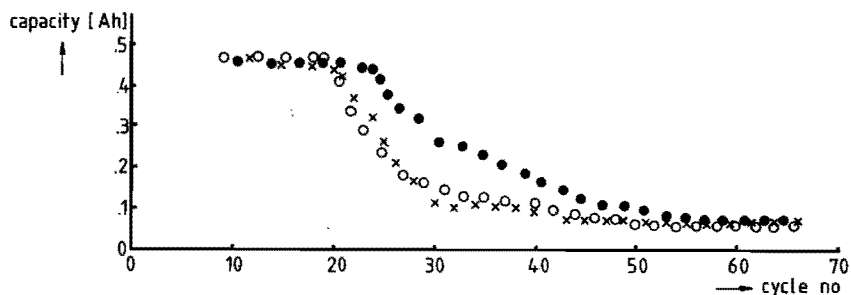
Fig. 6.10   Capacity of the cells 4-6 as function of cycle number.
o = cell 4 ; • = cell 5 ; x = cell 6.

In Fig. 6.11 photographs of the zinc electrode of cell 6, after 67 cycles are shown, which is also representative for cells 4-5; in Fig. 6.12 the thickness distributions of the zinc electrodes of cells 4-6 are given.
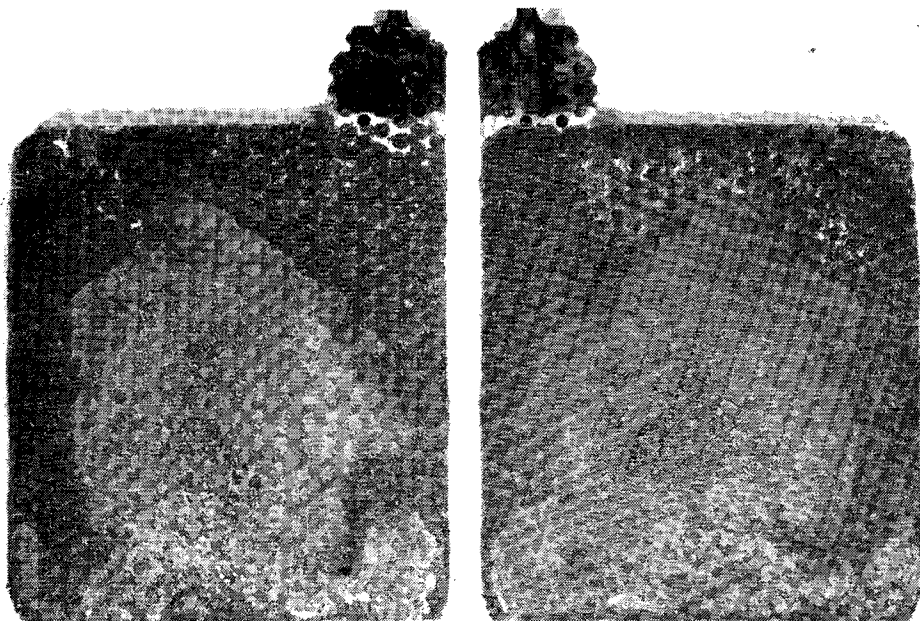
Fig. 6.11   Photographs of the zinc electrode (both sides) of cell 6 after 67 cycles.

78

56	71	42
39	116	43
105	121	113

cell 4

44	108	50
46	107	44
125	123	127

cell 5

39	63	39
46	101	43
101	100	98

cell 6

Fig. 6.12 Thickness distributions (in 10^3 cm) of the zinc electrodes of
cells 4-6 after 67 cycles as measured at different places
along the surface.

6.4.2 Potential distribution.

The potential distribution over the surface of the zinc electrode was mea-
sured in the cells 7-9, using four reference electrodes, as indicated in
Fig. 6.2, $(E_{Zn,a}, \ldots E_{Zn,d})$.
Potential times curves of cell 7 with 2% HgO additive, are shown in Fig.
6.13A, for different cycle numbers together with the cell voltage-time
curves Fig. 6.13B. In Fig. 6.14 the potentials at the end of the charge and
discharge period are plotted as a function of the cycle number. $E_{Zn,a}$, $E_{Zn,b}$
and $E_{Zn,d}$ increase more gradually to a maximum value (about 1.8 V) than
$E_{Zn,c}$ (midst of plate), which rather suddenly increases to that value
between cycle 52-55.
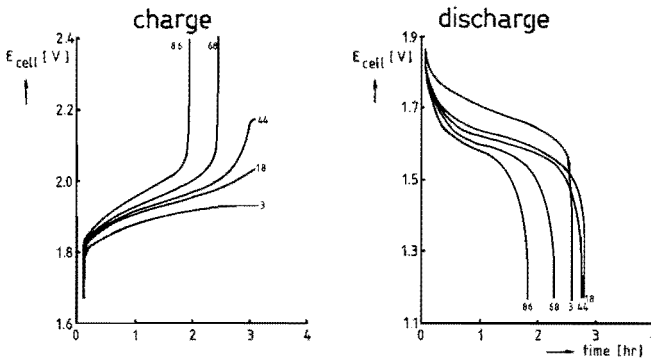
Fig. 6.13A E_{cell}-time curves during charging and discharging of cell 7
at constant current of 100 mA for different cycle numbers.

79
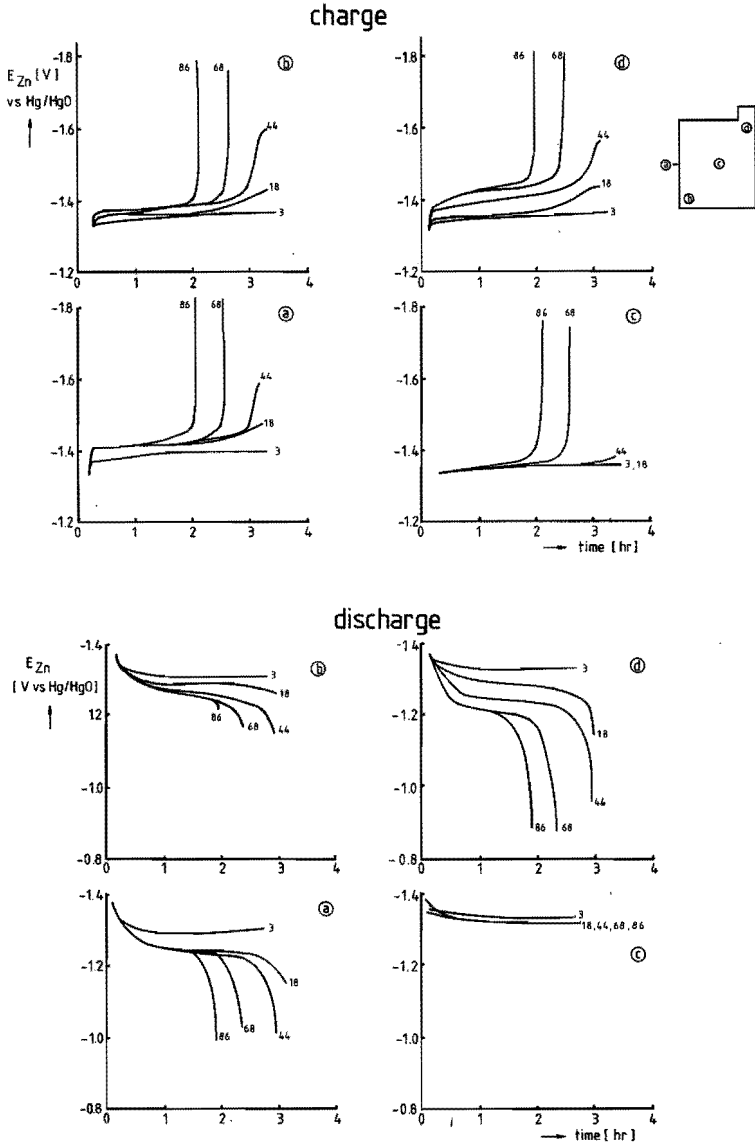
charge

discharge

Fig. 6.13B $E_{Zn,a}$ .... $E_{Zn,d}$-time curves during charging and discharging of cell 7 at constant current of 100 mA for different cycle numbers.

During discharging, differences between the potentials become more clear and different leveling-off values are reached. The capacity (initially constant) begins to decrease in the same cycle number (52-55), where $E_{Zn,c}$ strongly increases.
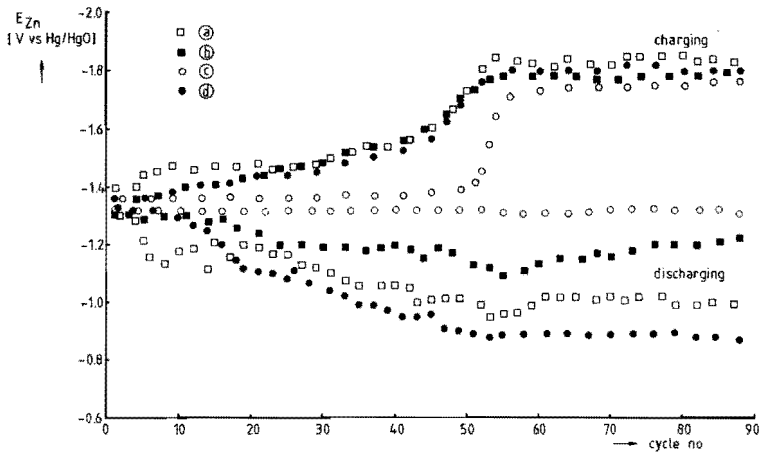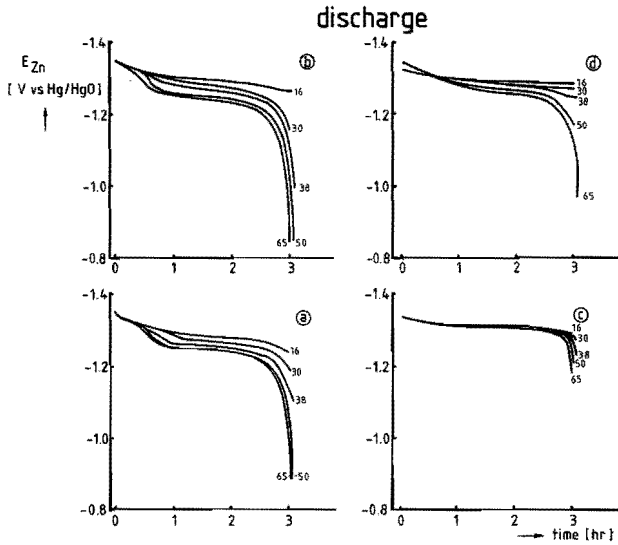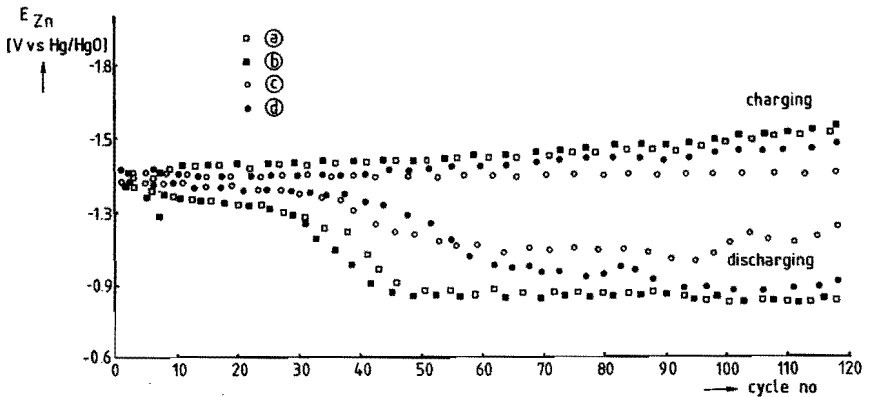
Fig. 6.14 $E_{Zn,a}$ .... $E_{Zn,d}$ of cell 7 at the end of the charge and discharge period as function of cycle number.

In cell 8 (also with 2% HgO additive) the amount of active material of the zinc electrode is reduced to 1.5 gr. The cycle number where $E_{Zn,c}$ strongly increases and the capacity begins to decline, is now in the region 40-43. Potential-time curves at discharging of cell 9 (without the HgO additive), are shown in Fig. 6.15. The increase with cycling of the potentials at the end of the charge period is much more gradual (Fig. 6.16). The potential
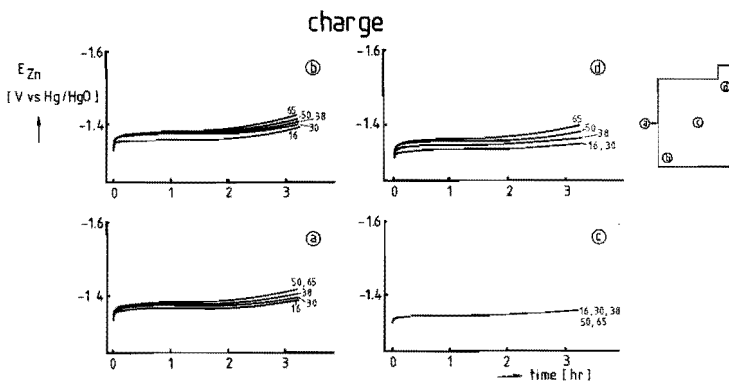
Fig. 6.15 A $E_{Zn,a}$ .... $E_{Zn,d}$-time curves during charging of cell 9 at constant current of 100 mA for different cycle numbers.

discharge

Fig. 6.15 B $E_{Zn,a}$ .... $E_{Zn,d}$-time curves during discharging of cell 9
at constant current of 100 mA for different cycle numbers.

Fig. 6.16 $E_{Zn,a}$ .... $E_{Zn,d}$ of cell 9 at the end of the charge and dis-
charging period as function of cycle number.

distribution upon discharging is more uniform than in cell 7 and the highest
overpotential is measured at the bottom edge ($E_{Zn,b}$), contrary to cells 7
and 8, where the highest overpotential is measured at the top-edge ($E_{Zn,d}$).

6.4.3 Influence of the nickel oxide electrode.

One experiment has been carried out to establish the influence of the state-of-charge of the nickel oxide electrode in the beginning of cycling. In Fig. 6.17 potential-time curves for the zinc electrode of cell 9 with an initi-ally uncharged, and of cell 10 with an initially charged nickel oxide elec-trode, are shown during discharging of cycle 9. The anodic overpotential of zinc in cell 10 increased strongly at the end of discharge, indicating that the zinc electrode is the capacity limiting in cell 9, because no increase is observed.
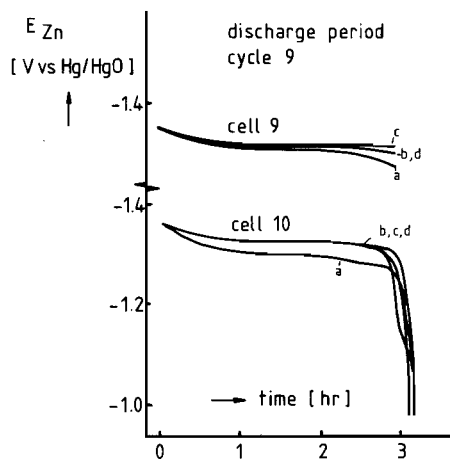
Fig. 6.17

$E_{Zn,a}$ .... $E_{Zn,d}$ of cell 9 and 10 during discharging in the 9th cycle.

6.4.4 Capacity

The capacity was determined for three cells with zinc oxide electrodes con-taining no additives (cells 11-13, see Table 6.1). Charged nickel oxide electrodes were used.

In Fig. 6.18 the results of three series of experiments are shown. The capa-city tends to decrease linearly with the discharge current.
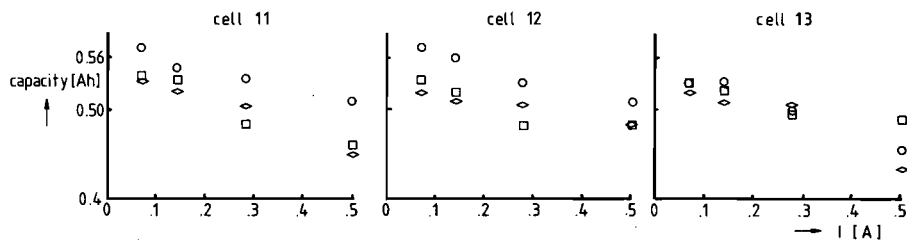
Fig. 6.18 Capacity of the cells (11-13) as a function of the discharge current for three series of experiments.

(o = 1st serie ; □ = 2nd serie ; ◇ = 3rd serie)

83

6.4.5. Porosity of zinc electrodes.

The porosity was determined for electrodes of the same composition as in
cell 1 and 4, i.e. a teflon bonded zinc oxide, respectively a mixture of
teflon bonded zinc oxide (1 part) and amalgamated zinc powder (2 parts). In
Fig. 6.19 the pore size distributions of these electrodes are shown. The
resulting data and the calculated porosities are tabulated in Table 6.2.
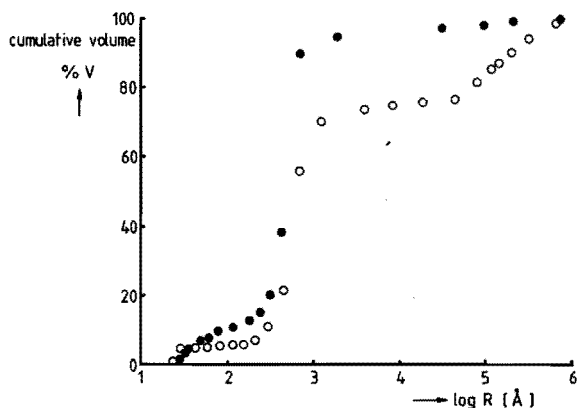The calculated porosities are rather low compared with literature values
(0.5-0.8) [7,8].

Fig. 6.19   Pore size distribution of the two kind of zinc electrodes.

      ● : teflon bonded zinc oxide

      o : teflon bonded zinc oxide and amalgamated zinc powder

Table 6.2   The pore volume per gram, mean pore radius, surface area, density, total volume
per gram and porosity of two different types of zinc electrode

	teflon bonded zinc oxide	teflon bonded zinc oxide and amalgam. zinc powder
Pore volume, V_p [$cm^3 \cdot g^{-1}$]	0.115	0.067
mean pore radius, R [Å]	260	320
surface area [$cm^2 \cdot g^{-1}$]	$8.4 \; 10^4$	$4 \; 10^4$
true density, ρ [$g \; cm^{-3}$]$^\square$	5.3	6.8
Total volume, V_t [$cm^3 g^{-1}$]	0.32	0.2
ε, with equation (6.1)	0.38	0.31
ε, with equation (6.2)	0.36	0.31

$^\square$calculated with $\rho_{ZnO} = 5.6 \; g \; cm^{-3}$; $\rho_{teflon} \simeq 2 \; g \; cm^{-3}$

$\rho_{Zn} = 7.1 \; g \; cm^{-3}$; $\rho_{Hg} = 13.6 \; g \; cm^{-3}$

6.5 Discussion.

While uncharged nickel oxide electrodes were used in cells 1-9, the charging curves indicate that, initially the cells can be loaded with the predetermined charge, hence the nickel oxide electrode is not capacity limiting; neither, initially is the zinc electrode. By observation and comparison of Figs. 6.4 and 6.9 with Figs. 6.5 and 6.10 respectively, it appears that E_{cell} and $|E_{Zn,a}|$, at the end of the charge period, increase with cycling and that the cut-off voltage and the maximum value of $E_{Zn,a}$ are reached at the same cycle which marks the start of the capacity decline of the cell. It follows from the charge efficiency data that in a cycle more zinc oxyde is reduced during charging than zinc is oxidized in the subsequent discharge. With each next cycle the amount of reducible zinc oxide decreases and finally it becomes exhausted, so that the zinc electrode cannot be charged further. This effect was calculated for the amalgamated zinc electrodes (cells 3-8), where the rate of self-discharge is low.

In Table 6.3 the total amount of the differences between charge input and charge output of all cycles up to the start of capacity decline is given in column 5; the last column 9 gives the sum (S) of column 5 and the charge input of the subsequent charge period (column 6). The theoretical capacities of the zinc oxide electrode (column 3) are in rather good agreement with the calculated sums (S). Therefore, it is concluded that the decrease of the capacity and the increase of the zinc overpotential during charging are caused by exhaustion of the active zinc oxide material.

Table 6.3 The theoretical capacity, the total amount of the differences between charge input and output up to the capacity decrease, and the charge input in the subsequent charge period for different cells.

(1)	(2)	(3)	(4)	(5)	(6)	(7)
cell no.	Amount of ZnO (g)	theoretical capacity (Ah)	cycles before capacity decrease	$\sum_{i=1}^{n}(Ah_{in}-Ah_{out})$ (Ah)	charge input subsequent charge period (Ah)	sum (S) (Ah)
3	2.0	1.3	18	0.67	0.43	1.10
4	1.0	0.65	23	0.32	0.32	0.64
5	1.0	0.65	24	0.22	0.45	0.67
6	1.0	0.65	22	0.22	0.42	0.64
7	2.0	1.3	54	1.10	0.45	1.55
8	1.5	1.0	43	0.84	0.30	1.14

In cells with non-amalgamated zinc electrodes considerable self-discharge
occurs with the result that more active zinc oxide material is present than
in amalgamated electrodes. This is demonstrated by the shift of the start
of capacity decline to a higher cycle number (Fig. 6.5), and also by the
more gradual increase of the cathodic zinc overpotentials (Fig. 6.16).
During discharging of cells 1-9 it can be deduced from Figs. 6.4, 6.9, 6.14
and 6.19, that in the beginning of cycling (1-10 cycles) the nickel oxide
electrode is the capacity limiting factor. With cycling, the zinc electrode
gradually becomes the limiting electrode, as can be seen from the increasing
anodic overpotential. Possible causes of this increase are:
- passivation of the zinc electrode by thin film formation [9,19];
- plugging of the pores of the electrode by insoluble reaction products
  [11];
- depletion of electrolyte [11].
A further point of interest is the much steeper decrease in capacity with
cycling of cells 4, 5 and 6 (Fig. 6.10) compared to cell 3 (Fig. 6.5). The
difference in porosity of the two types of zinc electrodes in thought to be
responsible for this effect: the porosity (ε) of the zinc electrodes in the
cells 4-6 is ca. 0.31, and ca. 0.37 in cell 3 (which in this respect can be
compared with the zinc electrode in cell 1), implying a smaller surface area
of the zinc electrode in cells 4-6 and hence a smaller degree of availibility
of the active material on discharging. So, the use of amalgamated zinc powder
for fabrication of the zinc electrode does not have a beneficial effect on
the cycling behaviour, though the rate of self-discharge seems to be lower
than with the other type of amalgamated zinc electrodes.

The capacity of the cell decreases linearly with the discharge current (Fig.
6.18), indicating that the availability of the active material decreases.
Probably, the above mentioned causes for the increase of the anodic over-
potential are also responsible for this decrease.

For a study of the Shape Change phenomenon it would be preferable to monitor
the current distribution which gives direct information about the material
distribution over the zinc electrode. However, it is not possible to carry
out current distribution measurements via sectioning of the zinc electrode:
the sections short-circuit as a result of dendrite formation during charging
(sectioning of the counter electrode would be possible but then it has to be
assumed that the current flow through a section of the counter electrode is
a good indication of the flow through the portion of the zinc electrode just
opposite that section). For our experiments we have therefore decided to

measure the potential distribution, because this is experimentally easy to do. In principle differences in overpotential over the surface of the zinc electrode can be attributed to:
- differences in local current density (as a result of the actual current distribution;
- variations in the zincate concentration at various points at the electrode;
- local passivation phenomena.

The current distribution is determined by many factors. With no polarization at the electrodes the primary current distribution is operative [12], which is determined by the geometry of the electrodes, the electrolyte and the separator. Due to activation and concentration polarization the actual current distribution will be more uniform. The magnitudes of the effects of these polarizations are dependent on the ratios of the kinetic respectively the mass transport resistance and the ohmic resistance.

If only the primary current distribution is operative then the current is highest at the periphery and no differences would be expected between charging and discharging. As result of polarization phenomena at the electrode, the actual current distribution varies continuously during charging and discharging and with cycling.

From the potential distribution measurements of cell 7 (with HgO-additive) and cel 9 (without additive) (Figs. 6.13 and 6.15), it can be seen that for both cells the potential distribution was more uniform during the charge than during the discharge period. The distribution of the end-potentials shows the same tendency (Figs. 6.14 and 6.16).

After dismantling of the cells, SC could be clearly observed in all cells. This is tentatively explained as follows. If it is assumed that places with higher overpotentials correspond to places with greater current densities, then it follows that in cells 7 and 9 the current density in the periphery is larger than in the centre and that the current distribution is more uniform during charging than discharging. Zincate is consumed in the charge period and produced in the discharge period. Therefore, the difference in current distribution will during discharging, result in a concentration gradient of zincate along the surface in the direction of the centre, which is more negative than the same gradient in the direction of the periphery during charging. Hence, a net movement of zincate to the centre is expected as result of one cycle. So the material redistribution, and thus the SC, can be explained by diffusion of zincate along the surface caused by non-uniform current distributions.

The concentration cell concept of McBreen [5] cannot explain the material redistribution, because the greater differences in anodic overpotentials compared to the cathode overpotentials should lead to a net effect of dissolution of zinc in the centre and deposition in the periphery.

There was no distinct difference in the appearance of the different electrodes after dismantling the cell; therefore, the influence of additives on the rate of SC could not be established. However, the higher rate of SC which is generally found for amalgamated zinc electrodes [1], could be explained by the more non-uniform potential distribution on discharging of the amalgamated electrode (cell 7, Fig. 6.14), compared to the non-amalgameted electrode (cell 9, Fig. 6.16); this would lead to a higher rate of material redistribution on discharging.

A mechanism of Shape Change, based on non-uniform current distributions, is not completely satisfactory, because it does not explain the accumulation of material at the bottom of the electrode upon cycling. The mechanism based on convective flows down by (electro) osmotic pumping of the membrane separator [13] does explain SC in the y-direction (see Fig. 2.3) but fails to explain Shape Change in the z-direction. Therefore, Shape Change seems to be caused by a combination of both these effects.

Moreover, it is found that the capacity decline of the cells as result of cycling, is greater than expected by the observed reduction in geometric surface area. Redistribution of the active material in the x-direction, leads to densification and this is thought to be responsible for the extra capacity decline.

6.6 Conclusions

- Different types of zinc electrodes were cycled. SC was observed in all cases and no distinct difference between the zinc electrodes without and with the HgO and PbO additive was observed. The change in porosity of the zinc electrodes, due to the incorporation of amalgamated zinc powder, is thought to be responsible for the steeper capacity decline with cycling.
- The decrease of the capacity and the increase of the zinc overpotential during charge are caused by exhaustion of the active zinc oxide material. After a number of cycles the zinc electrode has become the limiting electrode during discharge.

- The potential distribution along the surface was assumed to correspond
  with the current distribution; this is then found to be non-uniform and
  leads to a concentration gradient of zincate. The material redistribution,
  and thus the SC, was tentatively explained by diffusion of zincate along
  the surface.

6.7 Literature.

1. G.A. Dalin, in Zinc-Silver oxide batteries, A. Fleischer and
    J.J. Lander ed. Wiley, New York 1971, p. 87.
2. O. Wagner and A. Himy, in "Proc. 27th Power Sources symp.",
    PSC Publications Committee, Red Bank, N.J. 1976, p. 135.
3. A. Himy and O. Wagner, in "Proc. 28th Power Sources symp.",
    PSC Publications Committee, Red Bank, N.J. 1978, p. 167.
4. J. McBreen and E. Gannon, Electrochim. Acta 26 (1981) 1439.
5. J. McBreen, J. Electrochem. Soc. 119 (1972) 1620.
6. A. Himy, in "Proceedings of the 16th Intersociety Energy Conversion
    Engineering Conference", pp. 645-647, The American Society of Mecha-
    nical Engineers, New York (1981).
7. T.S. Chang, Y.Y. Wang and C.C. Wan, J. Power Sources 10 (1983) 167.
8. C.M. Shepherd and H.C. Langelan, J. Electrochem. Soc. 109 (1962) 657
    and 114 (1967) 8.
9. Z. Nagy and J. O'M.Bockris, J. Electrochem Soc. 119 (1972) 1129.
10. R.W. Powers, J. Electrochem.Soc. 118 (1971) 685.
11. W.G. Sunu and D.N. Bennion, J. Electrochem. Soc. 127 (1980) 2007, 2017.
12. H.E. Haring and W. Blum, Trans. J. Electrochem. Soc., 44 (1923) 313.
13. K.W. Choi, D.N. Bennion and J. Newman, J. Electrochem. Soc. 123
    (1976) 1616.

7. IMPEDANCE MEASUREMENTS

7.1. Introduction.

The use of the impedance technique for the study of electrode processes has expanded rapidly over the last three decades. With this technique information has been obtained on deposition and dissolution phenomena of the zinc electrode [1-7]. Characterization of primary cells, in which zinc is used as a negative electrode material, has also proved possible [8-10] and impedance data could be related with the state-of-charge of a battery.

In this chapter the behaviour of zinc and amalgamated zinc electrodes in alkaline zincate electrolyte is studied with the impedance method. Also, the porous zinc (zinc oxide) electrode in a Zn-NiOOH battery configuration was investigated using this technique, both in the charged and the discharged state and with the aim to find a correlation between cycling behaviour and impedance results.

7.2. Theory.

Starting from simple and well-known theory, based on the Randles circuit [11], we can best present the impedance frequency behaviour in a complex plot according to Sluyters [12]. An example of such a plot is given in Fig. 7.1, in which the components of the circuit are provided with commonly encountered values.
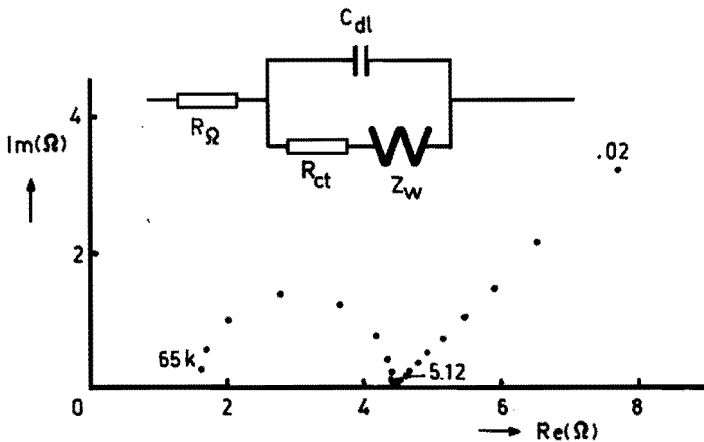
Fig. 7.1 Complex impedance plot with equivalent circuit: $R_\Omega = 1.6\Omega$; $\sigma = 1.0\Omega s^{-\frac{1}{2}}$; $C_{dl} = 6\mu F$; $R_{ct} = 2.8\Omega$.
Frequency range 0.02 Hz → 65 kHz (multiplication factor : 2)

As follows from the theory the so-called Warburg impedance

$$Z_W = \sigma\omega^{-\frac{1}{2}} - j\sigma\omega^{-\frac{1}{2}} \qquad (7.1)$$

becomes dominant at low frequencies: Z becomes a straight line with unit slope, characteristic for a diffusion controlled electrode reaction in the absence of convection.

For a reversible metal–metal ion electrode process $(\sigma)_{rev}$, the Warburg coefficient, and $(R_{ct})_{rev}$, the charge transfer resistance, are [12]

$$(\sigma)_{rev} = \frac{RT}{n^2F^2A} \frac{1}{(2D)^{\frac{1}{2}}c_{ox}^{\sigma}} \qquad [\Omega \ s^{-\frac{1}{2}}] \qquad (7.2)$$

$$(R_{ct})_{rev} = \frac{RT}{nFI_o} \frac{\left(c_{oc}^{S}\right)^{1-\alpha}}{\left(c_{ox}^{\sigma}\right)} \qquad [\Omega] \qquad (7.3)$$

where A   = surface area of the electrode [cm^2]

  D   = diffusion coefficient of the metal ion [cm^2 s^{-1}]

  c_{ox}^{σ} = concentration of metal ion at the [mol.cm^{-3}]

    electrode surface

  c_{ox}^{S} = concentration of metal ion in the bulk phase [mol.cm^{-3}]

  I_o = exchange current [A]

  n   = electrons per molecule oxidized or reduced

  α = cathodic transfer coefficient

When the mass transport in the solution is influenced by natural or forced convection the Warburg impedance behaviour changes [12]. In Fig. 7.2 the complete impedance plot is shown for the case of forced convection. At decreasing frequency the imaginary part tends to zero
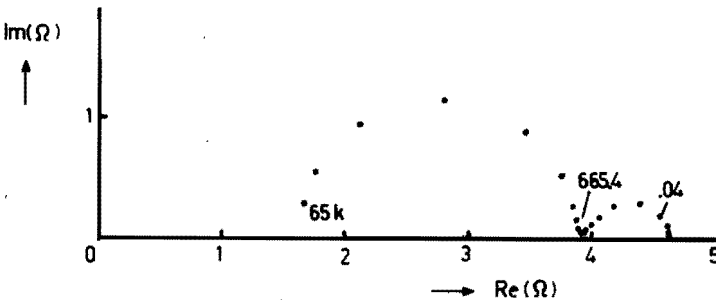
Fig. 7.2.   Total impedance of the Randles circuit with forced convection (2000 RPM). R_Ω=1.63Ω; R_{ct}=2.25Ω; σ=1.0Ωs$^{\frac{1}{2}}$; C_{dl}=6μF; D=2.1·10^{-6}cm^2 s^{-1}; δ=7.8·10^{-4}cm. Frequency range: 0.01 Hz → 65 kHz (multiplication factor : 2).

and the real part becomes [12]

$$\lim_{\omega \to 0} Z'_W = \sigma\delta\left(\frac{2}{D}\right)^{\frac{1}{2}}$$

(7.4)

where δ = thickness of the Nernst-diffusion Layer (cm).

In the case of heterogeneous reactions, surface processes such as adsorption, surface diffusion and lattice formation must be taken into account. Two models which include surface diffusion of adatoms and the adsorption of intermediates will be outlined briefly.

(A) Based on the well-known adatom mechanism for metal-ion exchange reactions [13]

$$M_{latt} \to M_{ad} \to M^{z+}_{solution} + ze^{-}$$
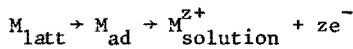
Fleischmann et al. [14] have proposed an analogous circuit in which additional components expressing surface adsorption and surface diffusion and lattice formation, are included, Fig. 7.3.
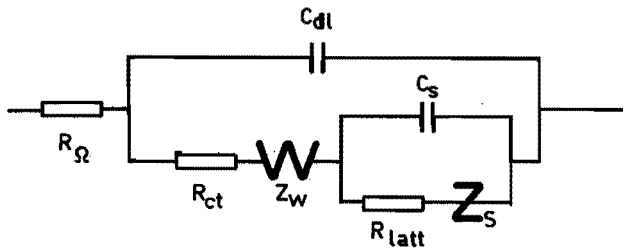
Fig. 7.3. Equivalent circuit in which additional components expressing surface processes are included in the Randles circuit.

C_s represents a pseudo-capacitance, Z_s the adatom diffusion impedance and R_{latt} the impedance due to lattice formation. At equilibrium potential these are defined [14] by

$$C_s = \frac{z^2 F^2 A}{RT} c^o_A$$

(7.5)

$$Z_s = \sqrt{\frac{k_2}{D_a}} \frac{1}{zFI_o} \sqrt{\frac{1}{1+j\omega/k_2}}$$

(7.6)

where C_s = pseudo capitance [F]

c_A^o = adatom concentration $[mol.cm^{-2}]$

$k_2 = I_o/(zFc_A^o A)$ $[s^{-1}]$

Z_s = adatom diffusion impedance $[\Omega]$

D_a = diffusion coefficient along the curface $[cm^2\ s^{-1}]$

$2l$ = distance between two parallel steplines on the surface $[cm]$

In Fig. 7.4 a plot of this equivalent circuit is shown in case $\omega/k_2 \ll 1$
so the Z_s-term can be simplified to

$$Z_s = \sqrt{\frac{k_2}{D_a}}\ 1 \cdot \frac{RT}{zFI_o} \qquad\qquad (7.7)$$

R_x is defined as

$$R_x = Z_s + R_{latt} \qquad\qquad (7.8)$$
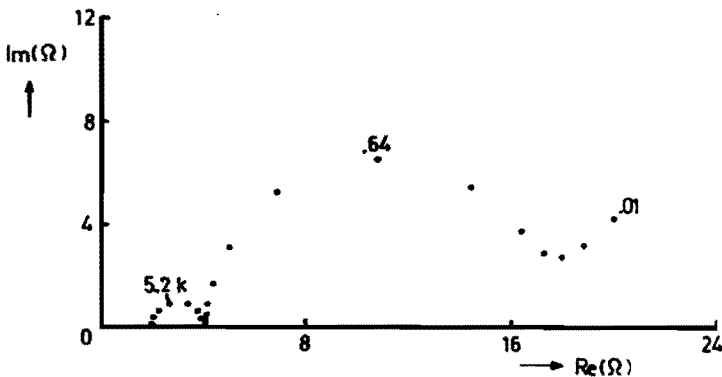
Fig. 7.4. Total impedance of the equivalent circuit of Fig. 7.3 with the
following parameter values:
$R_\Omega=2\Omega$; $R_{ct}=2\Omega$; $R_x=12\Omega$; $C_{dl}=20\mu F$; $C_s=20mF$; $\sigma=1\Omega s^{-\frac{1}{2}}$; Frequency
Range 0.01 Hz → 65 kHz (multiplication factor : 2)

(B) The other approach was first used by Gerischer and Mehl [15] and later
by Epelboin & cs.in the study of dissolution and electrocrystallization
phenomena [1,16].
The mathematical analysis of the impedance characteristics can be
described as follows. The response of the total current for a mechanism
that involves n intermediate species (surface coverages θ_1 .... θ_n) to
a sinusoidal potential pertubation is given by

$$\delta i = \left(\frac{\partial i}{\partial E}\right)_{\theta_1, \ldots, \theta_n} \delta E + \sum_{i=1}^{n} \left(\frac{\partial i}{\partial \theta}\right)_{\theta_j, E} \delta \theta_i \qquad (j \neq i) \qquad (7.9)$$

so, the faradaic admittance is given by

$$Y_f = \frac{\delta i}{\delta E} = \left(\frac{\partial i}{\partial E}\right)_{\theta_1, \ldots, \theta_n} + \sum_{i=1}^{n} \left(\frac{\partial i}{\partial \theta}\right)_{\theta_j, E} \frac{\delta \theta_i}{\delta E} \qquad (j \neq i) \qquad (7.10)$$

The derivation of the expression for the impedance $(Z = \frac{1}{Y})$ is completed by the evaluation of the terms on the right hand side of equation (7.10) for the mechanism of interest.

In the case of the electrocrystallization of nickel and cobalt [16], it is supposed that Me(OH) adsorbs at the interface and acts as an intermediate compound (and not as a catalyst). Several simplifying assumptions are made such as absence of convective diffusion. Depending on the parameters in the final expression of the impedance, the faradaic impedance can be either inductive or capacitive. For an inductive faradaic impedance, the equivalent circuit of the electrode overall impedance is given in Fig. 7.5.
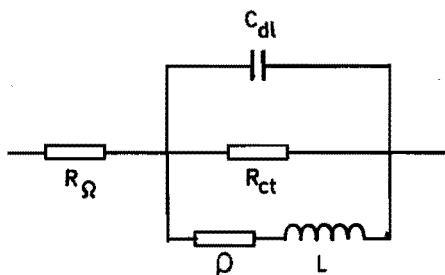
Fig. 7.5.
Equivalent circuit of the electrode impedance for the electrocrystallization process of a metal via an intermediate compound [16].
ρ = faradaic resistance;
L = self-inductance.

In the case of zinc electrocrystallization, Epelboin et al. [1] observed an impedance diagram which reveals several semicircles both capacitive and inductive ones. They assumed adsorption at the interface of three species: $H_{ad}(\theta_1)$, $Zn^+_{ad}(\theta_2)$ and $ZnA_{ad}(\theta_3)$ (A is an anion) and a coupling between the heterogeneous reactions, one of them being autocatalytic. This corresponds with the relaxation of the $C_{dl}-R_{ct}$ circuit and the coverage fractions of the three adsorbed species.

Therefore, their model can explain the existence of an inductive faradaic impedance characterized by at least three time constants. In Fig. 7.6 a simulated and measured impedance diagram of the electrocrystallization of zinc in alkaline zincate solution is given.
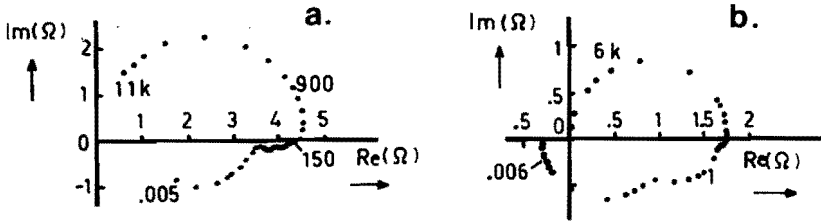
Fig. 7.6.a. Simulated impedance diagram of the electrocrystallization of
zinc, according to the model of Epelboin et al. [1]

b. Measured impedance diagram of the electrocrystallization of
zinc (electrolyte: 7 M KOH/0.25 M ZnO; 5000 RPM;
$i = 35.7$ mA·cm^{-2}; $E = -1.613$ V/SCE). frequency in hertz.

The model has been extended to incorporate surface diffusion and additives
[2-5]. The morphology of different zinc electrodeposits was explained by
taking into account a coupling between the surface diffusion of Zn^+_{ad} and
the interfacial reaction [2]. The impedance measurements have also been
carried out in the dissolution range, for various electrolyte compositions
[6]. It was concluded that at least four adsorbates are involved corres-
ponding to four faradaic relaxation processes.
Furthermore, impedance spectra have been obtained during the cycling of a
zinc electrode in an alkaline zincate solution to imitate the situation in
a real battery system [7]. Drastic changes in the impedance diagrams were
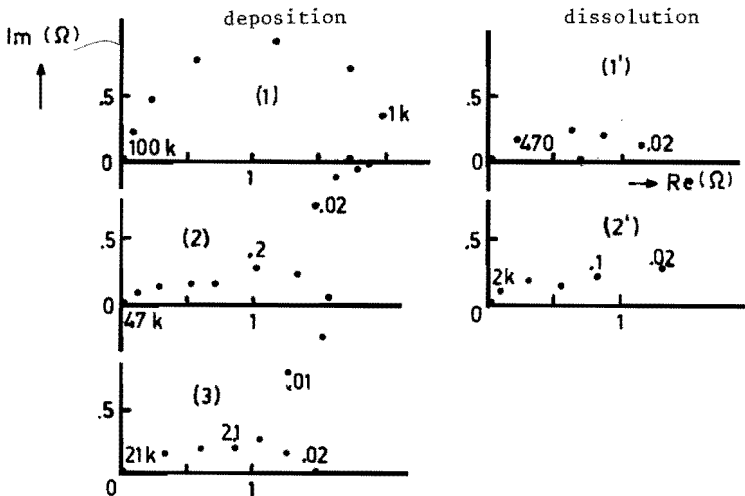
Fig. 7.7 Impedance diagrams obtained during the cycling of a zinc elec-
trode (2600 RPM) [7].
electrolyte : 5 M KOH/0.5 M ZnO; $i=25$ mA·cm^{-2}; cycling period:
1 hour (cycle numbers in brackets, frequency in hertz)

observed during cycling (Fig. 7.7), indicating an increase in electrode area and a variation of the electrode kinetics with cycling. Also the kinetics of zinc deposition appear to be very sensitive to the contamination of the electrolyte by dissolution products.

Besides these more fundamental studies, also the impedance of electrical storage cells, particularly the primary batteries, have been measured for practical purposes. This impedance is of interest not only for the purpose of predicting the battery behaviour in electronic circuits but also because it can be a useful diagnostic for assessing their quality i.e. the state-of-charge.

The Leclanché cell [8], the alkaline zinc-manganese dioxide cell [9] and the alkaline zinc-mercuric oxide cell [10] have been examined as a function of the state-of-charge.

The impedance diagram of a Leclanché cell can be explained in terms of control by charge transfer and diffusion at the rough zinc electrode, because this electrode has a nominally planar configuration whereas the cathode (the depolarizer) has a larger surface area, due to the finely divided carbon, which is used as a conductor. The in-phase component of the impedance at 31.2 Hz was found to be a good indicator for the state of charge between 100 and 90% (Fig. 7.8).
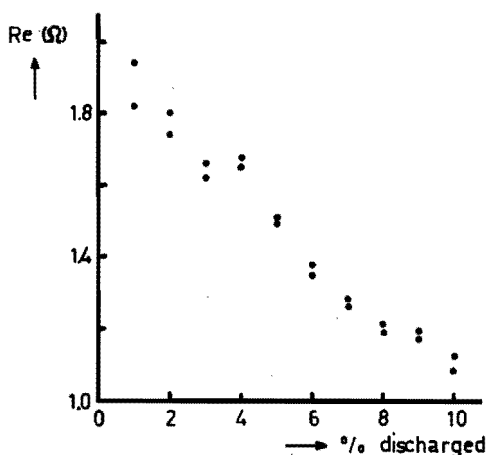

Fig. 7.8.
In-phase component of the impedance at 31.2 Hz as function of the state-of-charge between 100 and 90% [8].

The impedance diagram of the alkaline $Zn-MnO_2$ cell is complicated, because here the manganese dioxide electrode has also to be included in the equivalent circuit. Though the interpretation of the impedance data was successfully accomplished up to 80% discharge, it was not possible to find a reliable correlation with the state-of-charge.

The behaviour of the zinc-mercuric oxide cell conforms to that expected for rate control by charge transfer at the zinc electrode and diffusion in the solution (Fig. 7.9). At low frequencies a relaxation of the diffusive circuit elements is observed which results in a complete suppression of the capacitive component of the impedance at low frequency. A simple linear relation was found between the state-of-charge and the charge transfer resistance, R_{ct}.
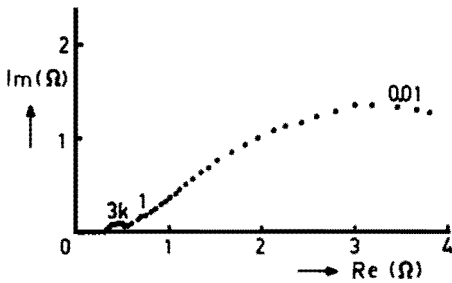

Fig. 7.9.
Complex plane plot for as manu-factured alkaline Zn-HgO cell; $22^{\circ}C$; zero current density [10].

7.3. Experimental

7.3.1. Electrodes and Cell.

Several types and forms of zinc electrode were investigated:
1. Disc electrode (0.28 cm^2): non-amalgamated type and three types of amalgamated electrodes. Zn(Hg,I) and Zn(Hg,II) consist of pre-amalga-mated zinc-alloys containing 1 resp. 6 wt% mercury and Zn(Hg,III) is amalgamated by immersing a zinc electrode in a solution of mercuric chloride in acetone (see Chapter 5).
2. Porous electrode (3.5 x 3.9 cm^2): pasted zinc oxide on a silver plated nickel screen, without and with metal oxide additives (2% PbO or 2% HgO).

The impedance measurements of the disc electrodes were carried out in the three-compartment cell, already described in chapter 5. The pretreatment is also given in that chapter. The electrolyte was an alkaline solution with concentrations ranging from 1.5 to 10 M KOH and 0.01 to 0.1 M ZnO. Most of these measurements were performed immediately after the galvano-static pulse measurements, at both 0 and 2000 RPM. The latter rotation frequency was chosen in order to minimize the convective diffusion of the chemical species towards the electrode.

The impedance measurements at the porous electrodes were performed in the
nickel oxide battery configuration with 9.5 M KOH/0.5 M ZnO/0.5 M LiOH.
The construction of these cells was described in chapter 6. A reference
electrode was used in these cells (see Fig. 6.2, Chapter 6). By means of
this three-electrode configuration the impedance of the zinc electrode
could be determined, as well as the impedance of the total cell.

7.3.2. Instrumentation.

The apparatus used for the impedance measurements incorporates a frequency-
response-analyser (Solartron 1250), an electrochemical interface (Solartron
1186) and a microcomputer (HP 9816), which completely controls the expe-
riment (see Fig. 7.10).
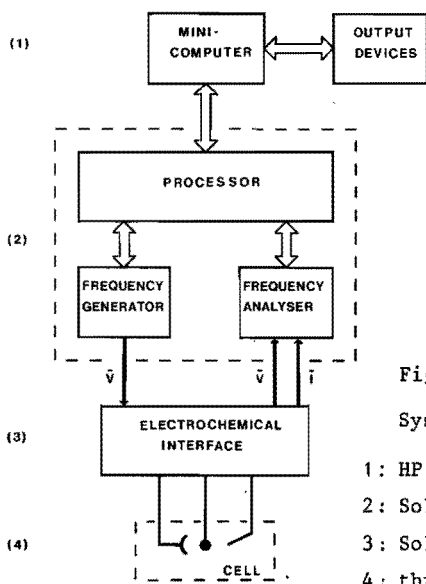
Fig. 7.10

System set up for impedance measurements

1: HP 9816 disktop computer and output devices
2: Solartron 1250 frequency response analyser
3: Solartron 1186 electrochemical interface
4: three-electrode cell

Measurements were made at frequencies in the range of 0.01 Hz to 10 kHz for
battery experiments and from 0.01 Hz to 65 kHz for the experiments at the
disc electrodes. The amplitude of the sinusoidal potential pertubation is
1 mV (rms).
Most of the impedance diagrams were determined at the restpotential of the
zinc electrode. Some experiments were carried out superimposed on a dc-
current, anodic or cathodic.

The impedance measurements of the nickel oxide-zinc battery were carried out at zero current density as a function of the state-of-charge and the cycle number [The state-of-charge is defined as 100%, at 0.5 Ah or less if the voltage on charging reaches about 2.2 V, and 0%, when the voltages on discharging reaches 1.35 V (see Chapter 6)].

In order to get reliable results the standard resistor of the "Interface", which is required for the purpose of current to voltage conversion, has to be of the same order of magnitude as the resistance of the battery. This then requires an external standard resistor of about 200 mΩ, otherwise measurements become inaccurate.   Fig. 7.11 shows impedance data measured at the dummy cell using three different standard resistors (R_s). Since these diagrams do not coincide, it must be concluded that the "Interface" itself has an additional internal resistance. Correcting for an internal resistance of about 110 mΩ results in identical impedance diagrams as shown in Fig. 7.12; only at frequencies higher than 10 kHz deviations occur, indicating
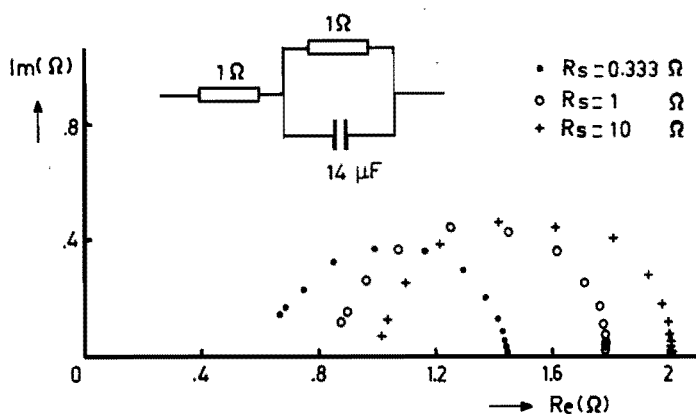
Fig. 7.11   Effect of standard resistor of the Interface 1186 on the
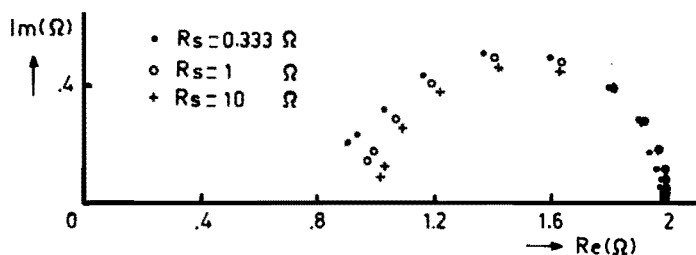   impedance of a dummy cell.

Fig. 7.12   Corrected impedance diagram of the dummy cell, measured with
            different standard resistor values and corrected for the internal
            resistance of the system (about 110 mΩ)

that with smaller external standard resistors the measurements become un-
reliable. Therefore, all battery experiments were carried out at frequen-
cies lower than 10 kHz.

7.4. Disc electrodes.

7.4.1. Results amalgamated zinc electrodes.

In Fig. 7.13 a typical impedance spectrum of the Zn(Hg,III)-electrode is
shown at its rest potential in 7 M KOH/0.1 M ZnO (unstirred solution). The
spectra of the Zn(Hg,I)- and Zn(Hg,II) electrodes are similar and can be
described with the Randles equivalent circuit of Fig. 7.1.
From the impedance plot the exchange current density (i_o), the capacity of
the double layer (C_{dl}), the Warburg coefficient (σ) and the diffusion coef-
ficient of the zincate ion (D) can be calculated. As is clear from Fig.
7.13 the simulated impedance plot for the Zn(Hg,III) electrode is in good
agreement with the measured values.
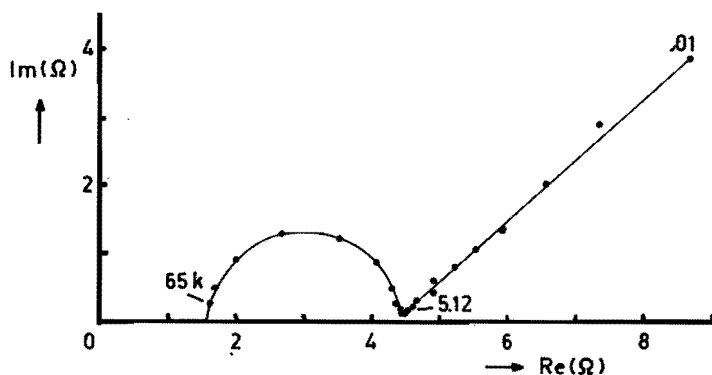
Fig. 7.13 Measured impedance plot ($\bullet$) of Zn(Hg,III).
electrode in 7 M KOH/0.1 M ZnO at the rest potential
(E_r=-1.382 V vs Hg/HgO) at 0 RPM
Simulated impedance plot (——)
Frequency range : 0.01 Hz → 65 kHz (multiplication factor : 2)

In Table 7.1 the results of all experiments are tabulated as a function of
the electrolyte composition and the kind of amalgamated surface.
The Table shows that the kind of amalgamation and the concentration of the
electrolyte to not noticeably influence the i_o- and C_{dl}-values.

100

Table 7.1 i_o, C_{dl}, σ and D as function of the solution composition and the kind of amalgamated surface.

Electrolyte	electrode	i_o (A/cm^2) x 10^4	C_{dl} $(\mu F/cm^2)$	σ $(\Omega\ s^{-\frac{1}{2}})$	D_{Zn} $(cm^2/s$ x $10^6)$
10 M KOH/0.1 M ZnO	Zn(Hg,I)	200-290	28-34	1.16-1.23	1.9-2.1
"	Zn(Hg,II)	240-270	30-33	1.02	2.7
"	Zn(Hg,III)	200-210	25	1.12	2.3
7 M KOH/0.1 M ZnO	Zn(Hg,I)	190-260	23-25	1.09	2.4
"	Zn(Hg,II)	240-294	30-32	1.08	2.4
"	Zn(Hg,III)	160-250	23-24	1.08	2.4
3 M KOH/0.1 M ZnO	Zn(Hg,I)	330-650	53-68	0.97	3
"	Zn(Hg,II)	50-250	23-32	0.92	3.3
"	Zn(Hg,III)	175-650	44-66	0.89	3.6
15 M KOH/0.01 M ZnO	Zn(Hg,I)	66-102	31-32	8.2	4.2
"	Zn(Hg,II	63-115	28-39	5.2	10.4
"	Zn(Hg,III)	-	-	-	-

When the disc electrode is rotated, the low frequency domain of the impedance diagram changes. A typical diagram is shown in Fig. 7.14 (The three amalgamated electrodes produce similar diagrams). These diagrams can also be described with the Randles circuit, in which now the Warburg impedance has to be corrected for convective transport.
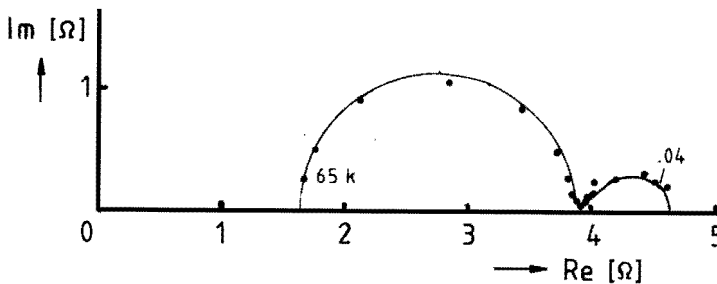

Fig. 7.14 Measured impedance plot (•) of Zn(Hg,III)-electrode in
7 M KOH/0.1 M ZnO at the rest potential (E_r=-1.382 V vs.
Hg/HgO) at 2000 RPM
Simulated impedance plot (——)
Frequency range: 0.02 Hz → 65 kHz (multiplication factor : 2)

The thickness of the Nernst diffusion layer (δ) can be obtained from the real part of the Warburg impedance, using equation (7.4). This result can be compared with the value, calculated from the Levich equation

$$\delta = 1.61 \ D^{1/3} \omega_r^{-1/2} \nu^{1/6}$$ (7.11)

where

D = diffusion coefficient of zincate $[cm^2 \ s^{-1}]$

ω_r = angular frequency of rotation $[s^{-1}]$

ν = kinematic viscosity $[cm^2 \ s^{-1}]$

Table 7.2 The Nernst diffusion layer δ as calculated with equation (7.4) and (7.11), respectively
(D and σ are obtained from Table 7.1 and ν from [17])

Electrolyte	$\lim\limits_{\omega \to 0} Z'_w$ (Ω)	σ ($\Omega \ s^{-\frac{1}{2}}$)	D ($cm^2 \ s^{-1}$)	ν ($cm^2 s^{-1} \times 10^2$)	$\delta(cm) \times 10^4$	
					via equation 7.4	via equation 7.11
10 M KOH/0.1 M ZnO	0.8-0.9	1.1	$2.3 \ 10^{-6}$	2.79	7.8-8.8	8.1
7 M KOH/0.1 M ZnO	0.7-0.9	1.1	$2.4 \ 10^{-6}$	1.84	7.0-9.0	7.7
3 M KOH/0.1 M ZnO	0.7-0.8	0.9	$3.3 \ 10^{-6}$	1.23	10.0-11.4	8.0
15 M KOH/0.01 M ZnO	3.3-4.2	6	$6 \ 10^{-6}$	1.10	9.5-12.1	9.5

In Table 7.2 the δ-values are summarized.
The agreement between the δ-values calculated respectively from the impedance data and the Levich equation is good. The simulated impedance diagram (Fig. 7.14) also agrees well with the measured data. Supposition of ac signals on a dc-current, whether anodic or cathodic, results in similar diagrams as observed at the rest potential. A typical diagram, at anodic dc-current of 10 mA/cm^2, is shown in Fig. 7.15. However, due to the dissolution or deposition process the surface of the electrode changes, continuously, so affecting the impedance measurements. A striking example is given in Fig. 7.16. At longer deposition times an inductive loop is observed in the impedance diagram. Such a diagram is typical for a non-amalgamated zinc electrode as will be shown in the next part.
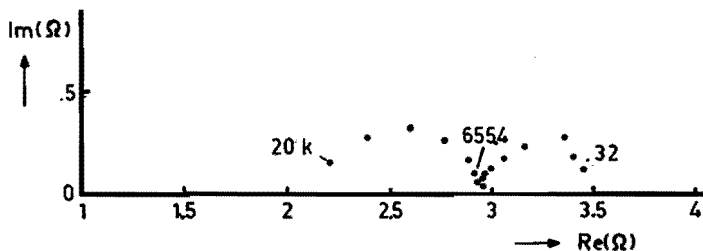

Fig. 7.15 Measured impedance plot of Zn(Hg,II)-electrode in
7 M KOH/0.1 M ZnO at 2000 RPM. numbers indicate frequency;
i_a = 10 mA cm^{-2}
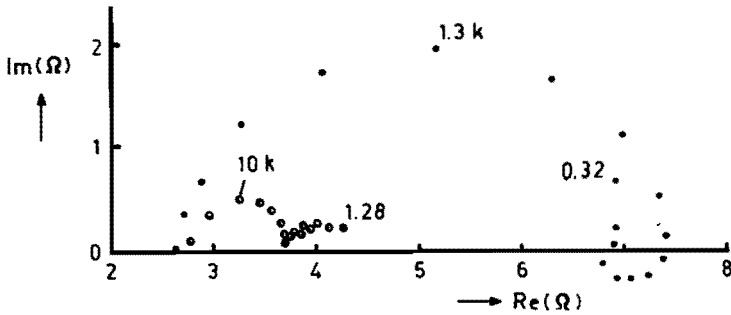
Fig. 7.16   Measured impedance plot of Zn(Hg,II)-electrode in
            5 M KOH/0.1 M ZnO at 2000 RPM ;
            i_c : 10 mA cm^{-2};   o : directly after pretreatment
                                       • : after ca. 20 min. deposition

Therefore, it is not justifiable to obtain kinetic parameters from such
measurements. The gavalnostatic pulse method, as discussed in chapter 5, is
more apt for this purpose.

7.4.2.   Results non-amalgamated zinc electrode.

In Fig. 7.17 the impedance spectrum of the zinc electrode in 7 M KOH/0.1 M
ZnO is given at the rest-potential at 0 RPM. The spectrum is quite different
from that of an amalgamated electrode (Fig. 7.13). The small semicircle at
high frequencies if followed by a pattern consisting of a semicircle and a
straight line. This part often masks the semicircle at high frequencies.
The impedance spectra can be understood qualitatively from the equivalent
circuit of Fleischmann et al. [14] (depicted in Fig. 7.3). The simulated
curve, based on this equivalent circuit is also shown.
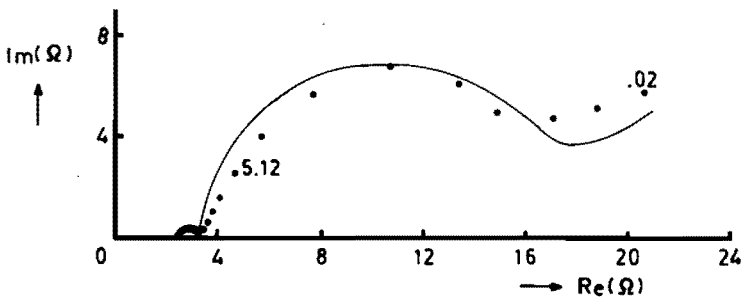

Fig. 7.17   Measured impedance spectrum of the zinc electrode in
            7 M KOH/0.1 M ZnO at 0 RPM (•) ; numbers indicate frequency;
            Simulated impedance plot   (——)

The agreement is reasonable taking into account that the surface of the
zinc electrode changes somewhat during the measurement. In Table 7.3 values
of R_{ct}, i_o, C_{dl}, C_S, c_A^o (with equation (7.5) and σ are tabulated as function
of the solution composition for a series of experiments.

Table 7.3 R_{ct}, i_o, C_{dl}, R_x, C_s and c_A^o as function of the solution composition at a zinc electrode.

Electrolyte	R_{ct} $(\Omega\,cm^2)$	i_o (A/cm^2) x 10^4	C_{dl} $(\mu F/cm^2)$	R_x $(\Omega\,cm^2)$	C_s (mF/cm^2)	c_A^o (mol/cm^2) x 10^9	σ $(\Omega\,s^{-\frac{1}{2}})$
10 M KOH/0.1 M ZnO	0.4-1.0	120-290	60-80	3-28	60-70	4-5	2-6
7 M KOH/0.1 M ZnO	0.2-0.6	200-750	70-180	4-20	20-80	2-5	2-6
3 M KOH/0.1 M ZnO	0.1-0.3	500-1500	50-100	4-11	44-120	3-8	2-6
15 M KOH/0.01 M ZnO	10-26	50-150	60-75	24-34	0.6-1.0	0.04-0.07	10-20

Comparing Tables 7.3 and 7.1, it appears that i_o-values are somewhat higher
than for the amalgamated electrodes, though the scatter is rather large.
The double layer capacity is twice that of the amalgamated zinc electrode.
The impedance diagram at a rotating zinc-disc electrode, shown in Fig. 7.18,
is quite similar to that of a non-rotating electrode (Fig. 7.17). Only the
Warburg impedance at low frequencies is not observed and it appears that
the resistance in the RC-circuit, which relaxes at low frequencies, is
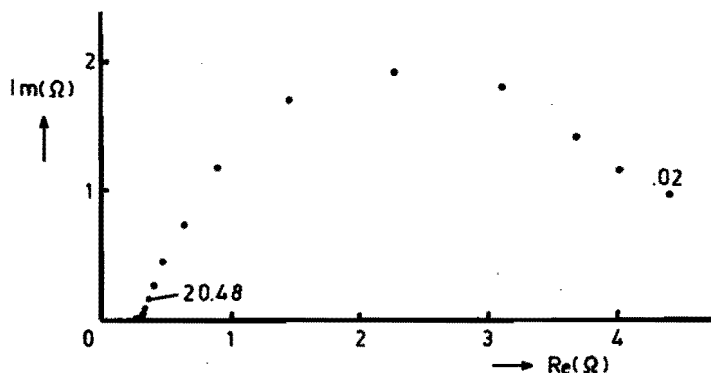about 2-5 times larger than in the absence of rotation.

Fig. 7.18 Measured impedance spectrum of the zinc electrode in
3 M KOH/0.1 M ZnO at 2000 RPM; numbers indicate frequency

Superposition of ac-signals on a dc-current changes the impedance diagrams
drastically. Fig. 7.19 shows the spectra obtained with an anodic dc-current
of 3.5 (a) resp. 35 (b) mA/cm^2. Increase of the dc-current leads to a

strong reduction of the large semi-circle observed at the rest potential. It seems that this reduced semi-circle overlaps the semi-circle due to the relaxation of the $R_{ct}C_{dl}$-circuit. Also, an inductive and an additional capacitive loop are observed. According to Epelboin et al. [1,16] this should indicate the presence of two intermediates in the electrode reaction.
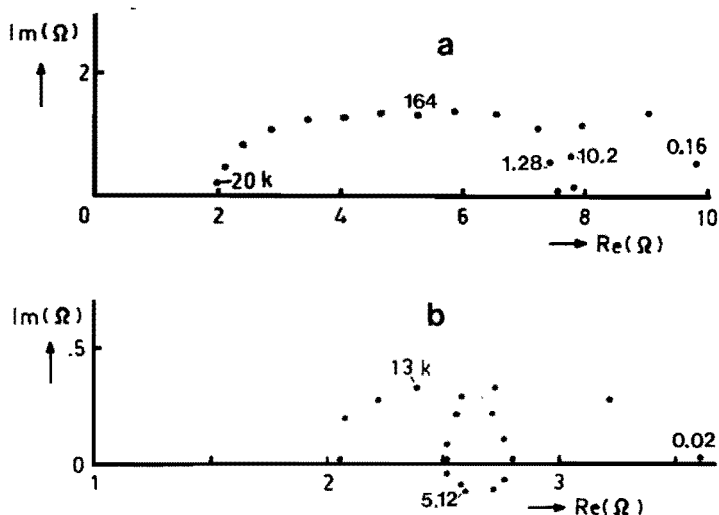
Fig. 7.19   Impedance spectra of a zinc electrode in 7 M KOH/0.1 M ZnO at 2000 RPM ; numbers indicate frequency

a : i_a = 3.5 mA cm^{-2}

b : i_a = 35 mA cm^{-2}

With a cathodic dc-current similar diagrams are observed (Fig. 7.20). Here also, the large semi-circles shrink with increasing current and an inductive and an additional capacitive loop are observed.

7.4.3   Discussion

The total impedance of the amalgamated electrodes can be adequately described with a model consisting of a kinetic and a diffusion controlled part, if necessary corrected for forced convection. Since no difference was found between the impedance spectra for Zn (Hg,I-II-III)-electrodes, it can be concluded, that the kind of amalgamation has no effect i.e. at all three electrodes sufficient mercury is present to cover the surface completely. Probably, as a result of the electrode pretreatment, in which more zinc dissolves than deposits, concentration of mercury on the surface takes place, leading to a complete coverage.
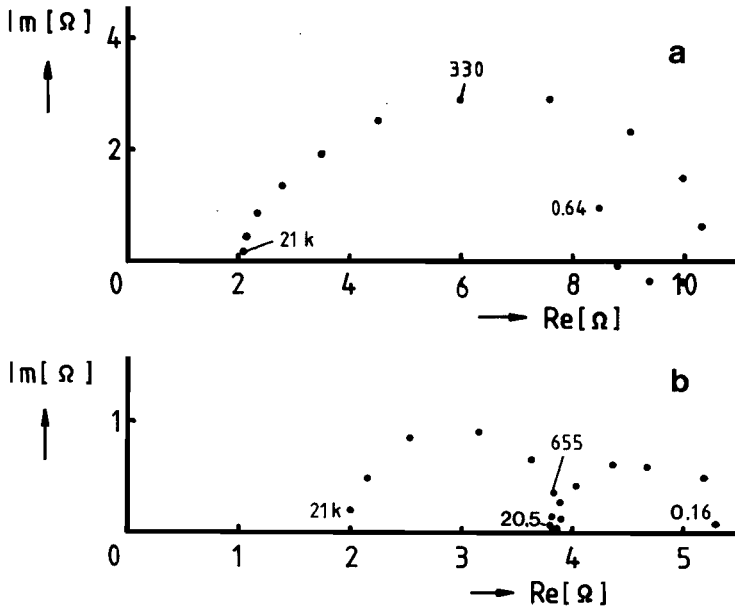
Fig. 7.20 Impedance spectra of a zinc electrode in 7 M KOH/0.1 M ZnO
at 2000 RPM ; numbers indicate frequency
a : i_c = 3.5 mA cm^{-2}
b : i_c = 35 mA cm^{-2}

In Table 7.4 the i_o values obtained from impedance measurements at the three
amalgamated electrodes are compared with the i_o values from the galvano-
static pulse technique (Table 5.6). As is evident there is a fair agreement
between these i_o values.

Table 7.4 Comparison of i_o-values at amalgamated zinc electrodes
calculated via different measuring techniques.

electrolyte	i_o (A cm^{-2}) $\cdot$ 10^4	
	impedance technique	galvanostatic pulse technique
10 M KOH/0.1 M ZnO	200-290	130-200
7 M KOH/0.1 M ZnO	60-300	130-270
3 M KOH/0.1 M ZnO	50-650	100-300
1.5 M KOH/0.01 M ZnO	60-120	10-160[□]

[□]not given in Table 5.6

The hydroxyl concentration has no influence on the i_o values, as was the
case in the galvanostatic pulse technique. In Table 7.5 i_o values are com-
pared that were obtained in direct sequence with the two different tech-
niques at the same Zn(Hg,III)-electrode. Here too, the agreement is
excellent.

Table 7.5 Comparison of i_o-values, obtained with two different
techniques at the same electrode surface [Zn(Hg,III)]

electrolyte	$i_o (A\ cm^{-2}) \cdot 10^4$	
	impedance technique	galvanostatic pulse technique
10 M KOH/0.1 M ZnO	200-210	120-150

The σ values (Table 7.1) change with decreasing hydroxyl concentration
which means an increase of the diffusion coefficients of zincate (D). The
D-values agree well with literature date [18] [$(1.5-7)\cdot10^{-6}\ cm^2\ s^{-1}$ (25°C)
in the hydroxyl concentration range of 1-12 M].
The impedance diagrams of the amalgamated electrodes measured with a sine
superimposed on a dc-current do not significantly change with respect to the
diagram at rest potential, i.e. the shape of the diagrams is similar, only
the values of the charge transfer (R_{ct}) and of $\lim_{\omega \to 0} Z'_W$ (which is proportional
to σ, see eq. 7.4, are affected. The zincate concentration at the surface
(c_{ox}^{σ}), which is dependent on the underlying dc-current, influences the R_{ct}
and σ values via equations (7.2) and (7.3).
The striking difference between the impedance spectra of zinc and amal-
gamated zinc electrodes clearly indicates that, at zinc, surface processes
play a more important role. It was shown in Fig. 7.17 that the results
can adequately be described with the analogous circuitry of Fig. 7.3. From
the impedance data at high frequencies i_o values were calculated (cf. Table
7.3). These values are of the same order of magnitude as the i_o values
obtained with the galvanostatic puls technique (Table 5.1). Table 7.6 com-
pares the two series of data. The agreement is fair, but the scatter of the
datapoints is large.
In Table 7.3 values are given for the surface concentration c_A^o as calculated
with equation (7.15). The number of zinc atoms in the compact plane (0001),
where the interatomic distance is 2.66 Å [17] is $2.7\ 10^{-9}\ mol\ cm^{-2}$.

Table 7.6 Comparison of i_o-values at the zinc electrode calculated
via different measuring techniques.

| electrolyte | i_o (A cm^{-2}) $\cdot$ 10^4 | |
	impedance technique	galvanostatic pulse technique
10 M KOH/0.1 M ZnO	120-290	84-380
7 M KOH/0.1 M ZnO	200-750	77-400
3 M KOH/0.1 M ZnO	500-1500	140-145
1.5 M KOH/0.01 M ZnO	50-150	80-260°

^{o} not given in Table 5.1

From this, it follows that in 0.1 M ZnO solutions the surface of the zinc
electrode is completely covered with zinc adatoms, so surface diffusion
cannot play an important role in the model according to Fleischmann et al.
[14]. Therefore, the resistance R_x must be attributed to R_{latt}, the resis-
tance of lattice formation (equation (7.8)). However, this explanation
cannot be satisfactory either, because from the impedance measurements in
the presence of a dc-current (Fig. 7.19) it can be deduced that this resis-
tance decreases strongly with increasing dc-current or overpotential. This
is rather unlikely for a resistance due to lattice formation, particularly
in view of the already very high surface adatom concentration. For this
reason, another process which is dependent on the activation potential must
be responsible for the resistance R_x.
In the model of Epelboin [1,16], too, intermediate species are considered
in the explanation of impedance diagrams.
Epelboin et al. [1] observed, during zinc electrocrystallization, an impe-
dance diagram with an inductive faradaic part, characterized by at least
three time constants. These are ascribed to the involvement of three inter-
mediate species in the total reaction [H_{ad}, Zn^+_{ad} and ZnA_{ad} (A is an anion)].
Cachet, Ströder and Wiart [6] pointed out four faradaic relaxation processes
in the impedance diagrams during steady-state polarization measurements.
From these results they concluded to at least four adsorbed intermediate
species at the interface. The intermediate species, however, were not
identified.
Using an anodic or cathodic dc-current we likewise observed an extra induc-
tive and capacitive loop. This would suggest, according to Epelboin et al.

[1,16], that two intermediates are involved in the total reaction
Therefore, no agreement exists on the number and kind of the intermediates.
The relaxation processes, observed in [1,6], take place partly in the very
low frequency region (< 0.1 Hz).
The question here is whether the impedance data measured at such low frequen-
cies (requiring very long measuring times) are not influenced by the change
of the surface as a result of the deposition or dissolution process. This
change can be seen very clearly during the deposition of zinc onto an amal-
gamated zinc surface (Fig. 7.16). It can also be seen in Fig. 7.7 [7] that
deposition or dissolution affects the impedance diagram drastically. There-
fore, not much value should be attached to the very low frequency measure-
ments (< 0.1 Hz); it seems likely that intermediate species are involved in
the reaction.

7.5.   Porous electrodes: Results and Discussion.

Fig. 7.21 shows the impedance spectra of the zinc electrode, the nickel
oxide electrode and the total cell in the discharged state after the first
charge/discharge cycle of the battery. It can be seen that both electrodes
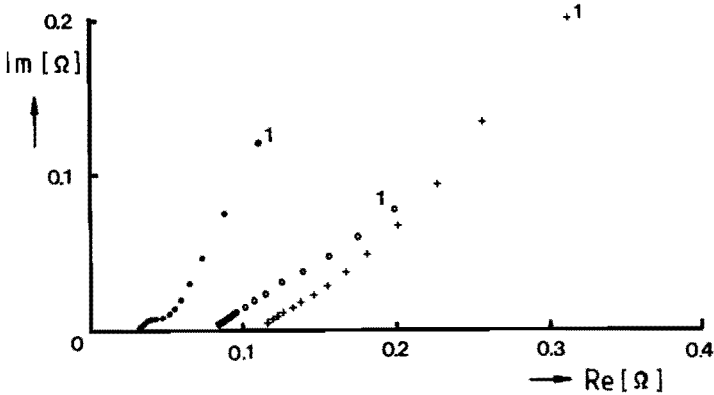contribute to the impedance of the total cell. Vectorial addition of the

Fig. 7.21   Impedance spectra of nickel oxide-zinc battery after the first
            charge/discharge cycle
            • : zinc electrode
            o : nickel oxide electrode
            + : total cell
            Frequency Range:1 Hz → 5000 Hz (multiplication factor : 2).

109

impedance of the two individual electrodes results in an impedance diagram,
which is nearly identical with the measured impedance of the total cell: the
difference is smaller than 10 mΩ in the frequency range of 1 to 3000 Hz.
In the following, only the impedance of the Zn-electrode will be considered.
Fig. 7.22 shows the impedance of a fresh zinc oxide electrode (uncharged)
and at various states-of-charge (as defined in Chapter 6): in the uncharged
state the impedance is capacitive.
During the first charging the impedance diagram changes considerably: the
capacitive character decreases and, in fully charged state (about 0.50 Ah)
a curve becomes visible which is characteristic for kinetic and mass trans-
port controlled processes. For a flat electrode the Warburg impedance
should be a 45° straight line.
However, the angle is smaller than 45°, which points to the porous character
of the zinc electrode [19]. During this first charging the ohmic resistance
of the electrolyte increases due to the formation of gas bubbles (hydrogen).
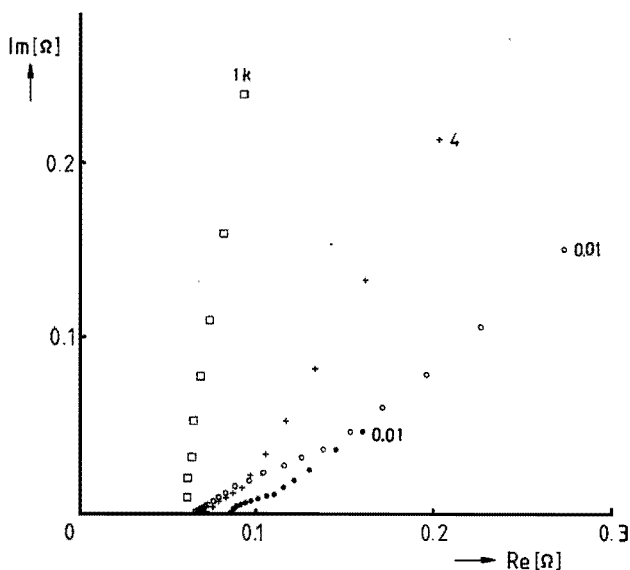

Fig. 7.22   Effect of the 1st discharge on the impedance spectrum of the
            zinc electrode

		frequency range	
□ uncharged (SOC 0%)		> 1	kHz
+ 0.015 Ah (SOC 3%)		> 4	Hz
o 0.075 Ah (SOC 14%)		> 0.01	Hz
• 0.50 Ah (SOC 100%)		> 0.01	Hz

multiplication factor : 2

The effect of discharge is shown in Fig. 7.23. The impedance values become
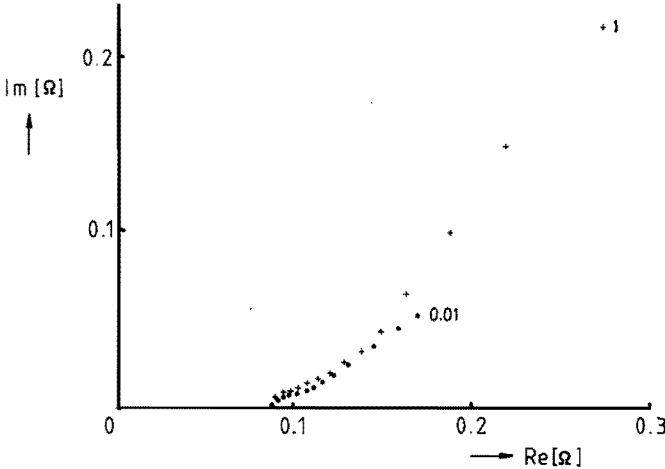larger and more capacitive, but the diagram does not revert to that for the
uncharged battery.

Fig. 7.23 Effect of the 1st discharge on the impedance spectrum of the
zinc electrode

		frequency range
•:0.50 Ah	(SOC : 100%)	> 0.01 Hz
+:discharged (SOC :	0%)	> 1 Hz
		multiplication factor : 2

Before discussing the influence of further charging and discharging on the
impedance of the zinc electrode, attention must be paid to two phenomena:
(i) the effect of the rest time and (ii) degassing of the cell.
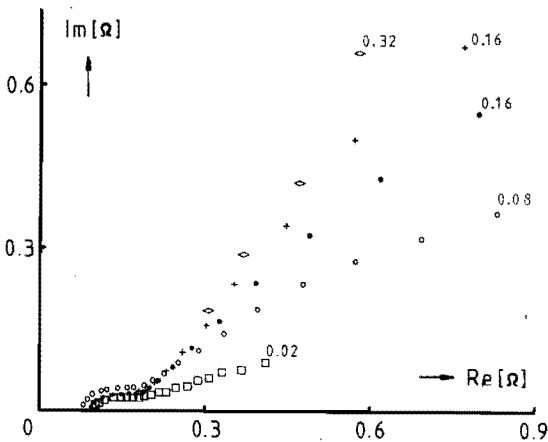
Fig. 7.24.

Impedance spectra of zinc elec-
trode with low state-of-charge
(10-15% SOC) as function of the
rest time.

□ : after   1.5 hour

o : after 69   hour

● : after 165 hour

+ : after 312 hour

◇ : after 672 hour

numbers indicate frequency
multiplication factor : 2

In Fig. 7.24 an impedance plot of a battery with a low state-of-charge
(about 10-15%) is shown at various rest times. The impedance increases with
the rest-time, which can be explained by the self-discharge of the active
zinc material, resulting in an increase of zinc oxide. The effect of de-
gassing is shown in Fig. 7.25. The shape of the impedance curve is unaf-
fected, but the absolute values of the real part of the impedance decrease,
indicating that the surface area electrode/electrolyte is increased by de-
gassing.

Therefore, all measurements are carried out after about half an hour rest-
time, without degassing of the cell.
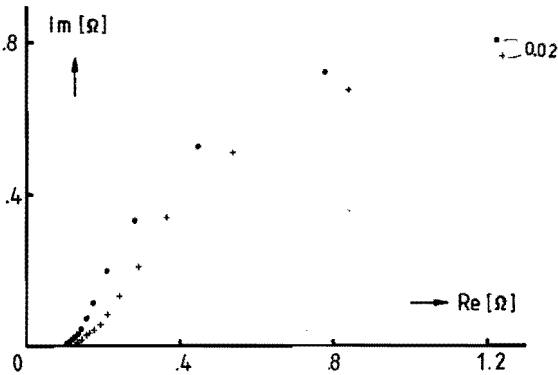
Fig. 7.25.

Effect of degassing on impe-
dance spectrum of zinc elec-
trode (0% SOC).

+ : before degassing

• : after degassing

The effect of cycling is shown in Fig. 7.26 for the zinc electrode in the
charged (100% SOC) and discharged (0% SOC) states. It is seen that the im-
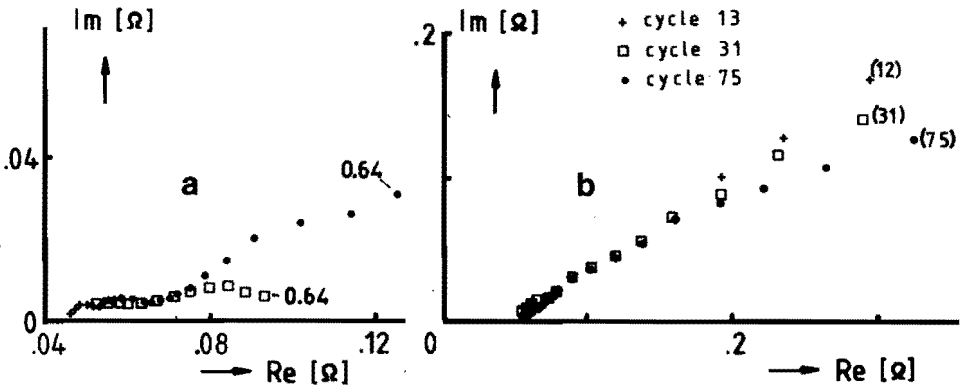

Fig. 7.26   Effect of cycling on impedance spectra

      a.   charged state

          Frequency range 0.64 → 10 kHz (multiplication factor : 2)

      b.   discharged state

          Frequency range 0.16 Hz → 10 kHz (multiplication factor : 2)

pedance in the charged state is always smaller than in the discharged state.
The curves, however, are not well-defined and specific information is
hardly obtainable. In order to see whether the drastic shape change of the
zinc electrode, as illustrated in Fig. 6.6 (Chapter 6), is also reflected
in the impedance data, real and imaginary parts of the impedance data at
different frequencies in charged and discharged state are plotted in Fig.
7.27 as function of cycle number. It appears that an effective change with
cycling cannot be detected because of the scatter in the data. Only an in-
crease in the real part of the impedance in the charged state of the bat-
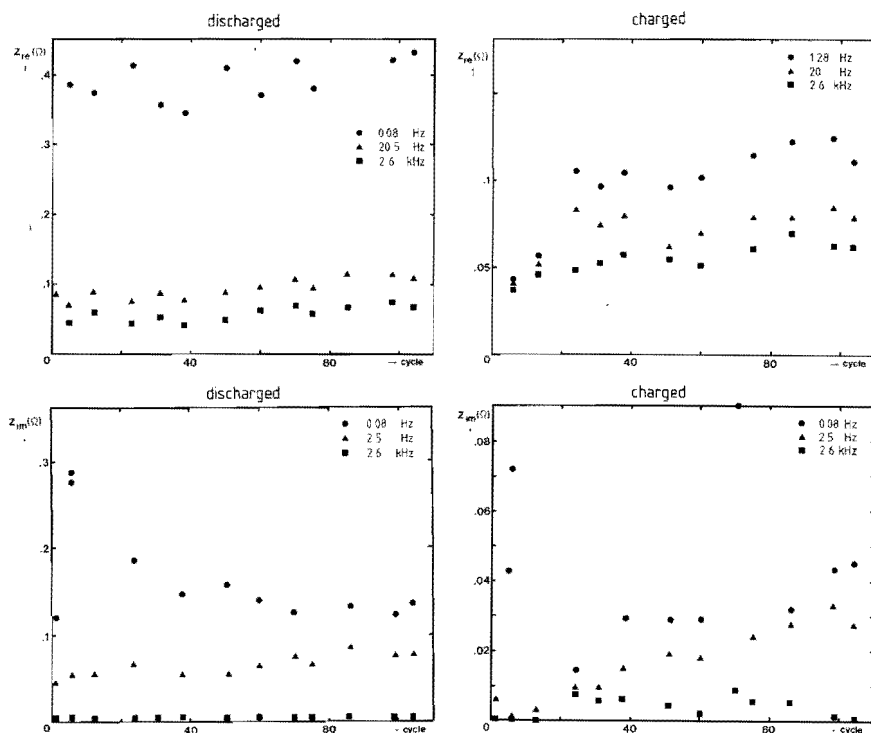tery is observed in the first twenty cycles.

Fig. 7.27   Real and imaginary parts of impedance data of the zinc electrode
            at different frequencies in charged and discharged state.

Addition of PbO of HgO to the zinc oxide electrode has no appreciable in-
fluence on the impedance diagram. The effect of these additives on the im-
pedance during cycle life is shown in Fig. 7.28 and 7.29. Compared with
the impedance of the zinc electrode, without additives (Fig. 7.27) no sig-
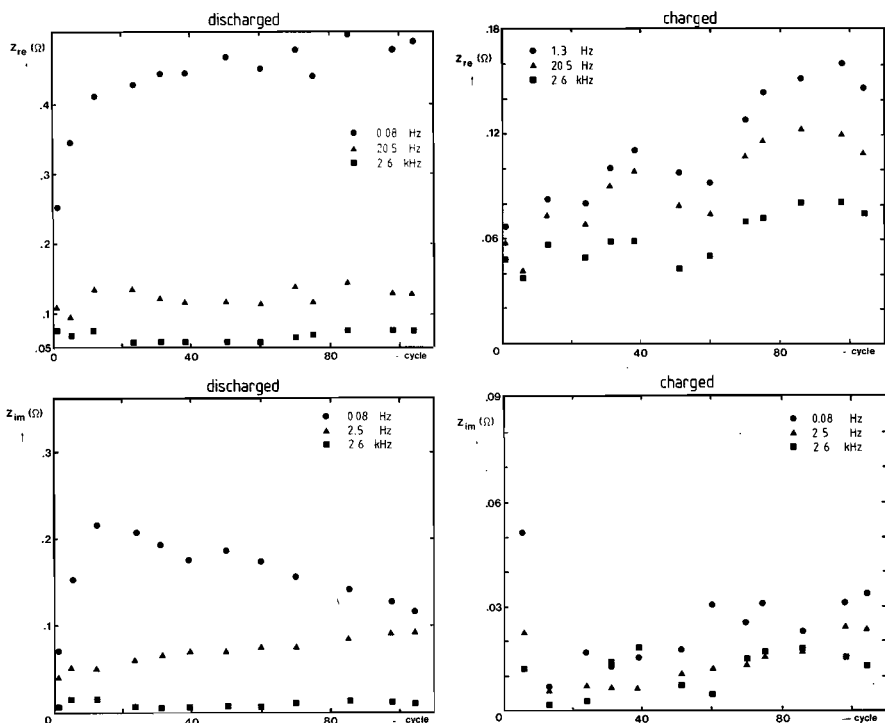nificant changes are observed. The values for the discharged state are

Fig. 7.28   Real and imaginary parts of impedance data of the zinc electrode
with PbO-additive af different frequencies in charged and dis-
charged state.

likewise independent of the cycle number. Only in the charged state an in-
crease of the real part of the impedance of the zinc electrode with PbO-ad-
ditive is observed, in contrast to the zinc electrode with HgO-additive,
where the impedance tends to decrease with cycling.
This could indicate a decrease (PbO-additive), resp. an increase (HgO-
additive) of the surface area of the zinc electrode in the charged state.
However, these trends cannot be correlated with the Shape Change of the zinc
electrodes: after 104 cycles the cells were taken apart and SC could be
visibly observed in all three cells (Fig. 6.6) without significant diffe-
rences between them. It would be expected that SC should result in a
decrease of surface area, so that in all three cells this decrease should
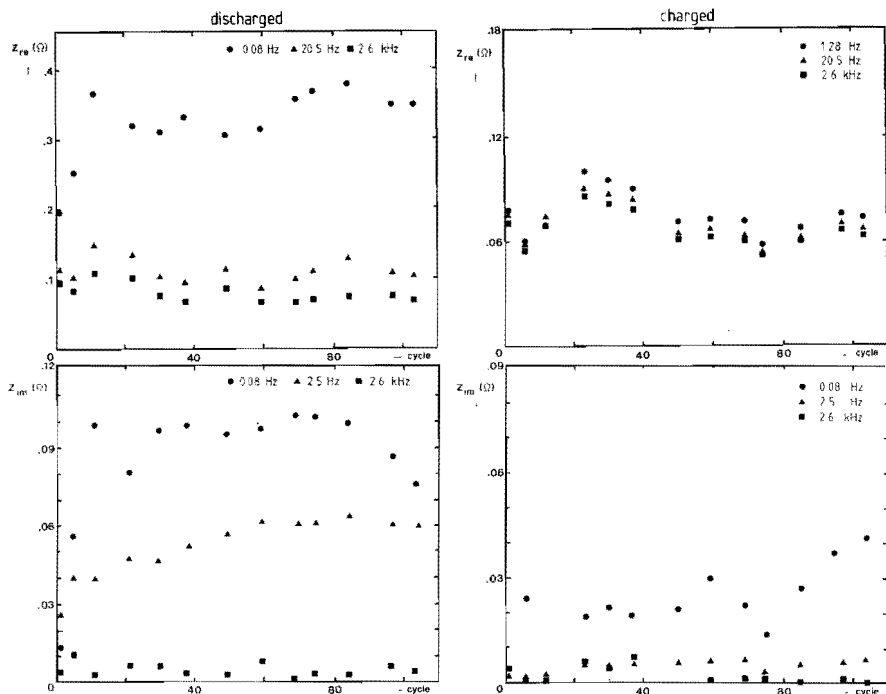be reflected in the impedance data.

Fig. 7.29   Real and imaginary parts of impedance data of the zinc electrode
            with HgO-additive at different frequencies in charged and dis-
            charged state.

7.6.   Conclusions.

- The impedance diagrams of amalgamated disc electrodes are not influenced
  by the method of amalgamation and can be adequately described with a
  kinetic and diffusion controlled reaction. The derived parameters are in
  good agreement with those calculated with the galvanostatic pulse tech-
  nique and indicate that no adsorption of hydroxyl ions or intermediate
  species at the amalgamated zinc electrode takes place.
- The impedance diagrams at the zinc disc electrode indicate that surface
  processes in which intermediate species are involved play a more important
  role.
- The impedance technique appears no to be a suitable technique for moni-
  toring the Shape Change of the zinc electrode. Only the imaginary part of
  the impedance at low frequencies (e.g. at 2.56 Hz, Fig. 7.27, 7.28, 7.29)
  might be used to discriminate between the charged and discharged state
  of the zinc electrodes.

7.7 LITERATURE

1. I. Epelboin, M. Ksouri and R. Wiart, J. Electrochem. Soc, $\underline{122}$ (1975) 1206.

2. I. Epelboin, M. Ksouri and R. Wiart, J. Electroanal. Chem. $\underline{65}$ (1975) 373.

3. J. Bressan and R. Wiart, J. Appl. Electrochem. $\underline{7}$ (1977) 505.

4. J. Bressan and R. Wiart, J. Appl. Electrochem. $\underline{9}$ (1979) 43.

5. J. Bressan and R. Wiart, J. Appl. Electrochem. $\underline{7}$ (1982) 615.

6. C. Cachet, U. Ströder and R. Wiart, Electrochem. Acta $\underline{7}$ (1982) 903.

7. C. Cachet, U. Ströder and R. Wiart, J. Appl. Electrochem. $\underline{11}$ (1981) 613.

8. S. Karunathilaka, N.A. Hampson, R. Leek and T.J. Sinclair, J. Appl. Electrochem. $\underline{10}$ (1980) 357, 603, 799.

9a. S. Karunathilaka, N.A. Hampson, R. Leek and T.J. Sinclair, J. Appl. Electrochem. $\underline{11}$ (1981) 365, 715.

9b. M. Hughes, S. Karunathilaka, N.A. Hampson and T.J. Sinclair, J. Appl. Electrochem. $\underline{13}$ (1983) 217.

10. S. Karunathilaka, N.A. Hampson, T.P. Haas, R. Leek and T.J. Sinclair, J. Appl. Electrochem. $\underline{11}$ (1981) 573.

11. J. Randles, Discuss. Faraday Soc. $\underline{1}$ (1947) 11.

12. M. Sluyters-Rehbach and J.H. Sluyters, in A.J. Bard (ed.), Electro-analytical Chemistry Vol. 4, Dekker, New York, 1970, p. 1.

13. H. Gerischer, Z. Elektrochem. $\underline{62}$ (1958) 256.

14. M. Fleischmann, S.K. Ranjarajan and H.R. Thirks, Trans. Faraday Soc. $\underline{63}$ (1967) 1240, 1251, 1256.

15. H. Gerischer, W. Mehl, Z. Elektrochem. $\underline{59}$ (1955) 1049.

16. I. Epelboin, R. Wiart, J. Electrochem. Soc. $\underline{118}$ (1971) 1577.

17. Handbook of Chemistry and Physics, 62n edition, 1981-1982, CRC Press Inc. Boca Raton, Florida USA.

18. J. McBreen, "Study to investigate and improve the zinc electrode for space craft electrochemical cells", NASA contract No. NAS 5-10231, June 1967, N67-37197.

19. R. de Levie, in P. Delahay (ed.), Advances in Electrochemistry and Electrochemical Engineering, Vol. 6, John Wiley & Sons, New York, 1967, p. 329.

ACKNOWLEDGEMENTS

LIST OF SYMBOLS

a   activity [mol l^{-1}]; lattice parameter

A   surface area [cm^2]; correlation constant in eq. (2.2);
rate of nucleation [$cm^{-2} s^{-1}$]

A'   rate of conversion of a site into a nucleus [s^{-1}]

b   tafel slope [mV]

B   constant in Davies equation (5.1); correlation constant in eq. (2.2)

c   concentration [mol l^{-1}]; lattice parameter

C   capacitance [F]

D   diffusion coefficient [$cm^2 s^{-1}$]; depth of discharge in eq. (2.3)

E   potential [V]

F   Faraday constant [C eq.$^{-1}$]

i   current density [A cm^{-2}]

i_o exchange current density [A cm^{-2}]

I   current [A]; ionstrength [mol l^{-1}]

I_o exchange current [A]

j $\sqrt{-1}$

k   rate of crystal growth [mol $cm^{-2} s^{-1}$]; rate constant [cm s^{-1}]

K   penetration constant [$cm^2 s^{-1}$]

l   distance [cm]

L   number of cycles in eq. (2.3)

M   molecular weight [g mol^{-1}]

n   number of electrons

N   number of nuclei [cm^{-2}]; Avogadro's number [mol^{-1}]

p   reaction order

q   charge amount per volume unit [mC cm^{-2}]

Q   charge amount [mC]

r_c critical size of a nucleus [cm]

R   resistance [Ω]; gas constant [kJ $mol^{-1} K^{-1}$]; mean pore radius [$\overset{\circ}{A}$]

t   time [s]

T   temperature [K]

V   volume per gram [$cm^3 g^{-1}$]

Y   admittance [Ω^{-1}]

z   number of electrons

Z   impedance [Ω]

α transfer coefficient; proportionality factor in eq. (2.3);
packing factor in eq. (3.3); correlation coefficient in eq. (4.3)

$\gamma_{\pm}$ activity coefficient

δ thickness of Nernst diffusion layer [cm]

Δ ellipsometric parameter

ε porosity

η overpotential [V]

θ contact angle ; surface coverage

ν kinematic viscosity [$cm^2\ s^{-1}$]

ρ density [$g\ cm^{-3}$]; faradaic resistance [Ω]

σ Warburg coefficient [$\Omega\ s^{\frac{1}{2}}$]

σ_n standard deviation

ψ ellipsometric parameter

ω (rotation) frequency [s^{-1}]

Subscribts

a   anodic

ad   adsorption

c   cathodic

ct   charge transfer

dl   double layer

f   faradaic

ox   oxidized

p   passivation, primary, pore

r   rest

rev   reversible

s   surface, secondary

t   total

W   Warburg

Abbreviations

CE   counter electrode

NHE   normal hydrogen electrode

RE   reference electrode

RDS   rate determining step

SC   Shape Change

SCE   standard calomel electrode

SOC   state-of-charge

WE   working electrode

Superscripts

σ at electrode surface

S   in bulk

'   real part

"   imaginary part

SUMMARY

The alkaline nickel oxide-zinc battery is a promising candidate as energy
source for traction purposes. A number of problems hinder a break-through
of this battery. The main problem is the limited cycle life caused by
various processes at the zinc electrode, among which Shape Change is the
principle one.
This thesis reports on certain aspects of the zinc electrode reaction and
behaviour, both in a conventional electro-chemical cell and in an actual
battery system.

In Chapter 2 a literature survey is given on the properties of zinc in al-
kaline solutions and the proposed mechanisms of Shape Change. In general,
Shape Change is attributed to non-uniform current distributions or to
electro-osmotic effects. It is concluded that neither of these mechanisms
can explain all observed data.

The initial stages of the electrocrystallization of zinc onto a silver sub-
strate are investigated (chapter 3), using the potential step method. This
is done because at the zinc electrode deposition and dissolution processes
take place, in which the formation and breakdown of crystal lattices are
involved. Analysis of the experimental current-time transients with detailed
models of nucleation and growth was possible and it was concluded that the
electrocrystallization of zinc proceeds via nucleation and growth, first of
a thin layer of primary centers, having low angle of contact at low over-
potentials, and subsequently by a layer, which starts to grow via secondary
centers, formed at the sites where the primary centers coalesce.

The interaction of the electro deposited zinc and the polycrystalline sil-
ver was studied with cyclic voltammetry, microbrobe technique and ellipso-
metry (Chapter 4). Zinc forms alloys with the substrate via diffusion. Two
phases are identified: the ϵ-phase ($AgZn_3$) and the ξ-phase (AgZn).
With time continuous transformation into phases with lower zinc content
takes place, ultimately resulting in the formation of the α-phase.

In an actual battery the zinc electrode is usually amalgamated to hinder
the formation of hydrogen. Because little information is available to date
in the literature on the reaction mechanism of the amalgamated zinc, the
reaction mechanism of zinc and amalgamated zinc electrodes was investi-
gated with the galvanostatic transient technique (Chapter 5). The results
for the zinc electrode indicate a reaction mechanism in which the rate

determining step is given by

$$Zn(OH)_2^- + OH^- \rightarrow Zn(OH)_3^- + e^-$$
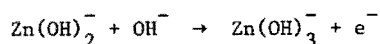
The results for the amalgamated zinc electrodes are not influenced by the method of amalgamation and suggest a mechanism which involves the participation of water. The differences between the zinc electrode and the amalgamated zinc electrodes are explained by changes in the adsorption behaviour.

The method of amalgamation has also no effect on the results of the impedance measurements (Chapter 7).
The impedance diagrams of amalgamated electrodes can be adequately described with a kinetic and a diffusion controlled reaction. The derived parameters are in good agreement with those calculated with the galvanostatic pulse technique and indicate that no adsorption of hydroxyl ions or intermediate species at the amalgamated zinc electrode takes place.
The impedance diagrams at the zinc electrode indicate that surface processes in which intermediate species are involved play an important role.

Finally, in order to obtain more information on the cycling behaviour and especially on the shape change phenomenon, different types of teflon bonded zinc and amalgamated zinc electrodes in the nickel oxide–zinc battery are investigated by repeated charge/discharge cycles, measurement of the potential distribution along the zinc surface (Chapter 6) and impedance measurements (Chapter 7). It appeared that impedance measurements could be used to discriminate between the charged and discharged state; however, it was not possible to monitor processes as Shape Change and densification.
It is found that the increase of the cathodic overpotentials of the zinc electrode is related with the local availability of the reducible zinc oxide amount and that the change in capacity with cycling is strongly determined by the porosity of the zinc electrode and the excess amount of zinc oxide.
A tentative explanation for the mechanism of Shape Change is given, based on different current distributions during the charge and discharge period, leading to a net movement of zincate in the direction of the centre via diffusion and so to the material redistribution (Shape Change).

SAMENVATTING

De alkalische nikkel oxide-zink batterij is een veelbelovende energiebron
voor traktiedoeleinden. De doorbraak van deze batterij heeft echter nog niet
plaatsgevonden, voornamelijk vanwege een te geringe cycleerbaarheid, hetgeen
in belangrijke mate wordt veroorzaakt door de vormverandering ("Shape
Change") van de zink elektrode. In dit proefschrift worden een aantal aspec-
ten van de reakties van de zink elektrode, zowel in een konventionele elek-
trochemische cel als in een batterij systeem beschreven.

In hoofdstuk 2 worden de eigenschappen van zink in alkalische oplossingen
uitvoerig besproken en wordt ingegaan op de in de literatuur voorgestelde
mechanismen van de vormverandering. Deze vormverandering wordt toegeschreven
aan ongelijkmatige stroomverdelingen of elektro-osmotische effekten. Geen van
deze twee mechanismen kan alle waargenomen verschijnselen verklaren.

De beginstadia van de elektrokristallisatie van zink op een zilver sub-
straat zijn in hoofdstuk 3 onderzocht met behulp van de potentiaal sprong
methode, omdat de vorming en afbraak van het kristalrooster van zink een
belangrijke rol spelen bij de processen, die gedurende het laden en ontladen
aan de zink elektrode plaatsvinden. De experimenteel gemeten stroom-tijd
kurven konden geanalyseerd worden met gedetailleerde modellen van kiemvorming
en groei. Deze elektrokristallisatie voltrekt zich via kiemvorming en groei
van twee lagen, een eerste laag van primaire centra, gevolgd door een laag
van secundaire centra, die gevormd worden op plaatsen waar de primaire elkaar
overlappen.

Vervolgens is de rol van het substraat verder onderzocht door bestudering
van de interaktie met het neergeslagen zink met behulp van cyclische voltam-
metrie, de microprobe techniek en ellipsometrie (Hoofdstuk 4). Het blijkt dat
het zink via diffusie legeringen met het zilver vormt. De ε-fase (AgZn$_3$)
en de ξ-fase (AgZn) zijn geïdentificeerd. Met de tijd vinden voortdurend
transformaties plaats naar fasen met een lager zinkgehalte, hetgeen uit-
eindelijk resulteert in de vorming van de α-fase.

Om de vorming van waterstof tegen te gaan wordt in een batterij de zink elek-
trode meestal geamalgameerd. Omdat er in de literatuur weinig bekend is over
het reaktiemechanisme aan de geamalgameerde elektrode is een studie gemaakt
van het reaktiemechanisme van zink en diverse typen geamalgameerde zink elek-
troden (Hoofdstuk 5). Dit gebeurde met behulp van de galvanostatische transiënt
techniek. De resultaten voor de zink elektroden duiden op een reaktiemechanisme

met de volgende snelheidsbepalende stap:

$$Zn(OH)_2^- + OH^- \rightarrow Zn(OH)_3^- + e^-$$
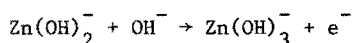
De resultaten voor de geamalgameerde zink elektroden worden niet beïnvloed door de methode van amalgamering en wijzen op een mechanisme met water als reaktie partner. De verschillen tussen de zink elektrode en de geamalgameerde zink elektroden worden verklaard door verandering in adsorptiegedrag.

De impedantie diagrammen van de geamalgameerde elektroden (Hoofdstuk 7) worden niet beïnvloed door de wijze van amalgameren en kunnen beschreven worden met een model voor een kinetisch en diffusie bepaalde reaktie. De afgeleide parameters stemmen goed overeen met die welke met behulp van de galvanostatische transiënt techniek zijn verkregen en duiden erop dat geen specifieke adsorptie van hydroxylionen en intermediairen aan de geamalgameerde elektroden optreedt. Impedantie diagrammen van de zink elektrode geven aan dat oppervlakte processen, waarin intermediairen zijn betrokken, belangrijk zijn.

Om meer inzicht te verkrijgen in het cycleergedrag en speciaal in de vormverandering zijn tenslotte verschillende typen zink elektroden (zink oxide gebonden met teflon, en geamalgameerd zink poeder met teflon gebonden zink oxide) in de nikkeloxide-zink batterij onderzocht. Dit is gedaan met behulp van herhaalde laad/ontlaad cycli, meting van de potentiaalverdeling langs het zink oppervlak (Hoofdstuk 6) en impedantiemetingen (Hoofdstuk 7). De impedantiemetingen blijken weliswaar informatie over de laadtoestand te geven maar kunnen niet gebruikt worden om de processen van vormverandering en verdichting van het aktieve materiaal te volgen. De toename van de overpotentialen tijdens het opladen van de zink elektrode hangt samen met de beschikbaarheid van de hoeveelheid reduceerbaar zink oxide ter plekke. De verandering in kapaciteit met cycleren wordt sterk beïnvloed door de porositeit van de zink elektrode en de overmaat aan zink oxide.
Voor het mechanisme van de vormverandering wordt een mogelijke verklaring gegeven, die gebaseerd is op verschillen in stroomverdeling gedurende de laad- en ontlaadperiode. Via diffusie van zinkaat leidt dit tot een netto verplaatsing in de richting van het centrum en zo tot een herverdeling van het aktieve materiaal.

CURRICULUM VITAE

De schrijver van dit proefschrift is geboren op 22 mei 1953 te Weert.
Na het behalen van het diploma Gymnasium B aan het Bisschoppelijk College
te Weert begon hij in september 1971 met de studie Scheikundige Technologie
aan de Technische Hogeschool te Eindhoven. Het afstudeeronderzoek werd
verricht bij de vakgroep Instrumentele Analyse onder leiding van Prof.
Dr.Ir. C.A.C.G. Cramers. Op 22 februari 1978 behaalde hij het ingenieurs-
diploma.
Tijdens zijn militaire dienstperiode was hij gedetacheerd bij het Prins
Maurits Laboratorium TNO te Rijswijk. In maart 1980 begon hij bij de vak-
groep Elektrochemie van de Technische Hogeschool te Eindhoven, onder
begeleiding van Prof. E. Barendrecht aan het onderzoek, waarvan dit
proefschrift het resultaat is.

DANKWOORD

STELLINGEN.

1. Het is onwaarschijnlijk dat het cyclovoltammetrische gedrag van een poreuze zinkoxyde-elektrode in het potentiaalgebied van -0,9 tot -1,34 V (vs. Hg/HgO) verklaard kan worden door direkte reduktie van zinkoxyde vanuit de vaste fase.

   J. McBreen and E. Gannon, Electrochim. Acta <u>26</u> (1981) 1439.

2. Het elektrochemische gedrag van een geamalgameerde zinkelektrode, verkregen via galvanostatische elektrodepositie [1] is niet representatief voor een zinkelektrode geamalgameerd door middel van de - in de batterijtechnologie gebruikelijke - stroomloze depositie [2].

   1. L.M. Baugh, F.L. Tye and N.C. White in "Power Sources 9", J. Thompson ed., Academic Press, London, 1983, p.303.
   2. J. Swift, F.L. Tye, A.M. Warwick and J.T. Williams in "Power Sources 4", D.H. Collins ed., Oriel Press, Newcastle upon Tyne, 1973, p.415.

3. Bij de bepaling van reaktieorden dienen aktiviteiten in plaats van koncentraties gebruikt te worden.

   J.O'M. Bockris and A.K.N. Reddy, Modern Electrochemistry, Plenum Press, New York, 1970.

4. Het door Wroblowa et al. ontwikkelde kriterium, om uit te maken of de zuurstofreduktie al dan niet via waterstofperoxyde verloopt, is praktisch van weinig waarde omdat dit kriterium te hoge eisen aan de experimentele nauwkeurigheid stelt.

   H.S. Wroblowa, Yen-Chi-Pan and G. Razumney, J. Electroanal. Chem. <u>69</u> (1976) 195.

5. Impedantiemetingen roepen voornamelijk weerstand op.

6. Voor de promovendus gaat de spreuk "wie schrijft die blijft" meestal niet op.

7. De huidige trend om barokmuziek uit te voeren op alleen authentieke
   instrumenten strookt niet met de intentie van de barokkomponisten,
   die openstonden voor nieuwe ontwikkelingen op gebied van instrumenten.

8. De thermochemische produktie van waterstof is een onhaalbare kaart.

   Th. van der Plas, Energiespectrum, februari 1984, p.42.

9. Dat relatief meer vrouwen dan vroeger een stottertherapie volgen
   duidt erop dat het emancipatieproces zijn vruchten afwerpt.

   J. Fluency Disorders 2 (1977) 301.

Eindhoven, 29 mei 1984   Jos Hendrikx